Geometry and construction history of the Copper Ridge laccolith, Mount Ellen, Henry Mountains, Utah

By

Elizabeth Anna Maurer

July, 2015

Director of Thesis: Eric Horsman

Major Department: Geological Sciences

The Copper Ridge laccolith is an asymmetric tongue-shaped intrusion located on the southeastern margin of Mount Ellen in the Henry Mountains, Utah. The late-Oligocene to early-Miocene igneous rocks have no syn- or post-emplacement tectonic overprint. In addition, exposure of the laccolith is exceptional: well-preserved sedimentary strata cap the intrusion, the lower contact is locally exposed, and numerous natural cross sections can be studied. These characteristics make the Copper Ridge laccolith an ideal location to study emplacement of magma in the shallow crust. Field mapping shows the intrusion is about 3.5 km wide, 2.0 km long and, at its thickest point, 425 m thick. The estimated magma volume is about 2.9 km^3. Field work, crystal size distribution, and geochemistry, suggest that the intrusion was built incrementally through the injection of two separate magma batches, resulting in an upper and a lower sheet. Field work shows that the upper sheet is separated from the lower sheet by well-preserved, variably metamorphosed Cretaceous Tununk shale. Data from anisotropy of magnetic susceptibility analysis suggest a subhorizontal sill fed the intrusion from the west-northwest, and magma flowed to the southeast in a fanning pattern. X-ray diffraction data show that the preserved Tununk experienced low-grade contact metamorphism. Multiple data sets suggest a construction model in which the upper sheet intruded first, lifting and deforming the sedimentary strata. The lower sheet intruded second and off center relative to the upper sheet. The asymmetric lifting caused the upper sheet to fracture adjacent to the southern margin of the lower

sheet. The fractures likely facilitated weathering and erosion, causing the upper sheet to appear segmented in current exposure.

GEOMETRY AND CONSTRUCTION HISTORY OF THE COPPER RIDGE LACCOLITH, MOUNT ELLEN, HENRY MOUNTAINS, UTAH

A Thesis

Presented To the Faculty of the Department of Geological Sciences

East Carolina University

In Partial Fulfillment of the Requirements for the Degree

Master of Science in Geology

by

Elizabeth Anna Maurer

July, 2015

GEOMETRY AND CONSTRUCTION HISTORY OF THE COPPER RIDGE LACCOLITH, MOUNT ELLEN, HENRY MOUNTAINS, UTAH

by

Elizabeth Anna Maurer

APPROVED BY:

DIRECTOR OF THESIS:_____
Eric Horsman, PhD

COMMITTEE MEMBER: _____
Terri Woods, PhD

COMMITTEE MEMBER: _____
Adriana Heimann, PhD

COMMITTEE MEMBER: _____
Sven Morgan, PhD

CHAIR OF THE DEPARTMENT
OF GEOLOGICAL SCIENCES: _____
Stephen J. Culver, PhD

DEAN OF THE
GRADUATE SCHOOL: _____
Paul J. Gemperline, PhD

DEDICATION

I would like to dedicate this thesis to my father. Without you, none of this would have been possible. Thank you for your endless love and support throughout every aspect of my life.

Acknowledgements

First and foremost, I would like to thank my thesis advisor Dr. Eric Horsman, without whom this project would not have been possible. His guidance during field work, data analysis, and writing has been instrumental in the completion of my thesis. I would also like to thank my committee members, Dr. Richard Mauger, Dr. Adriana Heimann, and Dr. Sven Morgan for their help and insight in various aspects of my research, and for their review of my thesis.

A special thanks to Erik Thornton for his help with field work, and life in general. Your support means the world to me.

I would like to thank the faculty of the Department of Geological Sciences at East Carolina University for their support and seemingly endless wealth of knowledge.

Finally, I would like to thank the National Science Foundation and the Geological Society of America for funding of this project.

Table of Contents

List of Tables

List of Figures

List of Plates

List of Abbreviations

CRL	Copper Ridge laccolith	8
CSD	Crystal size distribution	23
ICP-MS	Inductively coupled plasma mass spectrometry	25
AMS	Anisotropy of magnetic susceptibility	25
XRD	X-ray diffraction	28
Q	Quaternary	31
T	Tertiary	31
K	Cretaceous	31
J	Jurassic	31
REE	Rare earth element	56

Introduction

Extensive studies of igneous intrusions have greatly altered the way we think about the movement of magma and emplacement of igneous intrusions in the shallow crust. For some time the big tank hypothesis was the favored method of formation for igneous intrusions. However, studies on well-exposed intrusions like those in the Henry Mountains have revealed that some shallow intrusions form through pulses of magma. Various characteristics can provide evidence for pulsed construction, including geochemical variations in igneous rocks and the nature of preserved contacts. The study of fabrics preserved in the igneous rocks can aid in our understanding of how magma moves through the shallow crust, and can have implications on the mitigation of volcanic hazards. In many locations, finding evidence for pulsed construction can be difficult due to lack of exposure, and interpreting magmatic fabrics can be complicated if there is a tectonic overprint. The intrusions in the Henry Mountains are exceptionally exposed, and have no tectonic overprint, making them an excellent place to study pulsed construction.

The Henry Mountains consist of five mid-Tertiary igneous intrusive centers (Nelson et al., 1992), the largest of which is Mount Ellen. This study focuses on the Copper Ridge laccolith, a largely concordant igneous body on the southeastern flank of Mount Ellen (Figure 1A). The Copper Ridge laccolith provides an exceptional opportunity to study shallow igneous intrusions for several reasons. First, exposures are exceptional: well-preserved sedimentary rocks cap the intrusion, the lower contact is exposed in several locations, and numerous cross sections through the interior can be studied (Figure 1B; Hunt et al., 1953). Along these cross sectional transects, sedimentary strata are locally preserved, separating two thick sections of igneous rocks. Such exposures are rare elsewhere. Second, the intrusive body formed during a time of no regional deformation and there has been no post-emplacement tectonic activity, resulting in no tectonic

overprint in the rocks (Horsman et al., 2010). Therefore, the magmatic fabrics preserved during the rapid cooling of the intrusive rocks can be interpreted as the product of purely magmatic processes.

The goal of this study is to constrain the geometry and reconstruct the emplacement history of the Copper Ridge laccolith. Several field and laboratory techniques were employed to understand how the intrusion formed and to identify the processes that operated within the system. To construct the geometry and understand the timing of the magma pulses, field observations, crystal size distribution, and major and trace element geochemistry were used. In order to understand magma flow and deformation of sedimentary strata, field observations, anisotropy of magnetic susceptibility, and x-ray diffraction were used. The aforementioned techniques were used to test two hypotheses: 1) the Copper Ridge laccolith was constructed through the injection of two or more separate magma pulses at different times, and 2) the laccolith was fed by a conduit and magma then migrated laterally between sedimentary strata, deforming the strata in the process.

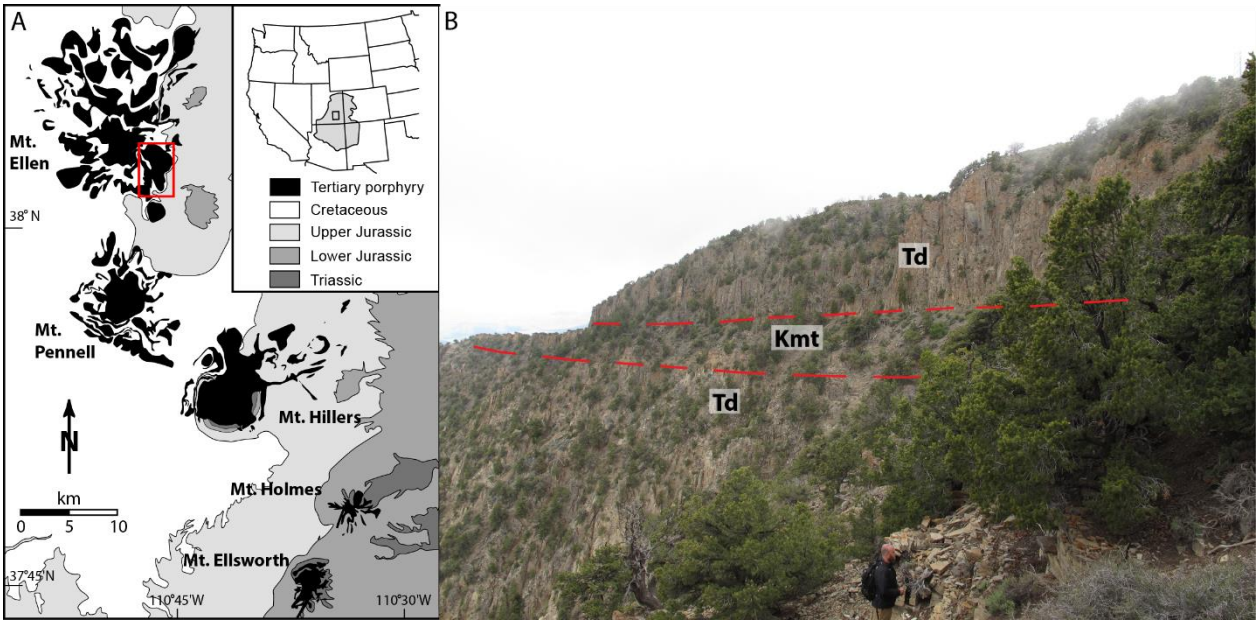

Figure 1. A: Map showing the location of the Henry Mountains in Utah. The Copper Ridge laccolith on Mount Ellen is outlined in the red box (modified from Horsman et al., 2010). B. Photograph showing a natural cross section through the Copper Ridge laccolith, with the contacts between the Cretaceous Tununk shale (Kmt) and the igneous rocks (Td) marked by dashed red lines.

Background

Geologic Setting

Colorado Plateau

The Colorado Plateau geologic province (Figure 2) extends over about 350,000 km^2 in the North American Cordillera (Hunt, 1956). It is underlain by 45-50 km of crust, and bounded by regions marked by deformation and magmatism (Thompson and Zoback, 1979; Beghoul and Barazangi, 1989). It consists of mostly subhorizontal Paleozoic through Tertiary sedimentary strata (Figure 3) deposited on Precambrian basement rocks (Hunt, 1956).

The regions surrounding the Colorado Plateau underwent intense deformation and magmatism from late Cretaceous to Eocene time including crustal shortening, followed by Oligocene volcanism and late Cenozoic magmatism, uplift and extension (Nelson et al, 1992; Nelson and Davidson, 1993). In contrast, interior parts of the Colorado Plateau itself have been less susceptible to the deformation (Beghoul and Barazangi, 1989). The minimal deformation experienced by the Colorado Plateau interior is likely the result of the structural and rheological properties of the thickened crust (Thompson and Zoback, 1979; and Nelson and Davidson, 1993).

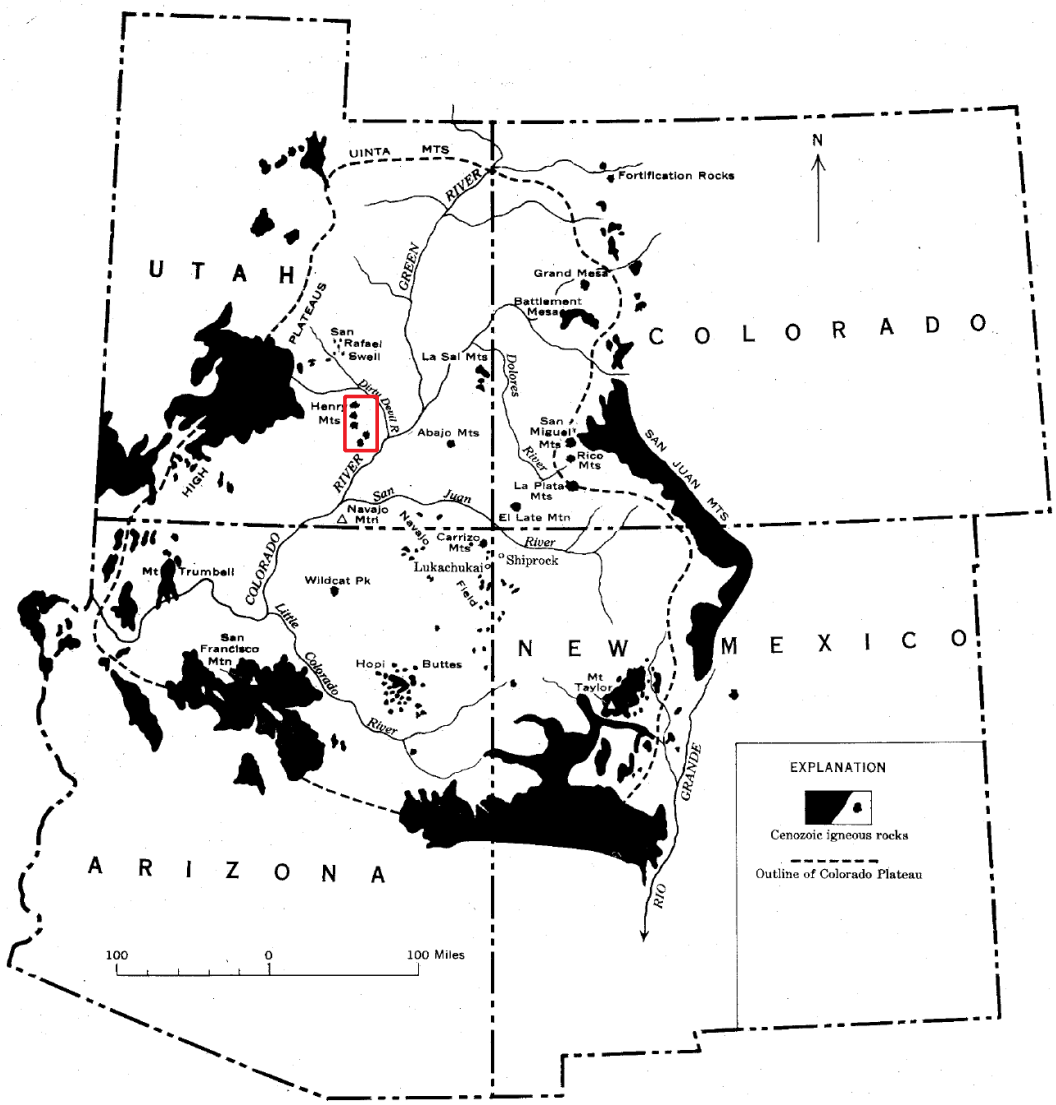

Figure 2. Map showing the location of the Colorado Plateau and the distribution of Cenozoic igneous rocks (from Hunt, 1956). The Henry Mountains are outlined by the red box.

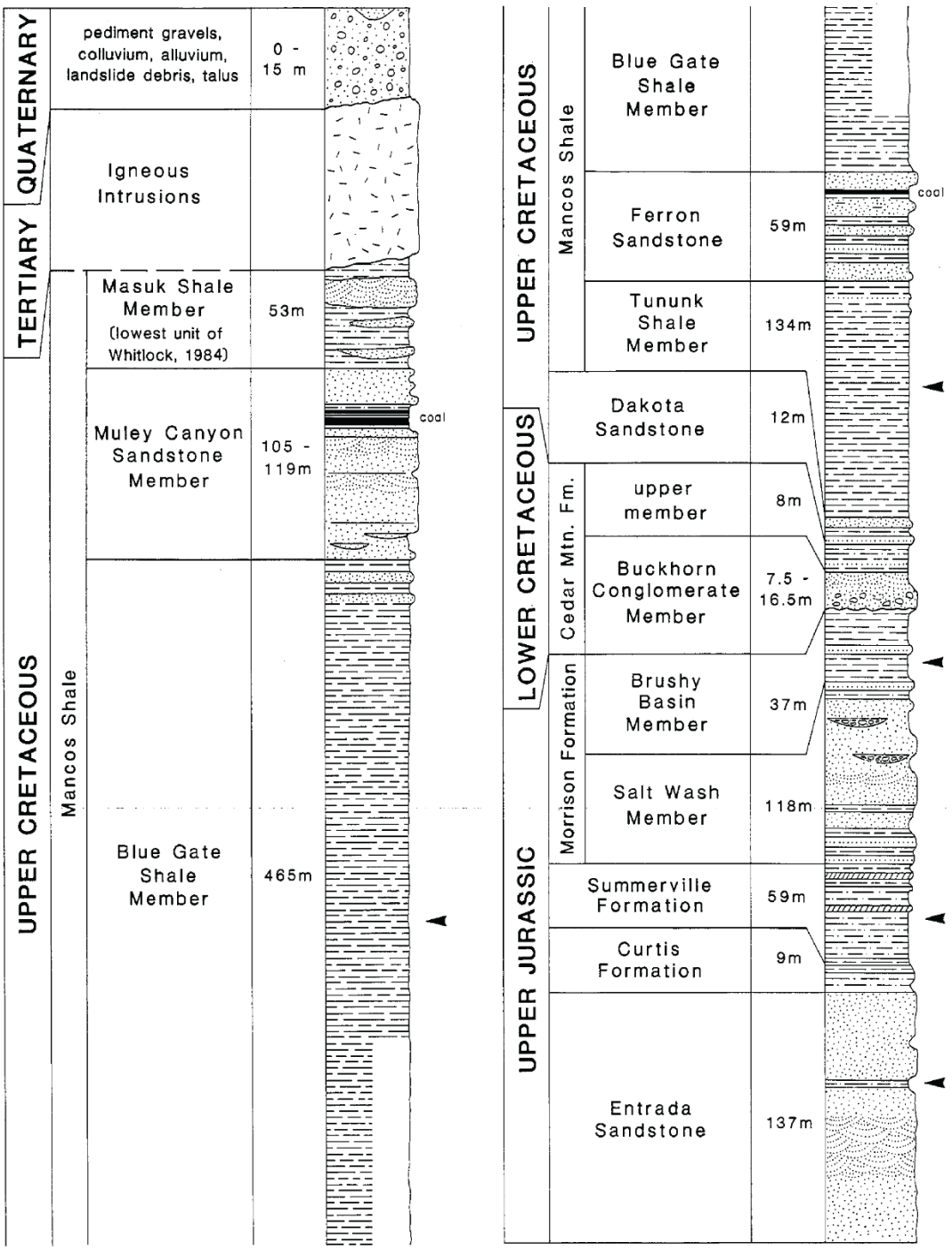

Figure 3. Stratigraphic section of the Colorado Plateau rocks observed on Mount Ellen in the Henry Mountains (from Morton, 1984). Black arrows indicate units that magma preferentially intruded.

The Henry Mountains

The Henry Mountains consist of five igneous intrusive centers: Mount Ellen, Mount Pennell, Mount Hillers, Mount Holmes, and Mount Ellsworth (listed from north to south) (Figure 1A). These five peaks trend north-south and extend for approximately 50-60 km (Hunt et al., 1953; Johnson and Pollard, 1973; Jackson and Pollard, 1988; Saint-Blanquat et al., 2006). The intrusive centers formed on the shallowly west dipping eastern limb of a structural basin, the western limb of which is part of the Waterpocket Fold monocline (Gilbert, 1877; Hunt et al., 1953). Magma intruded subhorizontal sedimentary strata, uplifting and deforming the host rocks in the process. Each of the resulting intrusive centers is composed of a large central intrusive body with smaller intrusions radiating towards the margins (Gilbert, 1877; Hunt et al., 1953; Jackson and Pollard, 1988). Each large central body is comprised of numerous component intrusions (Broda, 2014; Ward, 2014).

Nelson et al. (1992) dated titanite and zircon crystals using $^{40}Ar/^{39}Ar$ dating, and hornblende and feldspar crystals using fission track dating. The range of Henry Mountains igneous rock ages is 32-23 Ma (Nelson et al., 1992). Geochemical signatures of Henry Mountains rocks suggest they are typical of subduction-related volcanic arcs (Nelson et al., 1992; Nelson and Davidson, 1993, 1998). As subduction occurred, basaltic melts pooled under the Colorado Plateau, and melted deep portions of the crust. Assimilation and fractional crystallization occurred in the deep crust until portions of the magma ascended rapidly to the shallow crust (Nelson and Davidson, 1998). The magma cooled quickly and texturally the rocks are plagioclase-hornblende porphyry. Compositionally the rocks are andesite-to-trachyandesite.

Mount Ellen

Mount Ellen is the largest of the five Henry Mountains, with a diameter of about 24 km and total magma volume of about 3 km^3 (Hunt et al., 1953). The Mount Ellen intrusive center is made up of many laccolithic bodies that are stacked in some places, and radiate outward from the center of the mountain (Figure 4). Many of the laccoliths are circular in map-view, but some exhibit an asymmetric geometry. Several laccoliths and three large bysmaliths are exposed throughout the region. Sedimentary strata around the flanks of Mount Ellen are minimally deformed, and most retain their original subhorizontal orientation. Locally, there are varying degrees of deformation in the sedimentary strata adjacent to intrusive bodies.

The Copper Ridge laccolith (CRL) is located on the eastern margin of Mount Ellen and is the focus of this study (Figure 1A). CRL is asymmetric and tongue-shaped in map-view. In cross sectional view CRL is plano-convex with a flat roof and floor. In several locations, natural cross sections through the intrusion exist, most notably on a prominent east-facing cliff (Figure 1B, Figure 5). Along these cross sections, a thick layer of Cretaceous Tununk shale is preserved between two thick sections of igneous rocks. The upper section of igneous rock is about 80-100 m thick, and the lower portion is about 300-340 m thick. Sedimentary strata around CRL are generally subhorizontal, with only local variations in the dip around the margins of the intrusion.

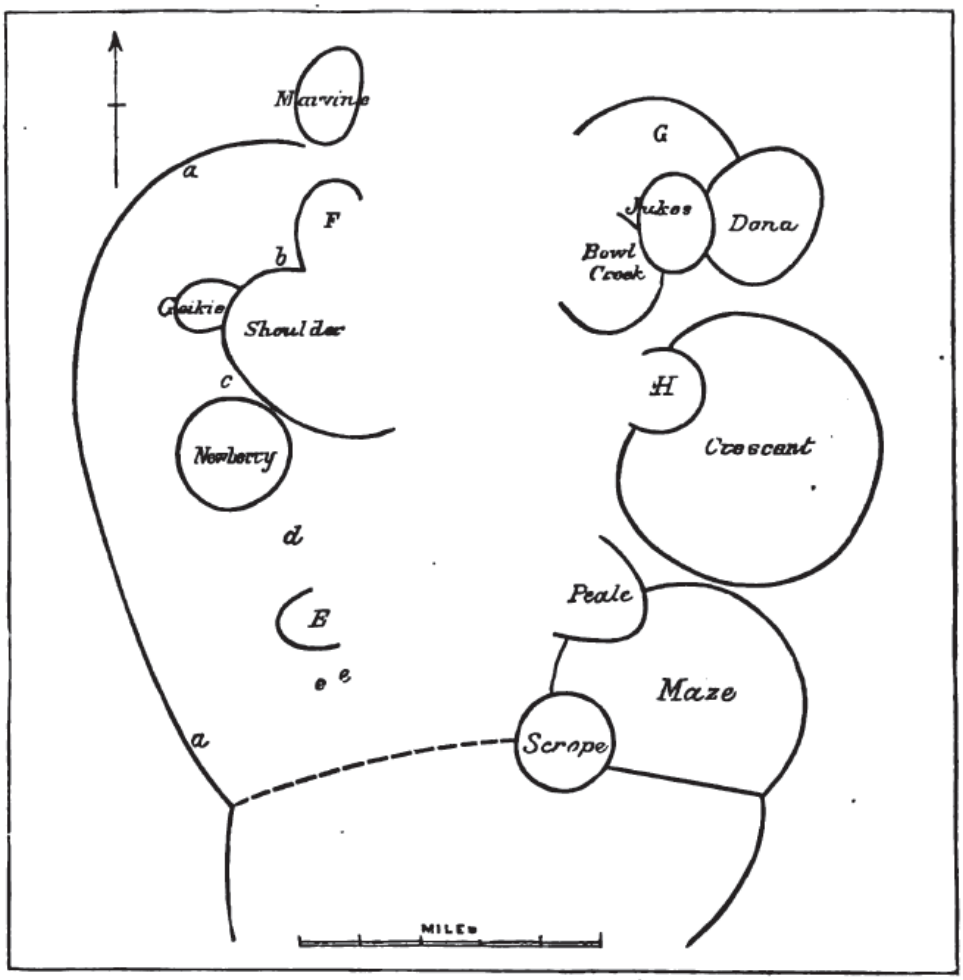

Figure 4. Map-view sketch of the cluster of laccoliths that make up Mount Ellen (from Gilbert, 1877). The Peale laccolith is now referred to as the Copper Ridge laccolith.

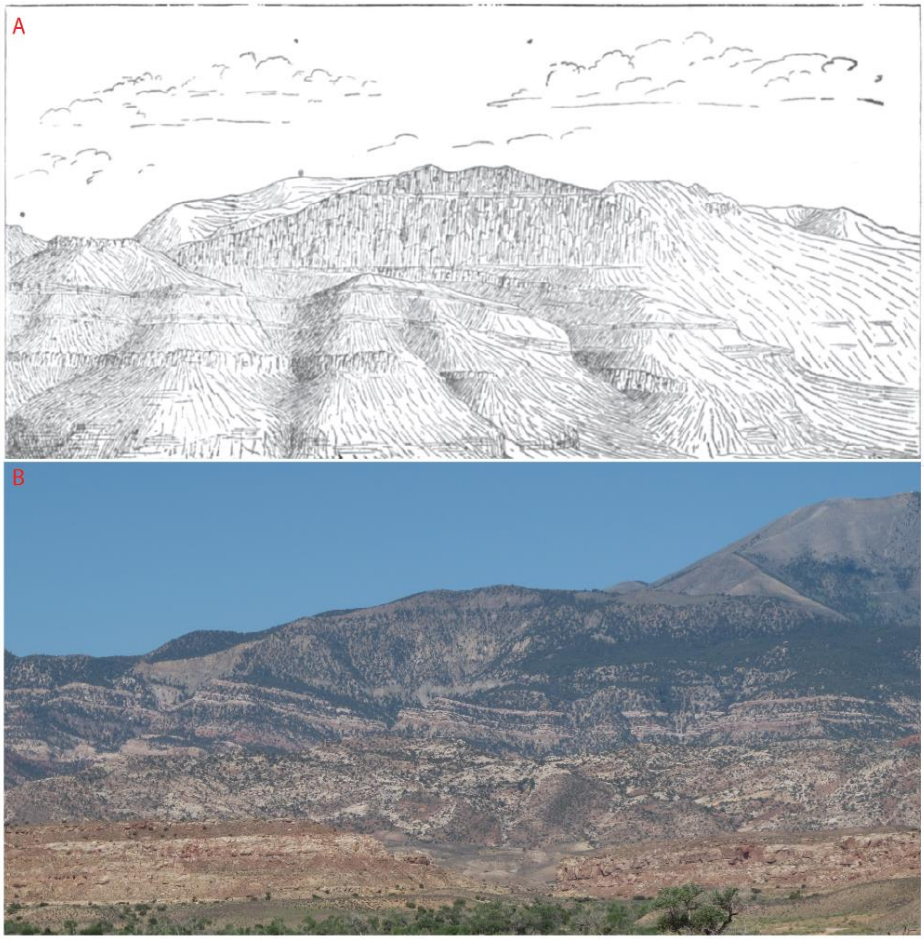

Figure 5. A: Sketch by Gilbert (1877) of CRL, which he referred to as the Peale laccolith. B: A photograph of CRL taken from the east of Mount Ellen. Both images show the cliff face that provides a natural cross section through the laccolith.

Defining the Term Laccolith

Gilbert (1877) described an idealized laccolite, now referred to as a laccolith, as being roughly circular in map-view, and concave downward with a flat roof and floor in cross section, noting that in some cases the upper boundary may undulate (Figure 6). Gilbert (1877) noted that smaller, thinner dikes and sills commonly accompany laccoliths, and suggested these dikes and sills may be the means by which magma reaches the place where a laccolith forms. In addition, laccoliths may intrude above or below already existing laccoliths, further offsetting the sedimentary strata.

Corry (1988) expanded on the definition of laccolith using various studies on igneous intrusions and noted that a continuum exists between sill and laccolith geometries. He suggested that laccoliths are always thicker than 30 m, and sills tend to be about 1-10 m thick. The term protolaccolith describes an intrusion that falls between the 10 and 30 m thicknesses; Trachyte Mesa on Mount Hillers in the Henry Mountains is an example of a protolaccolith. Corry (1988) also noted that laccoliths do not always fit the idealized structure as defined by Gilbert (1877). Laccoliths can be symmetric or asymmetric in map and cross-sectional view.

Corry (1988) noted several important characteristics of laccoliths:

1) The intrusion generally follows bedding planes;
2) The intrusion can be symmetric or asymmetric and "plano-convex, or doubly convex, lens flattened" in cross sectional view and in map-view can be circular or irregular;
3) The overlying host rock is vertically displaced due to the intrusion of the magma.

Based on these characteristics, I believe that the characterization of the Copper Ridge intrusion as a laccolith is accurate. Copper Ridge meets the size requirements of Corry's (1988) definition, and, as there are no requirements that the intrusion is symmetrical in map or cross-sectional view, it meets shape requirements as well.

Figure 6. Sketches of idealized laccolithic intrusions (from Gilbert, 1877): A: Simple idealized laccolith. B: Laccolith with associated dikes and sills. C: Stacked laccoliths showing deformation of the overlying strata.

Previous Work on the Henry Mountains

Previous work on the Henry Mountains has focused on understanding how shallow igneous intrusions form. The first major studies on the five intrusive centers focused on the geology of the region, and the authors proposed construction models for the intrusive bodies (Gilbert, 1877; Hunt, 1953). Gilbert (1877) and Hunt (1953) proposed the conflicting laccolithic and stock emplacement models, respectively. Jackson and Pollard (1988) used the geology of the Henry Mountains to test both hypotheses, and concluded that the laccolithic emplacement model was largely supported. The aim of this study is to reconstruct the emplacement history of CRL on Mount Ellen. Observations from the work of Gilbert (1877) and Jackson and Pollard (1988) will be used to do this as accurately as possible.

Recent work on the Henry Mountains focuses on sheeted intrusions, many of which have similarities to CRL. The studies provide observations that the authors interpreted as support for the pulsed construction model suggested by Gilbert (1877). Observations similar to those in these studies are present on CRL, and the studies utilize some of the methodology used in this project (Horsman et al., 2005; Saint-Blanquat et al., 2006; Morgan et al., 2008; Horsman et al., 2010). Several of the studies proposed construction models for the intrusions of interest and, where applicable, those models will be used to understand how CRL likely formed.

Laccolith-Stock Debate

Gilbert (1877) noted that the magma that formed the Henry Mountains was different from magmas that extrude onto the surface of the earth. The author hypothesized that magma intruded concordantly at depth, likely fed by a feeder dike, and made space for itself by lifting and deforming the overlying sedimentary strata, a process that he first suggested (Figure 6). Gilbert (1877) noted that the sedimentary strata bend over the intrusion and, in some cases, the new

orientation and geometry mimic the geometry of the underlying intrusion. As more magma intrudes, the displacement of overlying strata increases. Gilbert (1877) hypothesized that the main components of the five Henry Mountains are laccolithic intrusions.

After constructing the first geologic map of this area, Hunt et al. (1953) made observations that challenged Gilbert's (1877) conclusions. Hunt et al. (1953) hypothesized that the mountains consist of a large, discordant stock that fed surrounding intrusions (Figure 7). The stock would have intruded vertically and expanded, creating an area of extremely metamorphosed rock referred to as the shatter zone. Hunt et al. (1953) hypothesized that bulges on the sides of the stock were the sites of radial intrusion initiation and growth, and magma supplied by the stock spread out and formed laccoliths (Hunt et al., 1953).

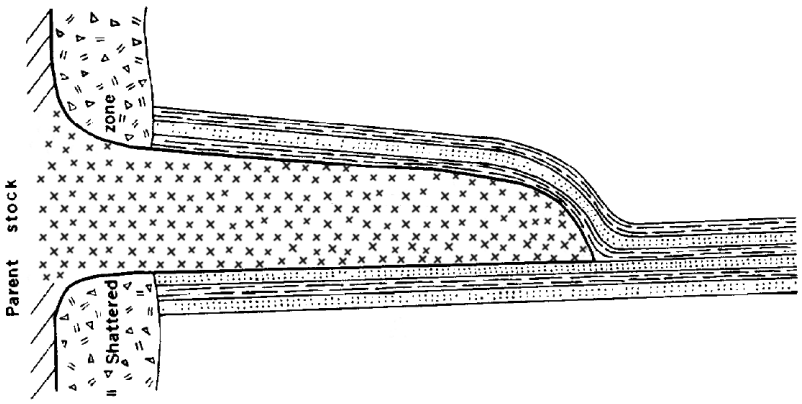

Figure 7. Sketch of the stock, shatter zone, and laccolith as suggested by Hunt et al. (1953; figured modified from Hunt et al., 1953).

Jackson and Pollard (1988) used the characteristics of the Henry Mountains to test the contradictory hypotheses of Gilbert (1877) and Hunt et al. (1953). Data from their study suggested that the vertical growth of a laccolith deformed the sedimentary strata, rather than the outward growth of a stock (Jackson and Pollard, 1988). The sedimentary strata show hinges on

both sides of the laccolith, which is consistent with Gilbert's (1877) findings. Structures, such as buckle folds, would be present if horizontal compression from stock emplacement had occurred; however, they are not present. In addition, paleomagnetic data from some sills showed that they were emplaced into horizontal strata and were rotated after inflows of subsequent magmatic pulses (Jackson and Pollard, 1988). Overall, the data from Jackson and Pollard (1988) support the laccolithic growth model.

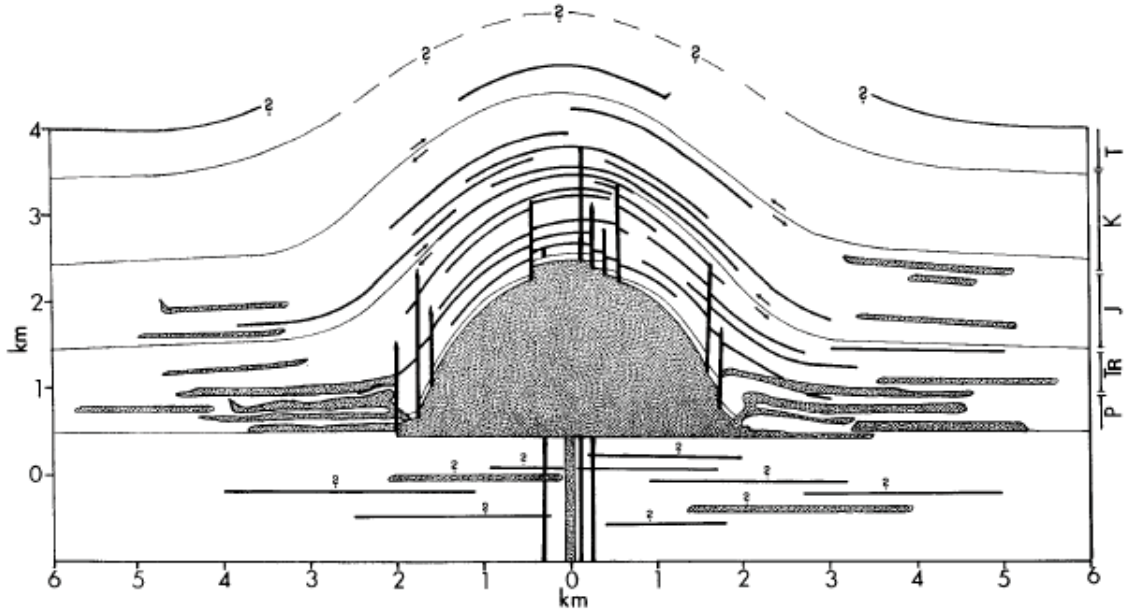

Figure 8. Schematic cross section of a Henry Mountains central intrusion with doubly hinged sedimentary beds and tilted sills above the intrusion (from Jackson and Pollard, 1988).

Recent Work on the Henry Mountains

Recent studies provide examples of shallow intrusions that were built through several pulses of magma (Coleman et al., 2004; Glazner et al., 2004; Michel et al., 2008; Rocchi et al., 2010; Saint-Blanquat et al., 2011). Pulsed construction can lead to step-wise growth of intrusive bodies. For example, an intrusion constructed through pulses of magma may start out as a sill and, through subsequent injections of magma, may grow to be a laccolith (Horsman et al., 2010).

The different geometries of intrusions have varying characteristics, including volume of magma and interaction with the host rock, and can show increasing complexity with increasing size. Studies on several intrusions in the Henry Mountains, including the Maiden Creek sill, the Trachyte Mesa laccolith, and Black Mesa bysmalith reveal the complexities and characteristics of such intrusions (Horsman et al., 2005; Saint-Blanquat et al., 2006; Morgan et al., 2008).

Horsman et al. (2005) described the Maiden Creek sill on the eastern margin of Mount Hillers. Through field observations, several key characteristics were observed: solid-state deformation at igneous-igneous contacts; presence of intercalated sedimentary rocks between the sheets; and continuous bulbous terminations at the margins of the intrusion. The aforementioned characteristics provided evidence for the hypothesis that the Maiden Creek sill is the result of pulsed construction. Using a suite of techniques to determine magmatic fabric orientation, Horsman et al. (2005) found that magma likely originated from a feeder to the west and flowed from the center of the main body and outward to several finger-like lobes that surround the main body. These authors also found that most of the lineations were subhorizontal, likely resulting from flattening that occurred during magma spreading and vertically displacing the overburden.

The Trachyte Mesa intrusion, studied by Morgan et al. (2008), is a protolaccolith on the eastern margin of Mount Hillers. The intrusion is asymmetric and tongue-shaped in map-view, similar to CRL, with a relatively flat roof. Magnetic fabric data suggested that a feeder from Mount Hillers fed the intrusion, and magma traveled from the southwest to the northeast. The sheets intruded sub-horizontally, each above earlier sheets, and different sheets are separated by contacts marked by intense cataclasis (Morgan et al., 2008). The tip of the intrusion has a bulbous termination, and the sedimentary host rock has been deformed and bent to accommodate the intrusion.

Saint-Blanquat et al. (2006) studied the Black Mesa bysmalith on the eastern margin of Mount Hillers. The intrusion is cylindrical and the eastern contact is fault bounded. Textural and fabric differences through the intrusion provided evidence for a pulsed construction. Their emplacement model proposed that the intrusion began as a sill and grew larger through progressive under-accretion of new sheets. Faulting and deformation of the host rocks allowed for accommodation of the intrusion. Emplacement occurred rapidly, possibly in less than 100 years (Saint-Blanquat et al., 2006).

Horsman et al. (2010) suggested a model of pulsed construction of idealized upper-crustal intrusions and the evolution of smaller intrusions into larger intrusions, based on studies on the Maiden Creek sill, the Trachyte Mesa laccolith, and the Black Mesa bysmalith. The important differences between these types of intrusions are the total volume of magma emplaced, and the deformation of the host rock. In addition to these differences, the temporal component of intrusion formation differs between intrusion types. A direct correlation exists between magma volume and duration of intrusion formation (Saint-Blanquat et al., 2011). Therefore, smaller intrusions, such as a sill, will form more quickly than a larger intrusion, such as a bysmalith.

A sill forms when a small volume of magma spreads away from the feeder in finger-like lobes (Figure 9; Horsman et al., 2010). Successive small pulses of magma may intrude, and will likely follow the same path as the initial pulse. Slight bending of the host rocks may occur along the edges of the intrusion. Additional pulses of magma or larger volumes of magma can cause the sill to evolve into a laccolith (Figure 9; Horsman et al., 2010). Similar to the sill, subsequent pulses of magma will tend to intrude along the same paths as previous pulses, and spread to about the same extent. Due to the increased size of the intrusion, wall rock bending, uplift, and deformation around laccolithic intrusions is more extensive. Increasing the magma supply can

lead to a bysmalith (Figure 9). Subsequent injections of magma lead to steepened margins, and the displacement of the host rock increases (Horsman et al., 2010). At a certain point, a fault forms in order to accommodate the increase in vertical relief, and the overburden is displaced in a piston-like manner.

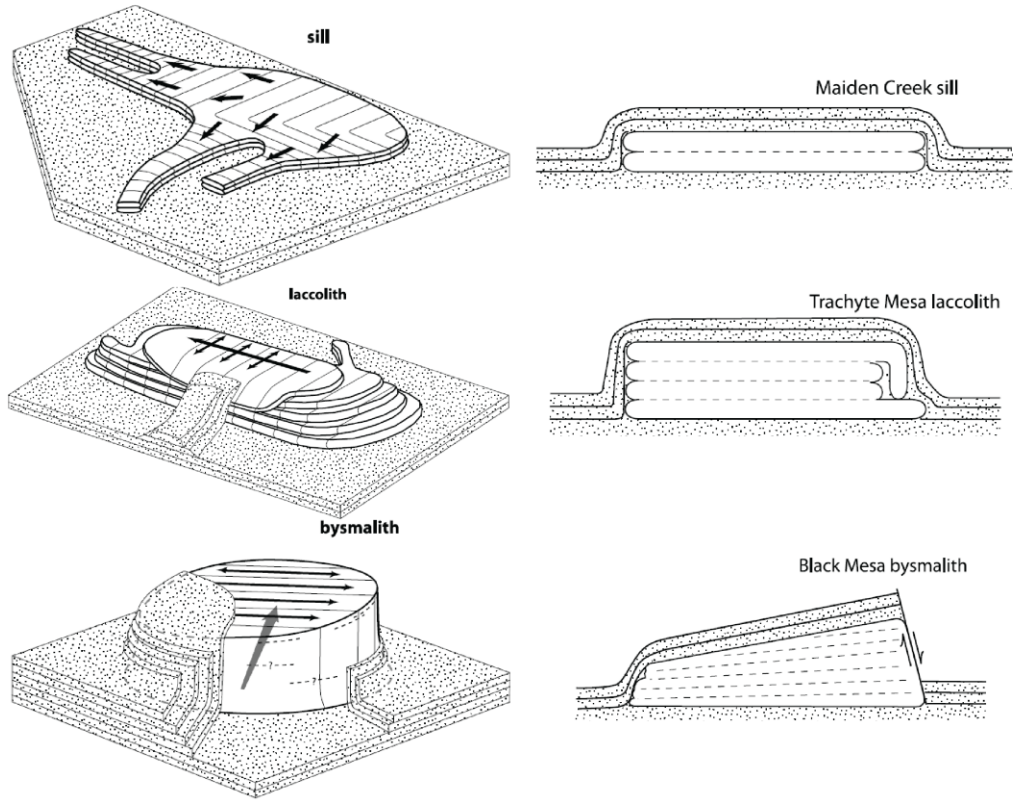

Figure 9. Idealized sill, laccolith and bysmalith block diagrams and examples of such intrusions (modified from Horsman et al., 2010). Note the relationships between the host rock (stippled) and the intrusive rocks. Intrusions are not to scale.

Magma Ascent and Laccolith Emplacement

Petford et al. (2000) and Vigneresse and Clemens (2000) discuss the formation, transport (ascent), and emplacement of magma. These are the main aspects of the construction history of CRL focused on in this project. Corry (1988) focuses on the vertical ascent and the emplacement of the magma, and the subsequent growth into a laccolith. He splits the process into four stages: 1) vertical ascent of the magma; 2) transition of magma movement from vertical to horizontal; 3)

progression and termination of horizontal movement and beginning of thickening; and 4) deformation of the overburden occurring with stages 2 and 3. This paper will focus on the first three stages.

Vertical Ascent of Magma

Magma ascent is an essential process in the formation of laccoliths, and much work has focused on how the magma ascends to the emplacement site. Magma flow through a crack or dike is one favored mechanism. Some studies suggest that magma emplacement may cause fracturing of the host rock and the magma propagates through the fracture. Magma may also then propagate through pre-existing fractures (Cook and Gordon, 1964; Pollard, 1977; Clemens and Mawer, 1992). A simpler approach by Petford et al. (1993) suggests that pre-existing faults and fractures act as the conduits for magma ascent.

As the magma ascends, and the temperature drops, viscosity increases exponentially. Therefore, rapid ascent to the shallow crust is essential for the magma to remain fluid enough to intrude. Slow ascent would likely lead to the magma solidifying at depth. A low viscosity is important to maintain because as the viscosity increases, drag against the wallrock increases, which decreases ascent speed (Pitcher, 1978). Many factors contribute to magma maintaining a viscosity that allows free flow to continue (Pitcher, 1978). One such factor is H_2O content; an increase in the H_2O content decreases viscosity (Clemens and Petford, 1999). A lower viscosity magma will move through a dike more rapidly than a more viscous magma (Petford et al., 1993). Additionally, a more pressurized magma will ascend through the crust rapidly, allowing the magma to reach the surface before solidifying.

Another important factor to consider when discussing ascent is the depth at which magma originates. Corry (1988) notes that a common assumption is that the source area for magma is at least at 30-50 km depth, generally about the thickness of the continental crust. The velocity of ascent and the depth of generation are both important in keeping the magma fluid through ascent. Petford et al. (1993) calculate critical dike widths that are required for magmas of a certain viscosity and density to ascend from an assumed 30 km of depth and remain fluid enough to begin emplacement. Therefore, in order for the vertical ascent to occur, and to reorient to horizontal emplacement, a certain dike width must exist to facilitate rapid ascent to prevent freezing of the magma.

Transition of Magma Movement from Vertical to Horizontal

As magma movement transitions from vertical to horizontal, ascent ceases and emplacement begins (Petford et al., 2000). Corry (1988) suggests that the magma reaching the theoretical neutral buoyancy level may cause a magma to emplace at a certain location. The neutral buoyancy level is the location in the crust where the host rock and magma have equal buoyancy and ascent will cease. However, Vigneresse and Clemens (2000) note that the neutral buoyancy level for granitic magmas does not exist in the shallow crust. Therefore, this cannot be the sole mechanism for emplacement of all magmas. Menand (2011) suggests other factors that may control where horizontal movement initiates, including the rheology-contrast, stress, and rigidity-contrast controls. Rheology-contrast control and stress control were not likely at work during the emplacement of the Henry Mountains because the intrusions formed in brittle upper crust, and there was no syn-emplacement regional deformation, respectively.

Rigidity-contrast control refers to the instances where the competency contrast between two sedimentary layers causes magma to intrude at a contact (Menand, 2011). Menand (2011)

suggests that this is likely one of the most common controls on where magma emplaces. When magma reaches a contact between a more competent rock above and a less competent rock below, it may intrude along that contact. This is not always the case, as evidenced in the work by Kavanagh et al. (2006). The laboratory results revealed that in some cases the water (magma) behaved as suggested. In other cases, the water stopped at the contact and it did not intrude. In a case where a weaker layer was on top of a stronger layer, the water continued to intrude as a dike, past the contact. Other factors that may contribute to magma emplacing at certain locations in the crust include preexisting weaknesses, such as fractures or bedding planes within a rock layer, and syn-emplacement fracturing in the host rock.

Progression and Termination of Horizontal Movement and Initiation of Thickening

Emplacement specifically refers to the space-making mechanisms that displace the host rock, and allow the intrusion to grow to its final geometry (Horsman et al., 2010). Once magma begins intruding horizontally, the magma must make space for itself in order to continue growing. For some time the space making mechanisms for shallow crust intrusions were not well understood. One early suggestion for the progression of a small intrusion, such as a sill, into a larger intrusion, such as a laccolith, was that when the intrusion reached a certain lateral extent it would begin to inflate into a laccolithic intrusion (Johnson and Pollard, 1973; Pollard and Johnson, 1973). It was hypothesized that at some critical extent the intrusion would have enough leverage to begin lifting the overburden. However, recent studies have found that more factors are involved in the transition from sill to laccolith (Rocchi et al., 2002; Horsman et al., 2010).

Rocchi et al. (2002) cite magma-supply rate, depth of emplacement, magma trap availability and space-making mechanisms as important factors for intrusion growth. During emplacement, the aforementioned factors contribute to the transition from a sill to a laccolithic

intrusion. Horsman et al. (2010) also consider emplacement rate as a major factor in the emplacement and growth processes; the authors also include wallrock lithology as a major factor. With a higher emplacement rate, the magma is more pressurized and the intrusion can grow larger than an intrusion emplaced at a slower rate. In addition, an intrusion may progress into a larger intrusion in a less competent rock, such as shale, whereas an intrusion may remain smaller if it intrudes a more competent rock, such as a sandstone.

Methods

In this section, I will describe the methods used to test my hypotheses, and devise the construction history of CRL. To test the hypothesis that CRL was constructed through two or more separate pulses of magma, I used a combination of field work, crystal size distribution, and geochemical analysis. To test the hypothesis that the intrusion was fed from a lateral feeder and deformed the sedimentary strata, I used a combination of field work, anisotropy of magnetic susceptibility, and x-ray diffraction.

Field Work

Field work was used to create a detailed geologic map of CRL. Previous work on Mount Ellen has not focused solely on CRL, resulting in more generalized (Hunt et al., 1953), and incomplete (Morton, 1984, 1986) maps of CRL. Morton (1984, 1986) mapped the entire Mount Ellen quadrangle; however, CRL lies along its boundary with the Raggy Canyon quadrangle, leaving half of CRL unmapped. My geologic map created in the field was digitized using ArcMap. Additionally, multiple cross sections through the intrusion were created to show overall geometry.

Field work also included collection of oriented samples, observation of igneous rock characteristics, measurement of foliations and lineations, and measurement of bedding in sedimentary units. Important details about the igneous rocks observed in the field include color of the matrix, relative size and abundance of phenocrysts and xenoliths, and the mineralogical composition of the phenocrysts. A cursory grouping of rocks into the upper and lower sheets was created using these characteristics. The grouping was then compared to the location of the

outcrop on the geologic map. This work and supplemental laboratory work led to a definitive identification of the upper and lower sheets.

Another important aspect of field work was observing the sedimentary rocks. Special consideration was given to the Tununk shale, the host rock for CRL. The Tununk shale is preserved as cap rock, within the laccolith, and under the laccolith. Contacts between the Tununk and igneous rocks were noted and carefully plotted on the geologic map. Contacts were also used to understand how the intruding magma interacted with the host rock. When observing the preserved Tununk special care was taken to note any metamorphism, and any spatial differences in the degree of metamorphism. Another subset of field work was to observe the sedimentary rocks and compare them with the detailed descriptions provided by previous studies.

Crystal Size Distribution

Crystal size distribution (CSD) analysis provides a quantitative measurement of rock texture and can help differentiate between superficially homogenous igneous rocks (Cashman and Marsh, 1988; Marsh, 1988, 1998; Higgins and Roberge, 2003; Mock et al., 2003). Data from CSD can be used to estimate crystal growth and nucleation rates, and the information can constrain the thermal history of the magma (Cashman and Marsh, 1988; Marsh 1988, 1998; Higgins, 2000; Higgins and Roberge, 2003). Separate pulses of magma may have distinct thermal histories; therefore, variations in CSD between samples can indicate that the rocks formed from different magma pulses. Several studies have used CSD on igneous rocks (e.g. Cashman and Marsh, 1988; Mock et al., 2003), and recently CSD has been used in several studies of Henry Mountains igneous rocks (Gwyn, 2011; Broda, 2014; Thornton, 2015). In the recent Henry Mountains work, the authors identified multiple CSDs in their field areas, and hypothesized that the igneous bodies formed from distinct magma pulses.

CSD analysis works by measuring phenocryst dimensions on a planar surface, and dividing those phenocrysts into groups based on a selected size interval. The abundance of phenocrysts within certain size intervals gives the population density. The natural logs of the population densities are plotted as a function of grain size to produce a CSD curve. The shape, slope, and y-intercept of the CSD curve can be interpreted to provide information about the crystallization history of the magma. The shape of the CSD curve can reveal complexities in the crystallization history. Straight CSD curves can indicate a steady-state cooling (Marsh, 1998; Higgins and Roberge, 2003). Curves that maintain a consistent slope for a portion of the line, but then shallow out significantly, may be the result of textural coarsening at depth (Higgins, 1998). Concave up curves may also result from textural coarsening (Higgins and Roberge, 2003), and also may result from magma mixing (Higgins, 1996). The slope of the curve provides information about residence time, and the y-intercept provides information about the nucleation density.

For this study, CSD was measured for six samples from the upper sheet, six samples from the lower sheet, and one sample from an intrusion adjacent to CRL. All samples were cut so that a flat, fresh surface was exposed. The surfaces were scanned at high resolution. Binary versions of the scanned images were created using the computer program ImageJ. The binary images allowed for the plagioclase phenocrysts to be isolated; the plagioclase crystals showed up as black and the rest of the rock was white. The image was then despeckled to avoid fragmentation of phenocrysts, and any large xenoliths were removed from the image. ImageJ then measured the dimensions of each phenocryst based on a set of minimum and maximum size parameters. Data from ImageJ were imported into a program called CSD Corrections (Higgins, 2000). The program produced numerical and graphical representations of the abundances of plagioclase

phenocrysts within certain size ranges. Data from all samples were plotted together, allowing relationships between samples to be recognized.

Geochemistry

Whole-rock major and trace element compositions of 16 samples were obtained commercially by inductively coupled plasma-mass spectrometry (ICP-MS) from Acme Analytical Laboratories. Samples were selected as follows: six from the upper sheet, six from the lower sheet, and four thought to be from adjacent intrusions. Upon further investigation, two of the non-CRL samples are now considered to be from the upper sheet of CRL. The selection process aimed to test for chemical variations between the upper and lower sheets and to distinguish other intrusions from the main CRL body. Special care was taken to choose samples that were as fresh as possible.

Anisotropy of Magnetic Susceptibility

In the Henry Mountains, field fabrics are sometimes absent or difficult to measure, making field data sparse. Measuring anisotropy of magnetic susceptibility (AMS) allows for a more detailed and complete representation of igneous fabrics. AMS data give information about the magnetic fabric within a rock, which can be used to infer magma flow characteristics (Bouchez, 1997). Previous studies have used AMS to study fabrics and infer magma flow characteristics in the Henry Mountains and similar intrusions (Knight and Walker, 1988; Horsman et al., 2005; Saint-Blanquat et al., 2006; Stevenson et al., 2007; Morgan et al., 2008; Thornton, 2015).

It is important to consider the magnetic minerals that control the AMS in a rock when interpreting the data (Rochette et al., 1992). Michael Petronis at New Mexico Highlands

University tested two samples from CRL. Testing involved heating the samples, and then cooling them, measuring susceptibility values throughout the course of temperature change. The data reveal a pattern consistent with that of magnetite (Figure 10). The same test on igneous rocks from the Henry Mountains in previous studies and those data suggest that the main ferromagnetic mineral grains are multi-domain magnetite (Horsman et al., 2005).

To collect AMS data, a rock specimen is subjected to an induced magnetic field. The magnetic minerals within the sample cause perturbations in the induced magnetic field (Rochette et al., 1992; Tarling and Hrouda, 1993). The magnetic susceptibility (K) is based on a ratio of the induced magnetization and the inducing magnetic field, and it is a unitless quantity represented by SI. The magnetic properties within a sample may vary spatially, so data are visualized as an ellipsoid with long, intermediate, and short principal axes, referred to as K_1, K_2, and K_3, respectively. The ellipse represents the magnetic fabric within the samples. The magnitudes of the axes are used to calculate scalar parameters, defined as:

$$K_m = \frac{K_1 + K_2 + K_3}{3}$$

$$T = \left[2 \frac{\ln\left(\frac{K_2}{K_3}\right)}{\ln\left(\frac{K_1}{K_3}\right)} \right] - 1$$

$$P_j = \exp(2[(\eta_1 - \eta_b)^2 + (\eta_2 - \eta_b)^2 + (\eta_3 - \eta_b)^2]^{1/2}$$

$$L = \frac{K_1}{K_2}$$

$$F = \frac{K_2}{K_3}$$

The abundance of magnetic grains is represented by bulk susceptibility (K_m). The mean shape factor (T) describes the ellipticity of the AMS ellipsoid: a perfect sphere has a T=0, an ellipsoid that is infinitely prolate has a T= -1, and an ellipsoid that is infinitely oblate has a T=1. The degree of anisotropy (P_j) represents the intensity of the magnetic fabric within the specimen. The magnetic lineation (L) and foliation (F) are represented by ratios that incorporate the principal axes.

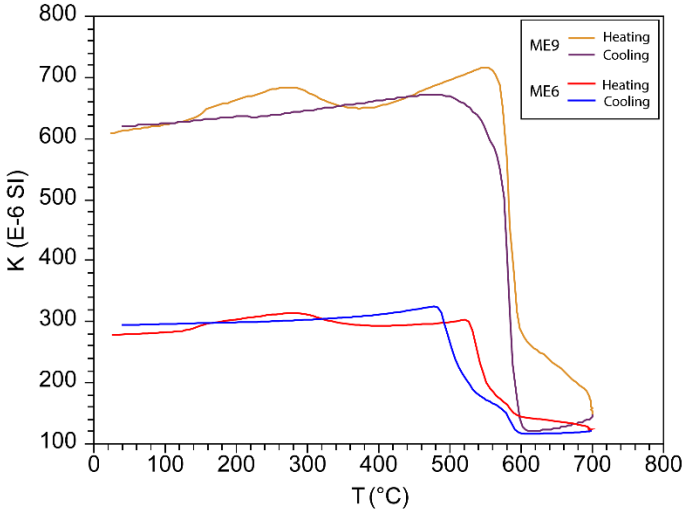

Figure 10. Plot of susceptibility vs. temperature for samples ME6 and ME9 from CRL. The heating and cooling cycles are noted in different colors. The sharp drop-off in both samples is indicative of magnetite.

AMS analysis was performed on forty-four oriented samples. From each sample, two to three 25-mm-diameter cores were drilled and oriented in the laboratory. Each core was cut into 22-mm-long specimens, resulting in five to six specimens from each rock. AMS was measured using an AGICO MFK1-A magnetic susceptibility bridge at East Carolina University. The SAFYR computer program provided with the instrument was used to collect the data. The AniSoft computer program was used to visualize the data. It shows the primary axes of the ellipsoid on a stereonet and provides magnetic parameters (K_m, T, P_j, L, and F). For this study,

data were used to make interpretations about magma flow during emplacement, and to compare the scalar parameters in the upper and lower sheets of CRL.

X-Ray Diffraction

The mineralogy of three samples of Tununk shale was determined using X-ray diffraction (XRD). XRD analysis was performed at East Carolina University. A transect consisting of three Tununk samples was taken the layer of Tununk preserved within CRL. Variation in the degree of metamorphism observed in the Tununk layer may provide insight into the thermal history of the host rock, and shed light on the intrusive history of CRL.

Results

Field Work

Copper Ridge Laccolith Geometry, Maps, and Cross Sections

Field observations were used to create a detailed map of the CRL region (Figure 11) and to construct cross sections (Figure 12). An annotated map of CRL with the main regions and features of CRL labeled is in Appendix A (Figure 47). The geologic map covers an area of 15.5 km^2. In map-view the upper sheet covers an area of about 3 km^2, and the lower sheet covers an area of about 4.8 km^2 (Figure 13). Both sheets have asymmetric tongue-like map-view geometries, generally fanning out from a point in the west-northwest toward the east-southeast. A portion of the upper sheet in the Garden Basin area is at the same elevation as some of the lower sheet, and appears to be detached from the main body. In cross sectional view the upper sheet has a relatively flat floor, and a dome shaped upper contact (Figure 12). The lower sheet also appears to have a flat floor with a domed upper contact. The lower sheet has a flatter roof than the upper sheet.

An easily recognized layer of Tununk separates the upper and lower sheets, and on the main ridge of CRL, Tununk cap rock can be observed. In one location to the southeast, the bottom contact of CRL is exposed. Where Tununk is preserved, the bedding is generally subhorizontal, with dips ranging from 0° to 24°. Other sedimentary units maintain their horizontal to subhorizontal bedding, except locally near the margins of the intrusion (Figure 14). In many locations, the upper and lower contacts between the Tununk and the igneous rocks are directly observable (Figure 15). The top of the intrusion undulates gently, and mimics the topography of the main ridge. As the sheets pinch out to the north and south, the igneous/Tununk

contact cuts up-section in a stair-step geometry. In some locations, the bulbous termination of the upper sheet can be observed (Figure 16). Two sills, much smaller than CRL, are visible below the bottom sheet. Only one is of mappable size, and thick sedimentary strata (~100 m) separate the sills from the laccolith.

Magmatic fabric measurements were collected from igneous rocks where well-developed fabrics existed (Figure 17). The fabrics all had subhorizontal plunges. The trends of the fabrics are consistent down the main ridge. From the main ridge, magmatic fabric trends fan out radially towards the margins.

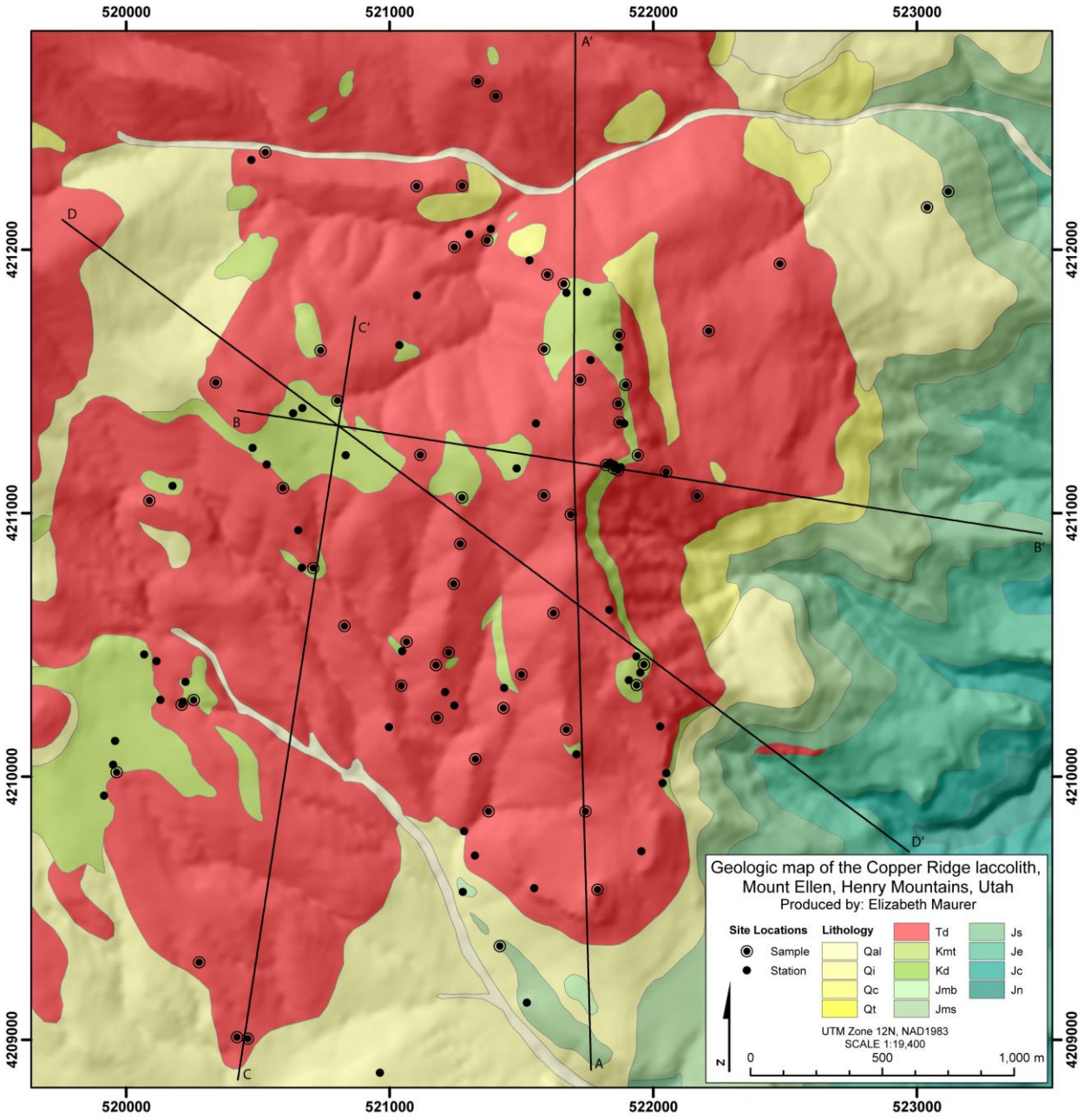

Figure 11. Geologic map of CRL area with station locations marked. Cross section lines A-A', B-B', C-C', and D-D’ are noted.

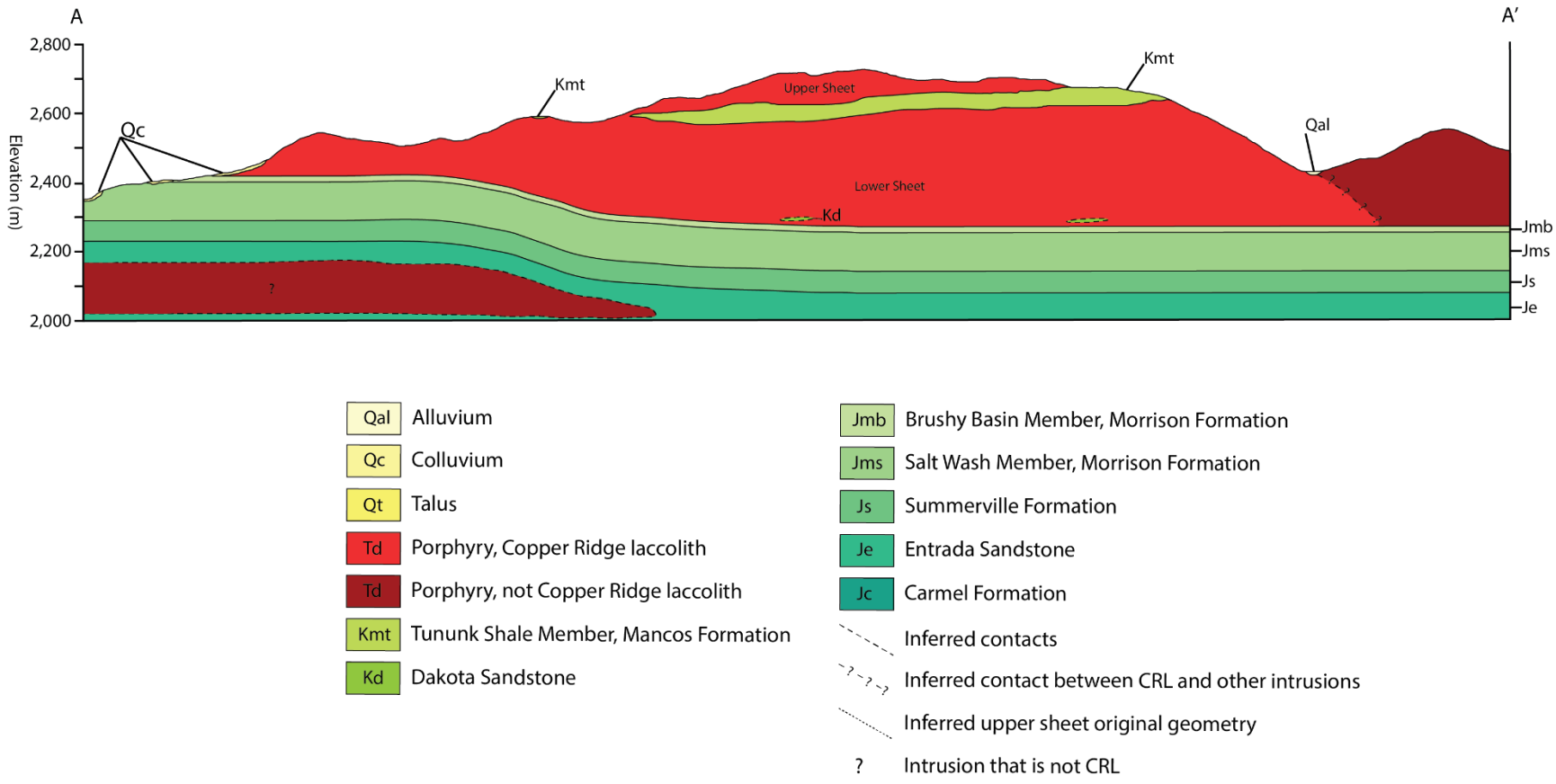

Figure 12. Cross sections (Transects from Figure 11) of CRL with no vertical exaggeration. A-A' transects the width of CRL, mimicking the orientation of the main cliff that exposes the natural cross section. B-B' transects the main ridge of CRL. C-C' transect shows the elevation differences in upper sheet rocks. D-D' transect shows CRL with the associated sill, and the central portion of Mount Ellen.

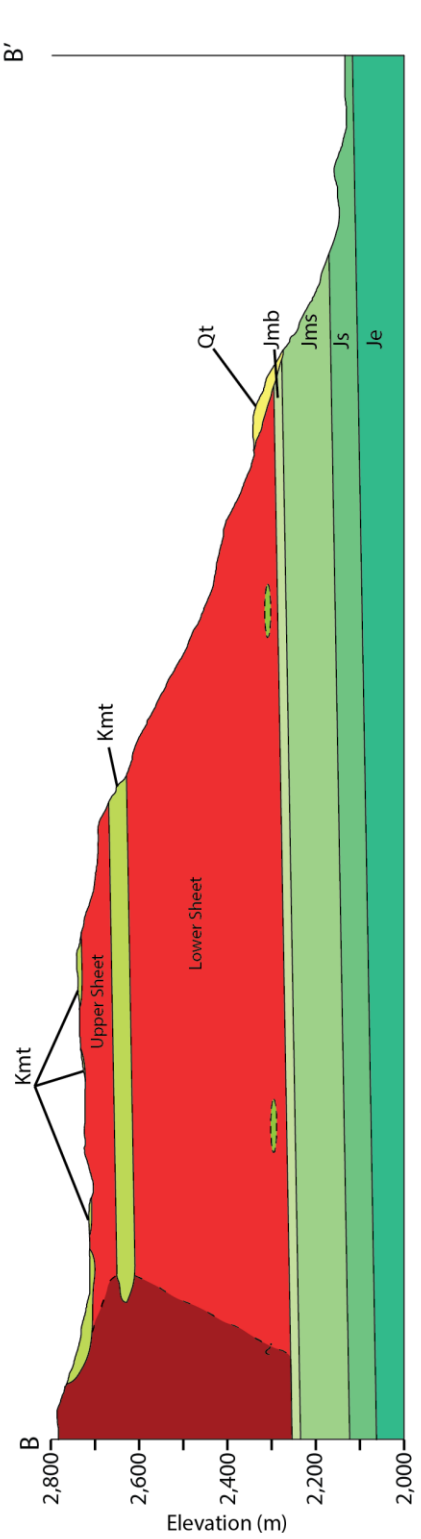
B
B′
Kmt
Upper Sheet
Lower Sheet
Kmt
Qt
Jmb
Jms
Js
Je
2,800
2,600
2,400
2,200
2,000
Elevation (m)

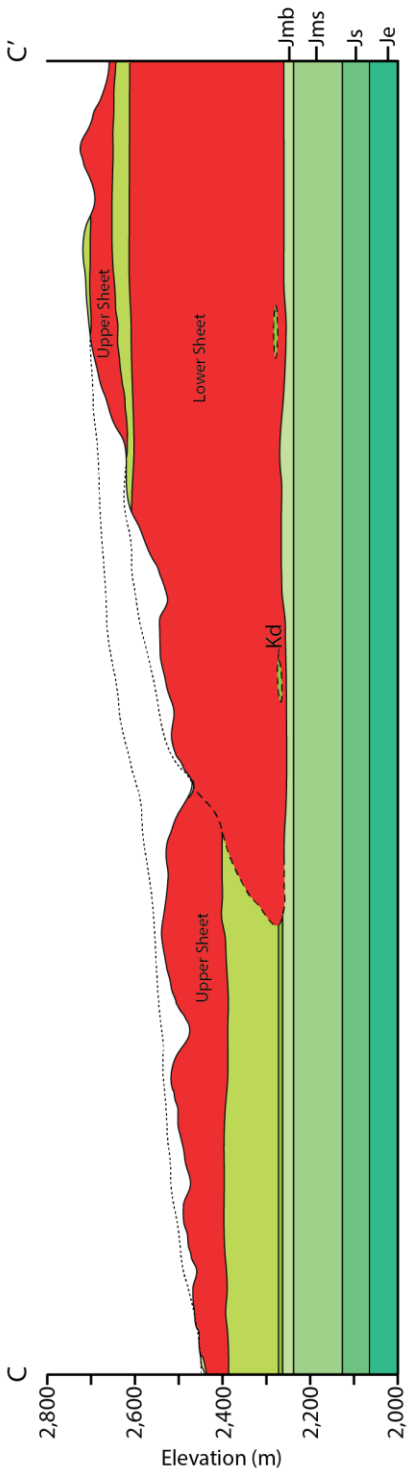
C
C′
Upper Sheet
Lower Sheet
Kd
Upper Sheet
Jmb
Jms
Js
Je
2,800
2,600
2,400
2,200
2,000
Elevation (m)

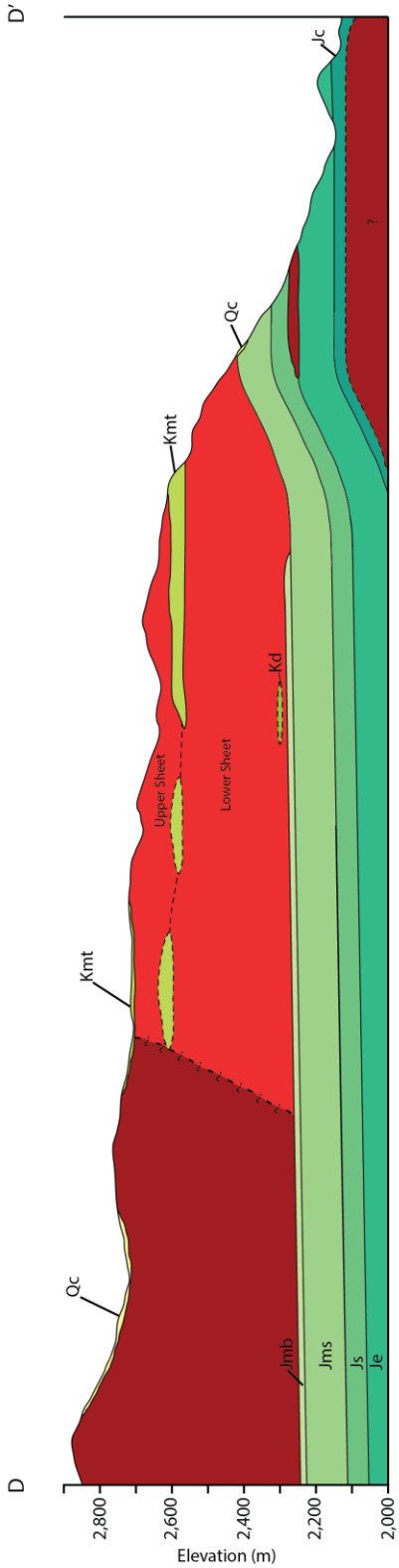
D'
D
Jc
?
Qc
Kmt
Kd
Upper Sheet
Lower Sheet
Kmt
Qc
Jmb
Jms
Js
Je
2,800
2,600
2,400
2,200
2,000
Elevation (m)

Figure 13. Gray-scale geologic map of CRL, showing the proposed aerial extent of the upper and lower sheets.

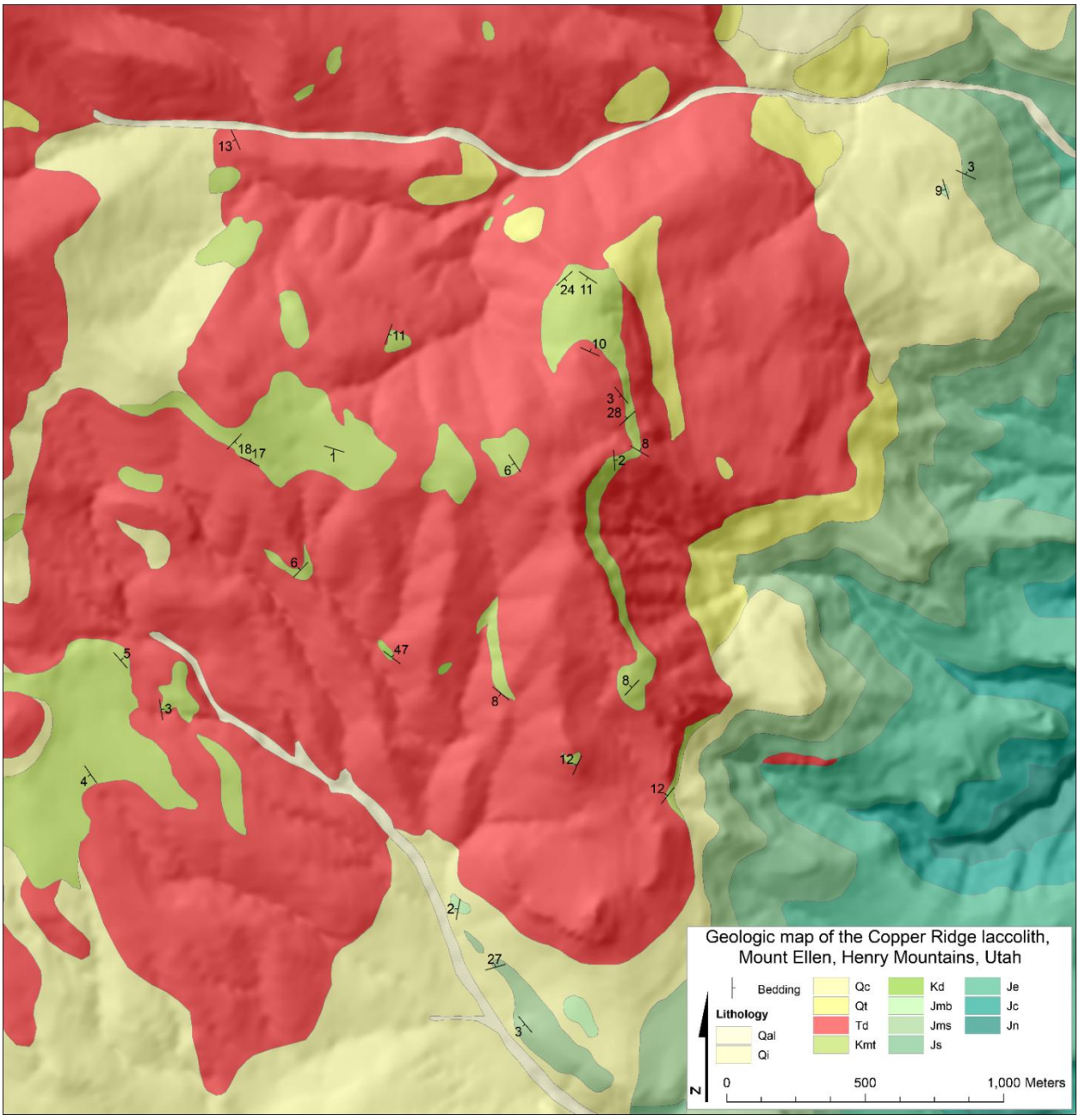

Figure 14. Geologic map with field-measured strikes and dips of bedding.

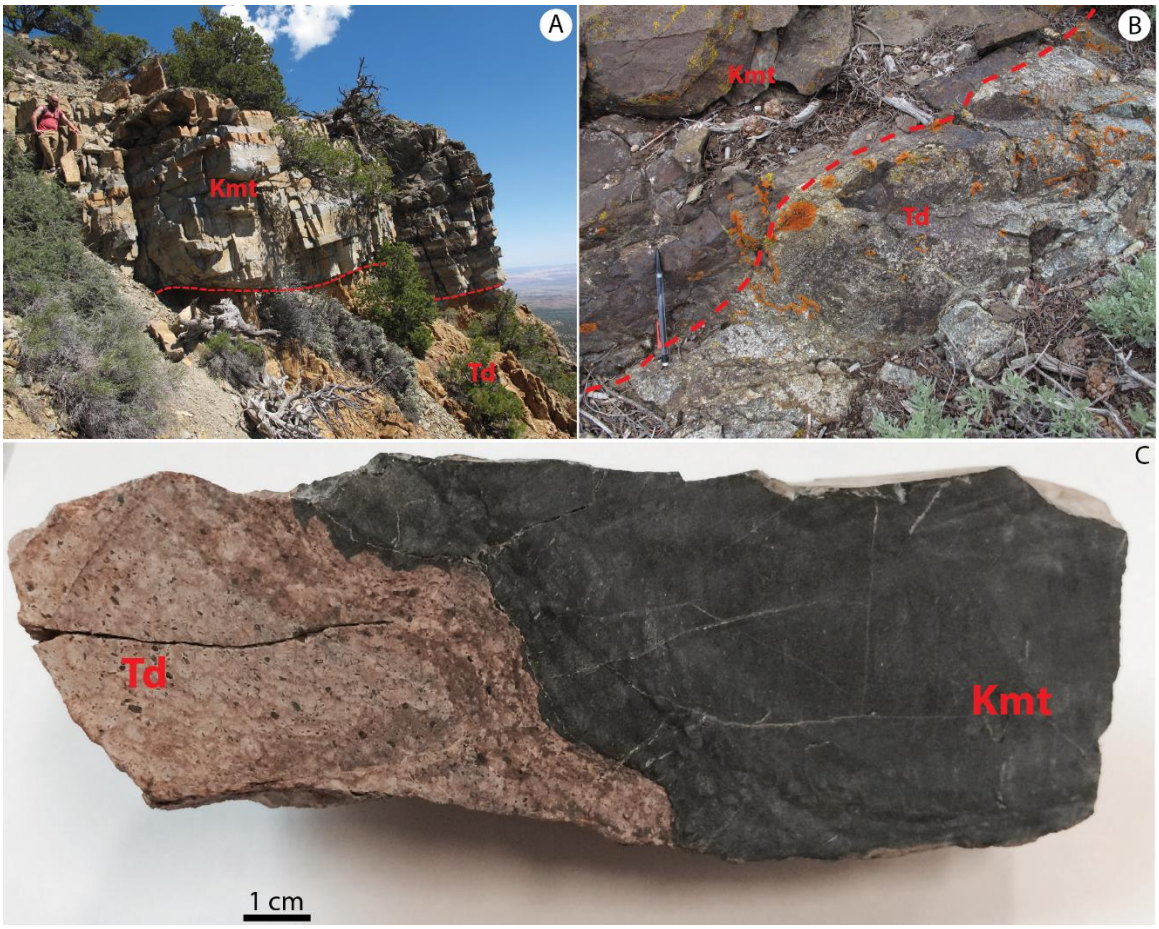

Figure 15. Images of preserved contacts between igneous rocks and Tununk. A: Contact between preserved Tununk and lower sheet of CRL (station CR22). B: Contact between Tununk over igneous rock (station CR16). Dashed red lines show the contact between the Tununk (Kmt) and igneous rock (Td). C: Contact between the lower sheet and the Tununk (station CR22).

Figure 16. Image showing the bulbous termination of the upper sheet against Tununk. The red line indicates the approximate location of the contact. Labeled in red are the igneous rocks (Td) and Tununk (Kmt).

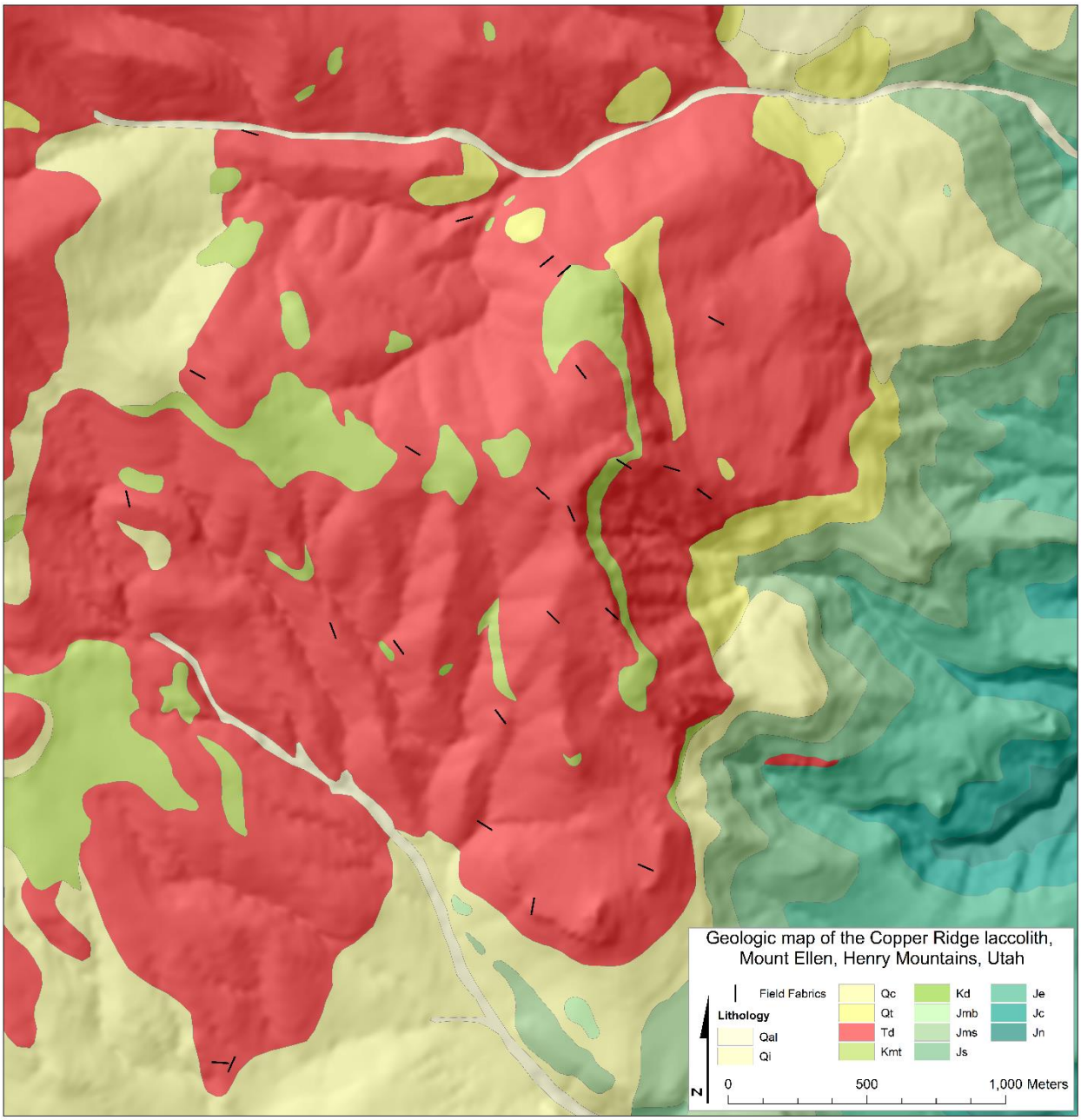

Figure 17. Magmatic fabric field measurements, all of which have subhorizontal plunges.

This new mapping builds on the work of Hunt et al. (1953) and Morton (1986) and remaps some incorrectly mapped sedimentary units, as well as the lateral extent of CRL. Hunt et al. (1953) mapped the northern boundary of the intrusion to extend north of the Copper Creek drainage and south to Ragged Mountain (Appendix A- Figure 48). However, the rocks observed in the Copper Creek drainage were not typical of CRL, and the southern margin does not extend to Ragged Mountain. In the northeastern region of the area, Morton (1986) mapped a ring of Dakota in the base of a drainage (Appendix A- Figure 49); the outcrops are actually Tununk (Figure 18). Morton's (1986) map also shows a semi-continuous layer of Dakota along the southern margin of CRL. In the field, no such layer was observed. Instead, several large Dakota lenses surrounded by igneous rocks are present. The bedding in the Dakota lenses (307/47NE) is generally steeper than the bedding in the Tununk and other layers.

Hunt et al. (1953) also originally hypothesized that the tip of CRL had been bent upwards during the intrusion of the Ragged Mountain bysmalith to the south of CRL. The location of this interpreted tip of CRL was adjacent to Ragged Mountain; however, upon investigation, it was clear that the igneous rocks near Ragged Mountain were not part of CRL. Farther away from Ragged Mountain on the southern tip of CRL, an area of extremely fractured rock appears to be tilted (Figure 19).

Figure 18. Tununk in drainage that Morton (1986) had mapped as a ring of Dakota (Appendix A). A portion of the outcrop has been removed (outlined in red) to show the black shale under the weathered surface.

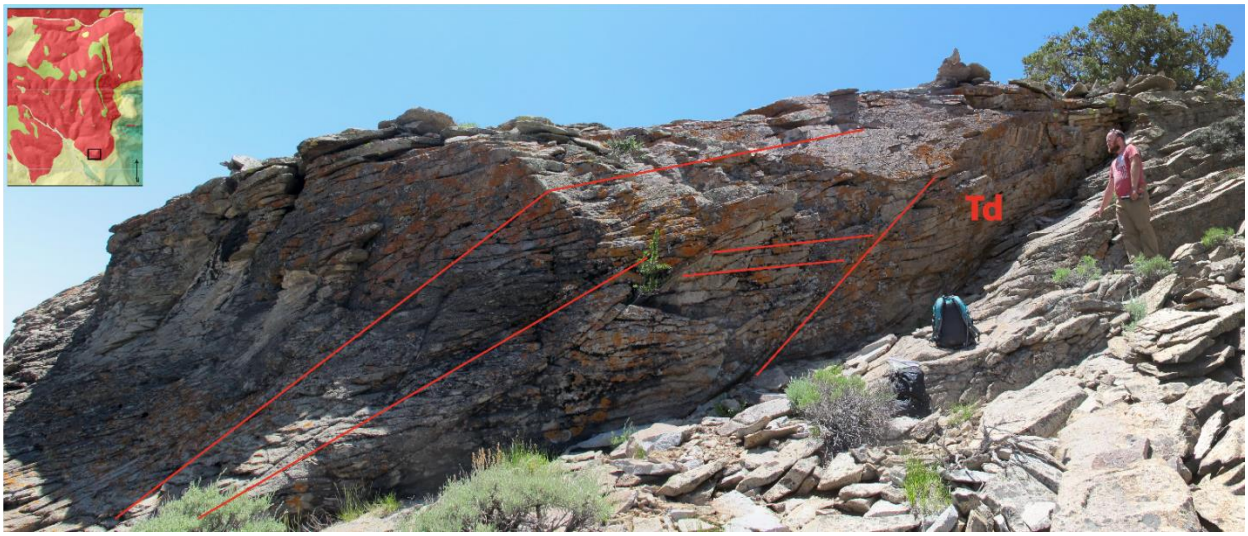

Figure 19. Stitched photograph of the extremely fractured igneous rock (Td) at the distal tip of CRL. Red lines outline some major fracture patterns present in the outcrop. Inset shows the location of the fractured tip on CRL outlined by a black box.

Igneous Rocks of the Copper Ridge Laccolith and Adjacent Intrusions

The upper sheet igneous rocks have plagioclase crystals up to 14 mm, and hornblende crystals up to 7 mm, surrounded by a dark gray matrix (Figure 20A). Within the rocks of the

upper sheet, large and abundant xenoliths (0.5-5 cm) of Proterozoic basement rock (Nelson and Davidson, 1993) are observed. The upper sheet weathers to generally massive orange-brown rock and is surrounded by large pieces of float (>6 cm) from the upper sheet (Figure 20C). In some places the rocks have quartz-filled vugs (<3 mm). Close to the host rock contacts, crystal size and abundance are greatly reduced in the igneous rocks.

The lower sheet igneous rocks have plagioclase crystals up to 8 mm, and hornblende crystals up to 4 mm, surrounded by a light gray matrix (Figure 20B). Basement rock xenoliths are far less abundant in the lower sheet, and only range up to 1 cm. The lower sheet weathers to white, almost vertical fins that are surrounded by gruss formed from lower sheet igneous rocks (Figure 20D, E).

Igneous rocks collected in the Garden Basin area are texturally similar to those from the upper sheet. However, these samples are at the same elevation as the lower sheet.

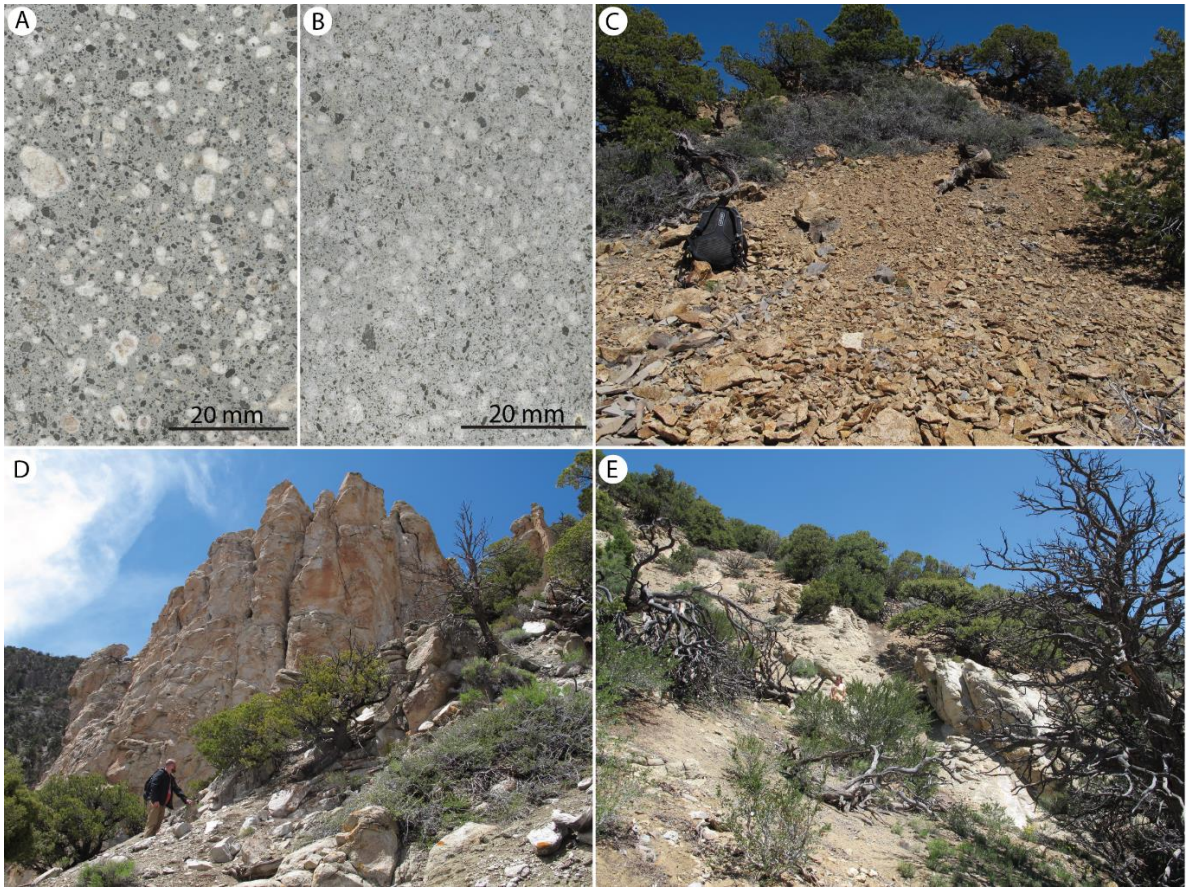

Figure 20. Physical differences between the upper and lower sheets of CRL. A: Texture of upper sheet igneous rock. B: Texture of lower sheet igneous rock. C: Example of weathering of the upper sheet. D, E: Examples of the weathering of the lower sheet.

On the northern side of the field area, a ridge previously mapped as part of CRL was found to differ in physical characteristics from both the upper and lower sheets. These rocks have a darker matrix, smaller plagioclase crystals, and far lower hornblende abundance (Figure 21A). In one location, the igneous rocks had several large shale and sandstone inclusions ranging in size from 2 cm to 10 cm (Figure 21B).

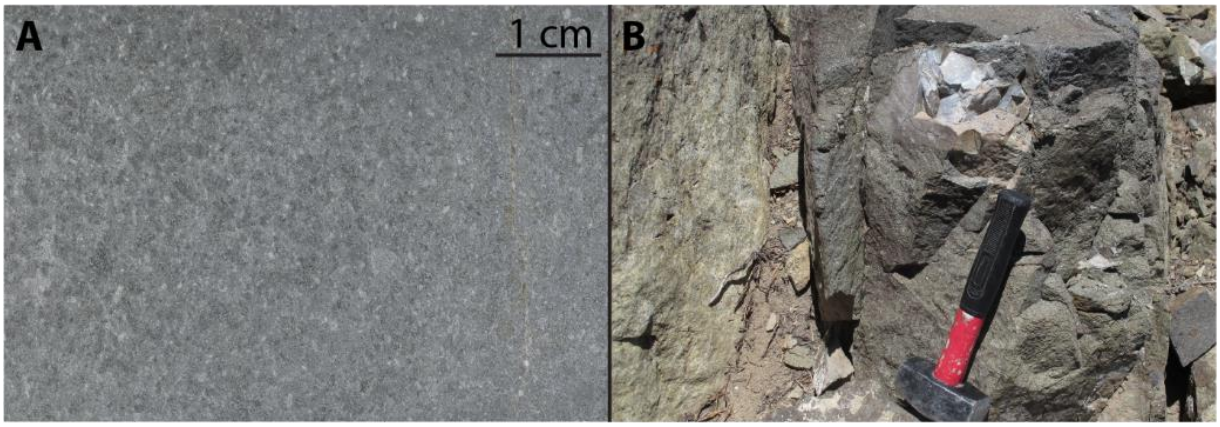

Figure 21. Physical characteristics of igneous rocks not from CRL. A: Scanned image of rock from the ridge north of CRL, showing color and texture. B: Picture showing large inclusion of sedimentary rock in igneous rock from the ridge north of CRL.

Sedimentary Rocks in the Field Area

The most abundant sedimentary rock in the field area is Cretaceous Tununk shale. The Tununk is a very fine-grained dark gray shale, locally containing abundant fossils, most predominantly ammonites (Figure 22). Throughout the thick layer of Tununk (~40 m) between the upper and lower sheets, differences in its physical properties exist. In many locations, the Tununk is metamorphosed to a very fine-grained, dark-gray rock. Toward the top and bottom of the layer, the Tununk is more metamorphosed than in the middle of the layer. The middle portion of the Tununk maintains shaley cleavage. The top and bottom have a mottled appearance (Figure 23), and narrow (< 1 mm wide) mineralized fractures (Figure 24). The lower portion of the Tununk exhibits small-scale faults, and appears to be more highly deformed and to have more fractures than the upper portion of the Tununk. Plumose structures are present locally near contacts. In one location, the Tununk contains extensive gypsum. The Tununk layer is folded in some areas, with visible fractures and a small detachment fold (Figure 25). The interlimb angles of the fold hinges increase closer to the tip of the intrusion: the first hinge is about 20°, the second about 60°, and the last, and closest to the tip of the intrusion, is about 120°.

Figure 22. Pictures of fossils in Tununk.

Figure 23. Picture showing mottled appearance in the Tununk adjacent to the contact with the lower sheet.

Figure 24. Image of metamorphosed Tununk sample, showing small-scale faults and calcite mineralized fractures.

Figure 25. Picture of folding in the Tununk, with some of the visible fold limbs marked by red lines.

Also observable in the field were Cretaceous Dakota sandstone, and the Brushy Basin and Saltwash members of the Jurassic Morrison formation. The Dakota exist in lenses (~10 m) surrounded by igneous rock and float. The sandstone contains abundant fossils (Figure 26B); also present were slickensides (Figure 26A). In most locations, Brushy Basin exists as a green, fine-grained unconsolidated material. In some areas, Brush Basin is lithified, very fine-grained, and green with some red weathering (Figure 26C). In the northeastern region of the field area, Saltwash exists as a white to tan coarse-grained sandstone, with conglomerate lenses. In some parts of the outcrops, there is black dendritic mineralization. In the southeastern region of the field area, the Saltwash includes of large portions of conglomerate, with poorly-sorted clasts ranging in size from 0.5 cm to 6 cm (Figure 26D, E). East of the large conglomerate outcrop is a cliff of typical Saltwash coarse-grained sandstone (Figure 26F).

Figure 26. Sedimentary rocks present in the field area. A: Slickenside in Dakota sandstone. B: Fossils in Dakota sandstone. C: Lithified Brushy Basin. D, E: Large clasts in Saltwash conglomerate. F: Cliff of typical coarse-grained Saltwash.

Crystal Size Distribution

CSD results (Appendix B) were used to quantify the textural differences between the upper and lower sheets that can be difficult to see in hand sample. The CSD curves for the sheets have different slopes, and the shapes of the curves differ considerably (Figure 27). The slopes of CSD curves for the lower sheet are generally steeper than those from the upper sheet (Table 1). The upper sheet contains larger plagioclase crystals, with sizes ranging from 0.5 mm to about 13.0 mm (Figure 28). The upper sheet CSD curves are mostly straight, but flatten significantly at higher crystal sizes. The lower sheet contains plagioclase crystals that range from about 0.5 mm to 8.0 mm (Figure 29). Most of the samples from the lower sheet have an upper crystal size threshold of 5.0 mm. Each of the CSD curves for the lower sheet have a generally consistent slope. The sample not from CRL shows a slope similar to that of the upper sheet samples that have the lowest crystal size upper threshold.

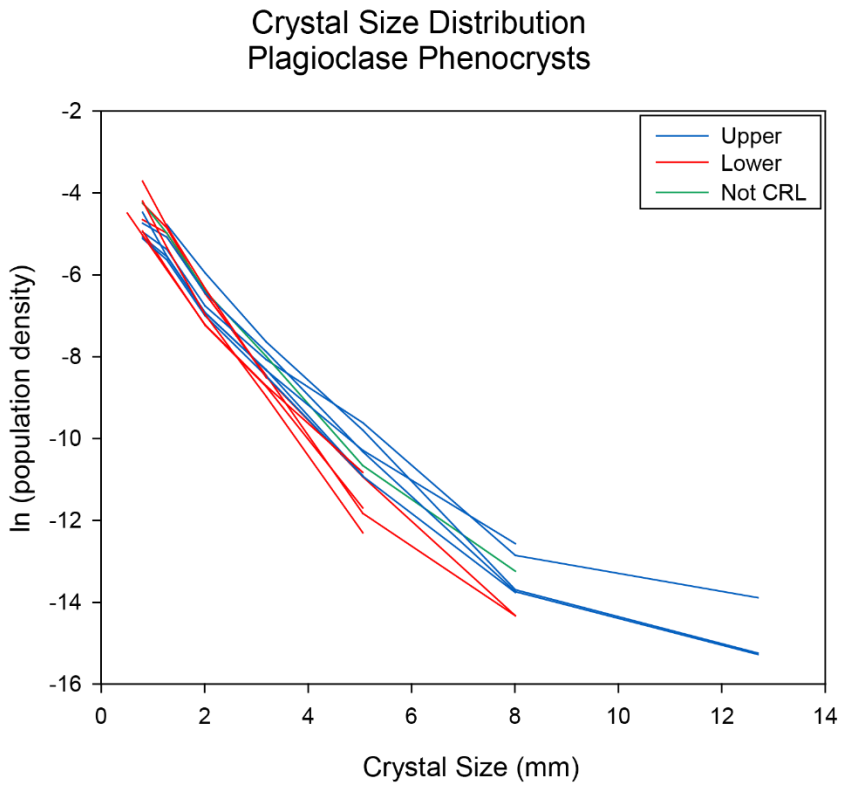

Figure 27. Crystal size distributions for the upper sheet, lower sheet, and a sample from an adjacent intrusion.

Upper Sheet			Lower Sheet			Not CRL		
Sample	Y-Intercept	Slope	Sample	Y-Intercept	Slope	Sample	Y-Intercept	Slope
CR19	-5.0746	-0.7868	CR2	-3.4465	-1.4503	CR38	-3.6409	-1.2612
CR48	-4.6251	-0.9414	CR9a	-3.6436	-1.3755			
CR59	-3.9565	-1.3784	CR14	-2.2155	-1.9939			
CR84	-4.3635	-1.2147	CR62	-3.8435	-1.5581			
CR95	-4.3168	-1.0923	CR88	-4.0526	-1.3901			
ME9	-4.4400	-0.9445	ME7	-2.9301	-1.8741			

Table 1. Slope and y-intercept values calculated through linear regression analysis on CSD curves for all samples.

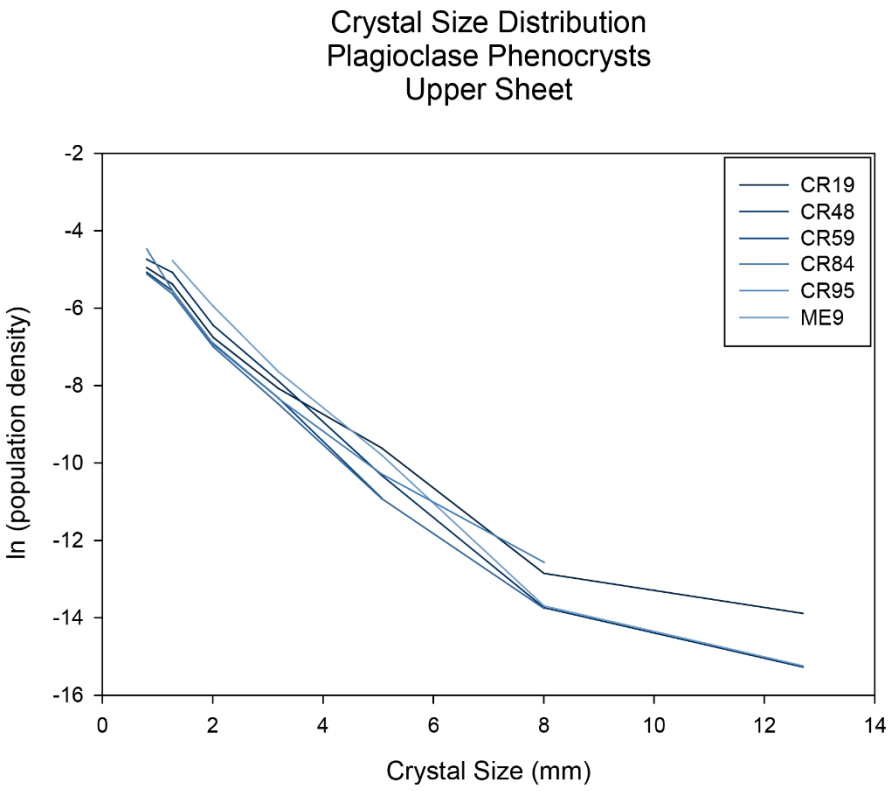

Figure 28. Crystal size distributions for the upper sheet.

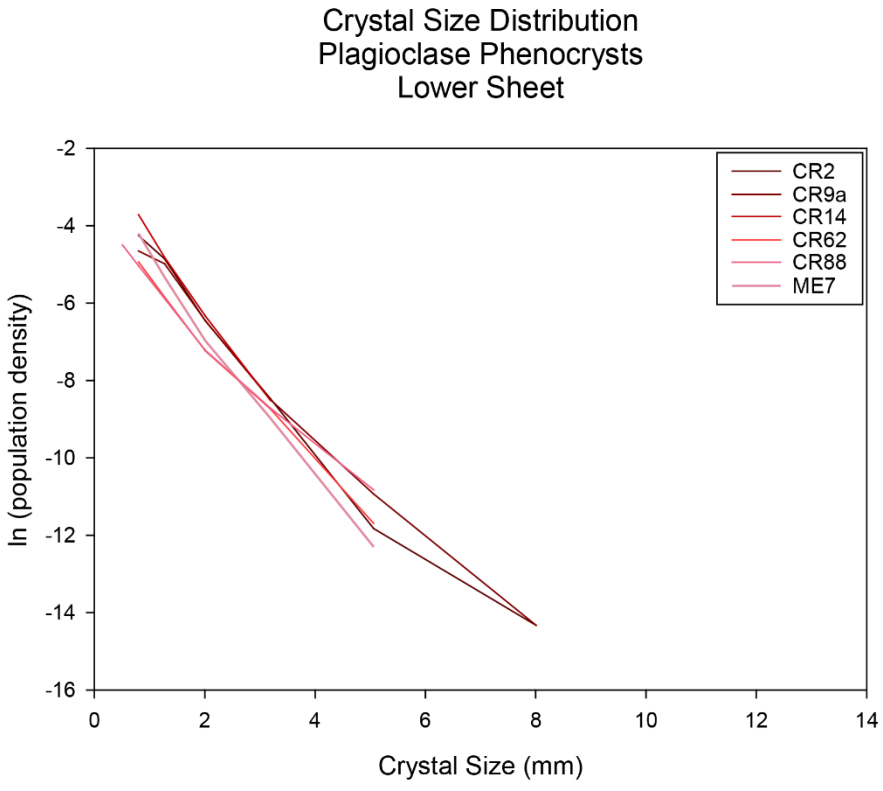

Figure 29. Crystal size distributions for the lower sheet.

Linear regression analysis gave a y-intercept and slope for each CSD curve. The y-intercept corresponds to the nucleation density in the magma, and the slope provides the characteristic crystal length for the sample. Plotting the characteristic crystal length versus the nucleation density reveals a trend between the upper and lower sheets (Figure 30). The upper sheet tends to have a higher characteristic crystal length and a lower nucleation density, and the lower sheet tends to have a lower characteristic crystal length and a higher nucleation density. Very little overlap exists between the upper and lower sheets. The two distinct groupings suggest that the two sheets underwent different crystallization histories. The sample that is not from CRL falls in between values from the upper and lower sheets. The overall relationship between nucleation density and characteristic crystal length shows that as the nucleation density gets higher, the characteristic crystal length decreases.

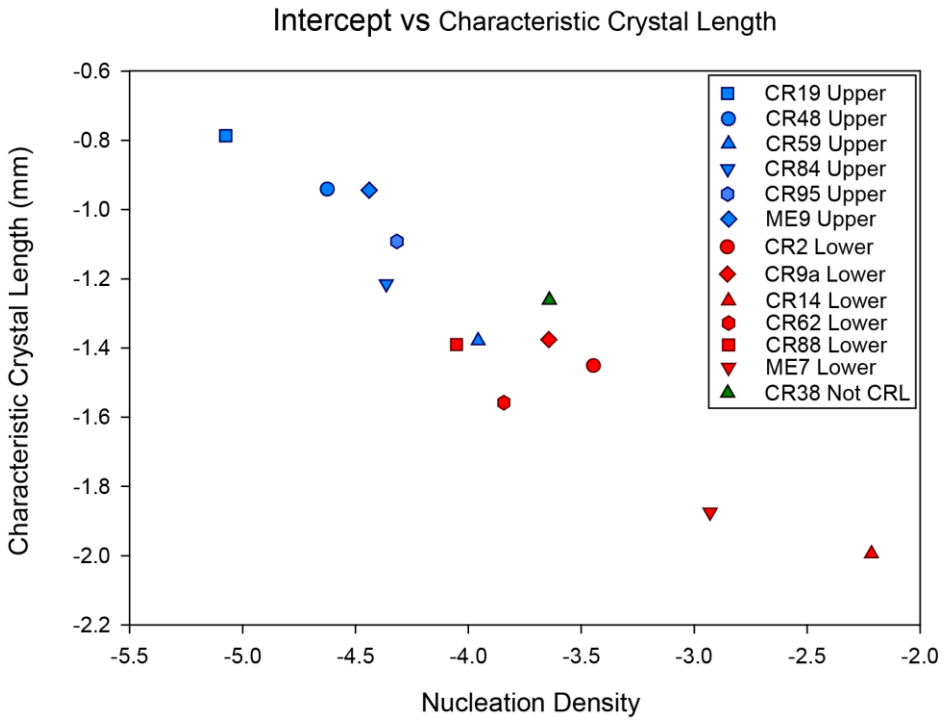

Figure 30. Characteristic crystal length vs. nucleation density for the CSD curves of all samples analyzed.

Geochemistry

Notable variations exist between the chemical composition of the upper and lower sheets (Appendix C). Silica concentrations vary between the sheets, but are consistent within each sheet. The upper sheet has lower silica concentrations, ranging from 58.12 wt% to 60.11 wt%, and the lower sheet has higher concentrations, ranging from 61.23 wt% to 63.2 wt%. Plotting data from the two sheets on a total alkalis (Na_2O+K_2O) versus silica (SiO_2) diagram (Le Bas et al., 1986) shows a difference in rock type (Figure 31). The upper sheet plots on the andesite/trachyandesite border and the lower sheet plots mostly as andesite, with one sample plotting in dacite and one sample in trachyandesite. There is no overlap in the silica concentrations, so the samples from the two sheets cluster separately. Samples from the northern end of the field area differ physically from the upper and lower sheets of CRL. Additionally these rocks vary chemically. Sample CR100 is a basaltic trachyandesite. Sample CR37 is a basaltic andesite and has the lowest silica and alkali concentrations of any sample analyzed.

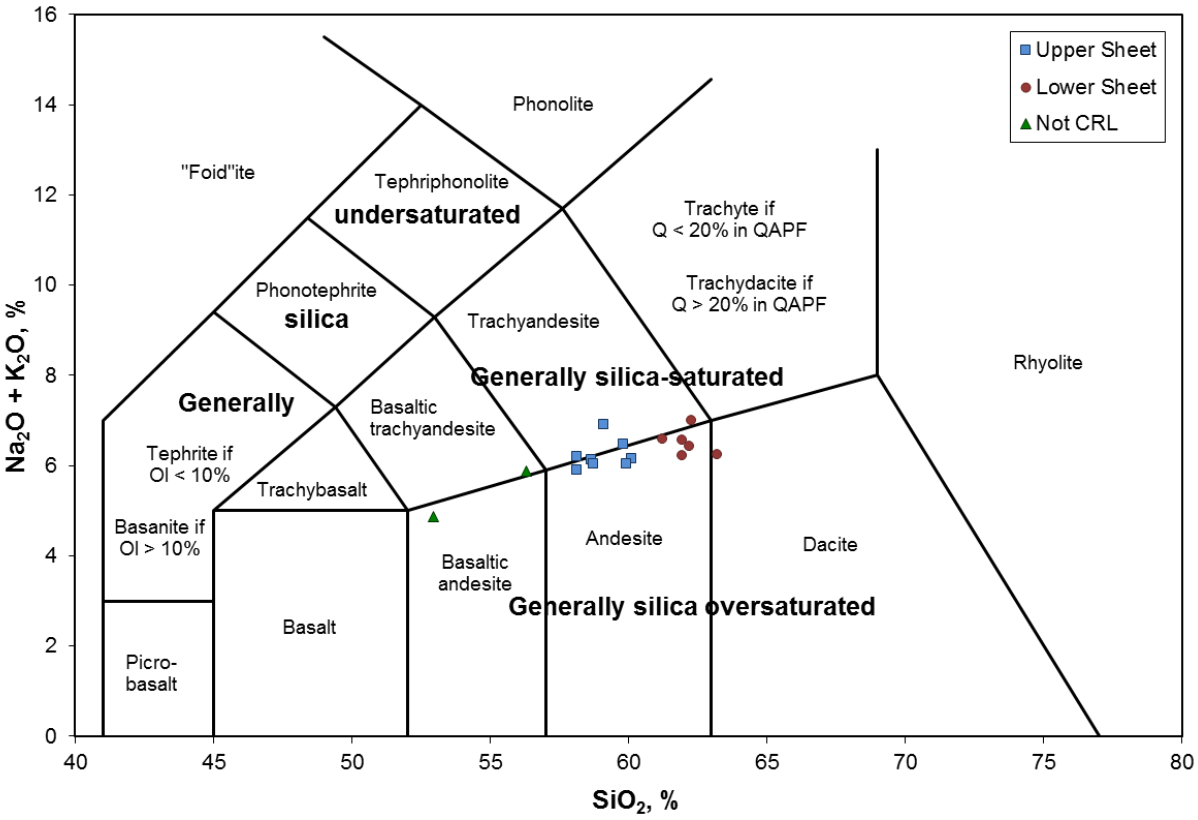

Figure 31. Total alkalis (Na_2O+K_2O) vs. silica (SiO_2) diagram (Le Bas et al., 1986) for 16 samples: 8 from the upper sheet of CRL; 6 from the lower sheet of CRL; and 2 from intrusions surrounding CRL.

Four major element oxides and 22 trace elements show statistically significant differences between the upper and lower sheets. The upper sheet has a higher average concentration than the lower sheet in all but two of the statistically significant elements. The lower sheet only has higher concentration than the upper sheet in SiO_2 and Ba. Mapping Fe_2O_3 (as total iron) concentrations show the general trend present for most of the statistically significant elements (Figure 32). Major and trace element concentrations plotted against silica concentration show the relationships between the upper sheet, lower sheet, and samples not from CRL (Figure 33).

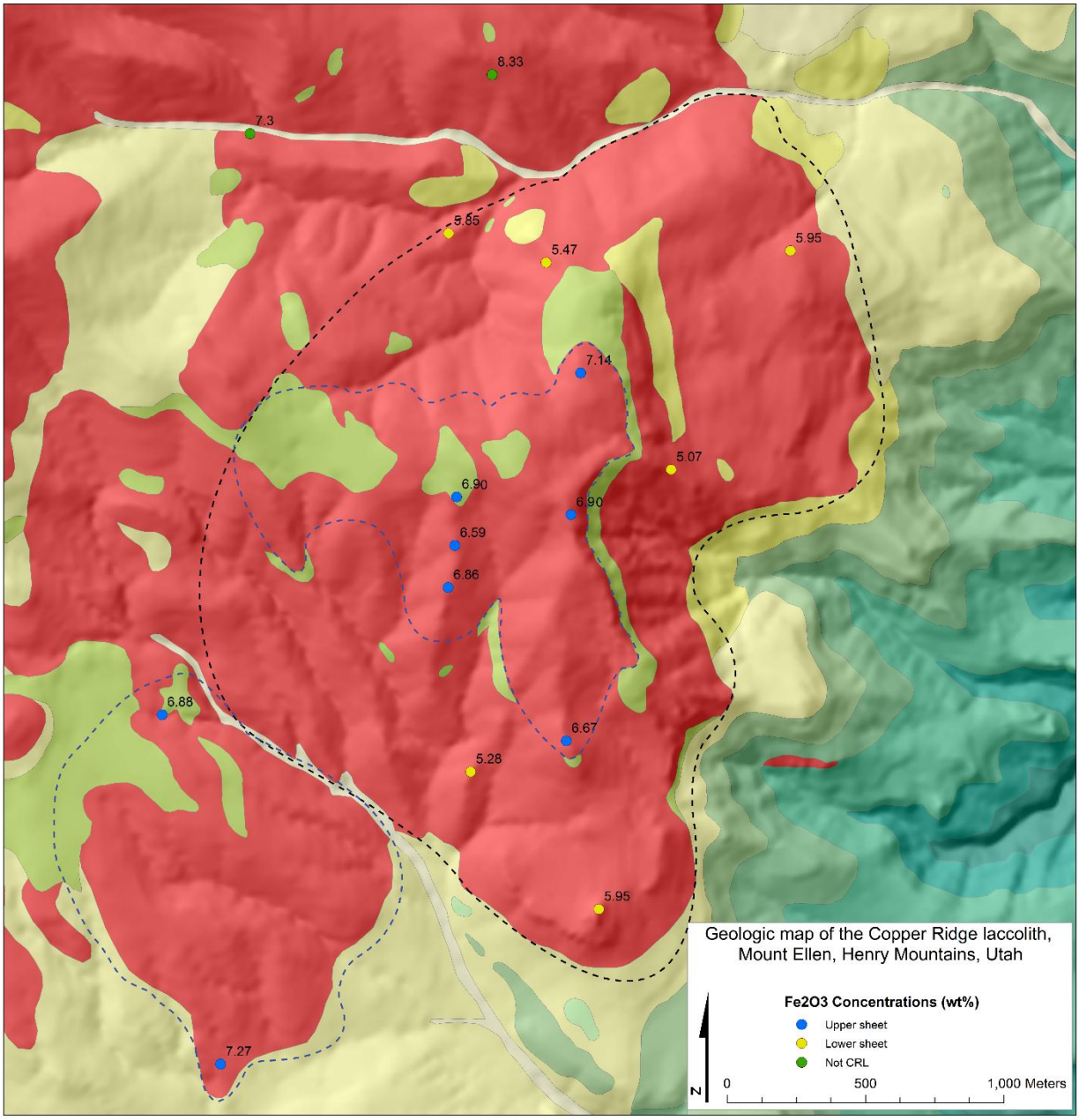

Figure 32. Map showing the abundance of Fe_2O_3 (Total wt.%) for the upper sheet, lower sheet, and an adjacent intrusion. A dashed blue line outlines the upper sheet, and a black dashed line outlines the lower sheet.

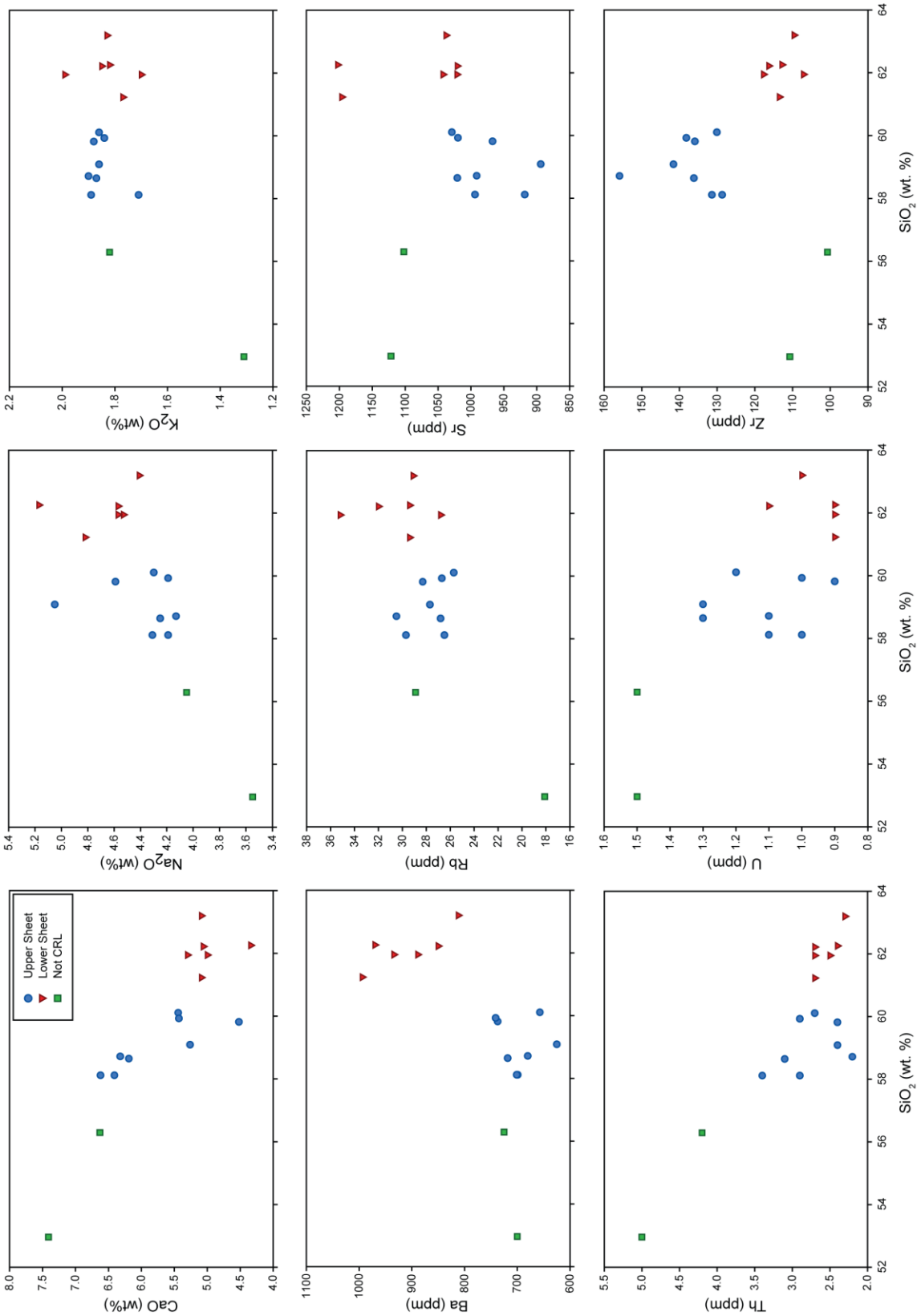

Figure 33. Harker diagram showing major and trace element concentrations vs. SiO_2 for the upper sheet, lower sheet, and samples from another intrusion. Elements plotted vs. silica include: CaO, Na_2O, K_2O, Ba, Rb, Sr, Th, U, and Zr.

Rare earth element (REE) concentrations were normalized to CI-Chondrite values (McDonough and Sun, 1995). Aside from lanthanum (La) and neodymium (Nd), the upper and lower sheets differ significantly in the REEs (Figure 34). Samples from the upper sheet tend to follow a consistent trend, with low standard deviations (Figure 35A). Samples from the lower sheet also follow a consistent trend, also having low standard deviations (Figure 35B). Samples from the adjacent intrusion have similar concentrations, with only small variations (Figure 35C). Average concentrations of each sheet from CRL show that the upper sheet is enriched in every REE relative to the lower sheet (Figure 35D). Samples from adjacent intrusions are enriched in about half of the REEs relative to the upper sheet, and all the REEs relative to the lower sheet (Figure 35D). Both the upper and lower sheet have low concentrations of heavy REEs. Additionally, there is no Eu anomaly in the upper and lower sheets REE patterns.

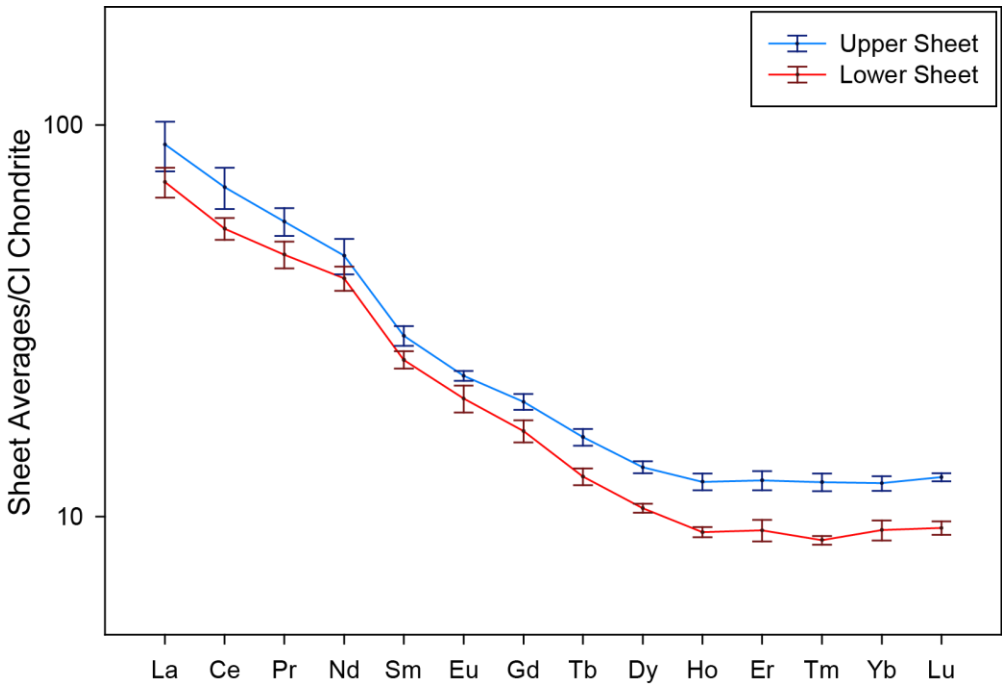

Figure 34. Chondrite-normalized (McDonough and Sun, 1995) REE plots for the upper and lower sheets. Error bars for each element represent one standard deviation in each direction.

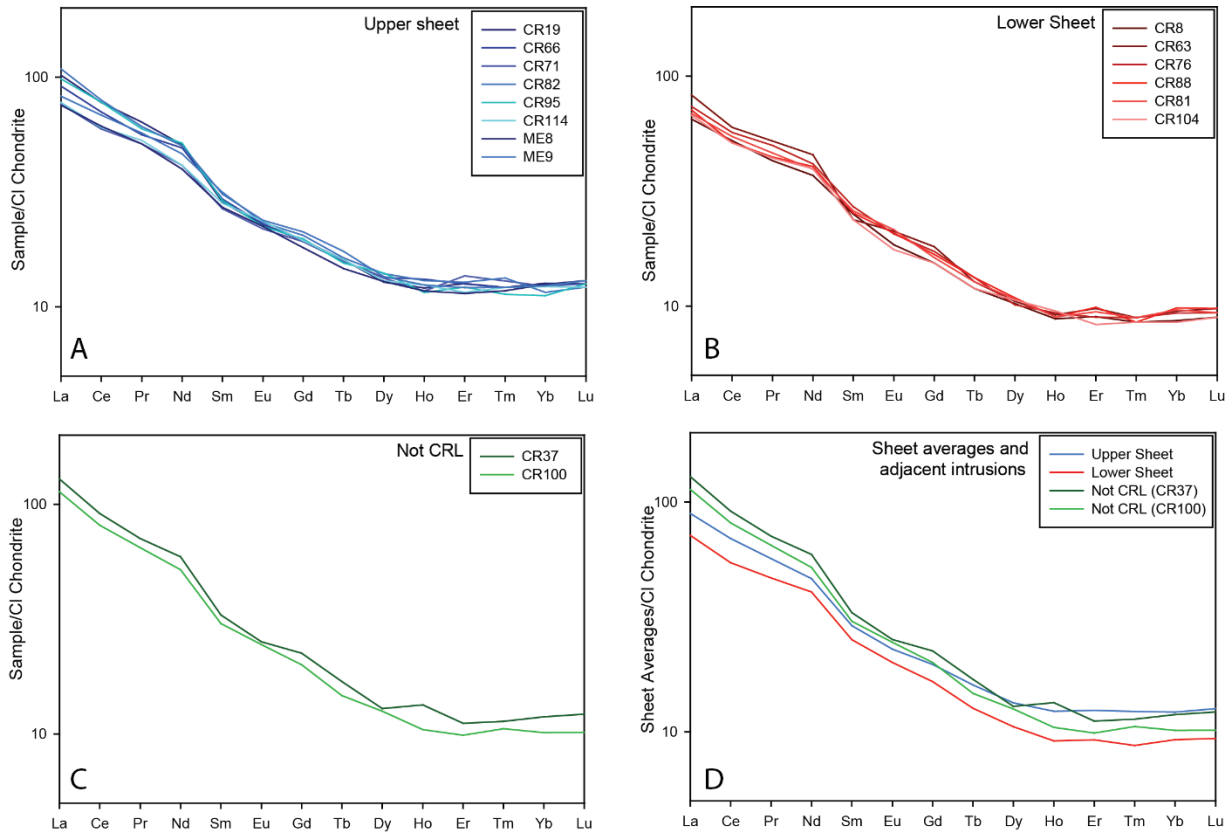

Figure 35. Chondrite-normalized (McDonough and Sun, 1995) REE plots for the A: upper sheet; B: lower sheet; C: intrusions adjacent to CRL; and D: all three combined to show differences and trends.

Anisotropy of Magnetic Susceptibility

K_1 orientations (lineations) are plotted on Figure 36. Additionally, individual stereonets for each location were plotted on a grayscale geologic map (Figure 37). For each site the stereonets show the K_1, K_2, and K_3 orientations, and the confidence ellipse for each axis. A loose trend in AMS lineations shows a generally consistent orientation down the main ridge of CRL, with lineations fanning out radially towards the margins of the intrusion.

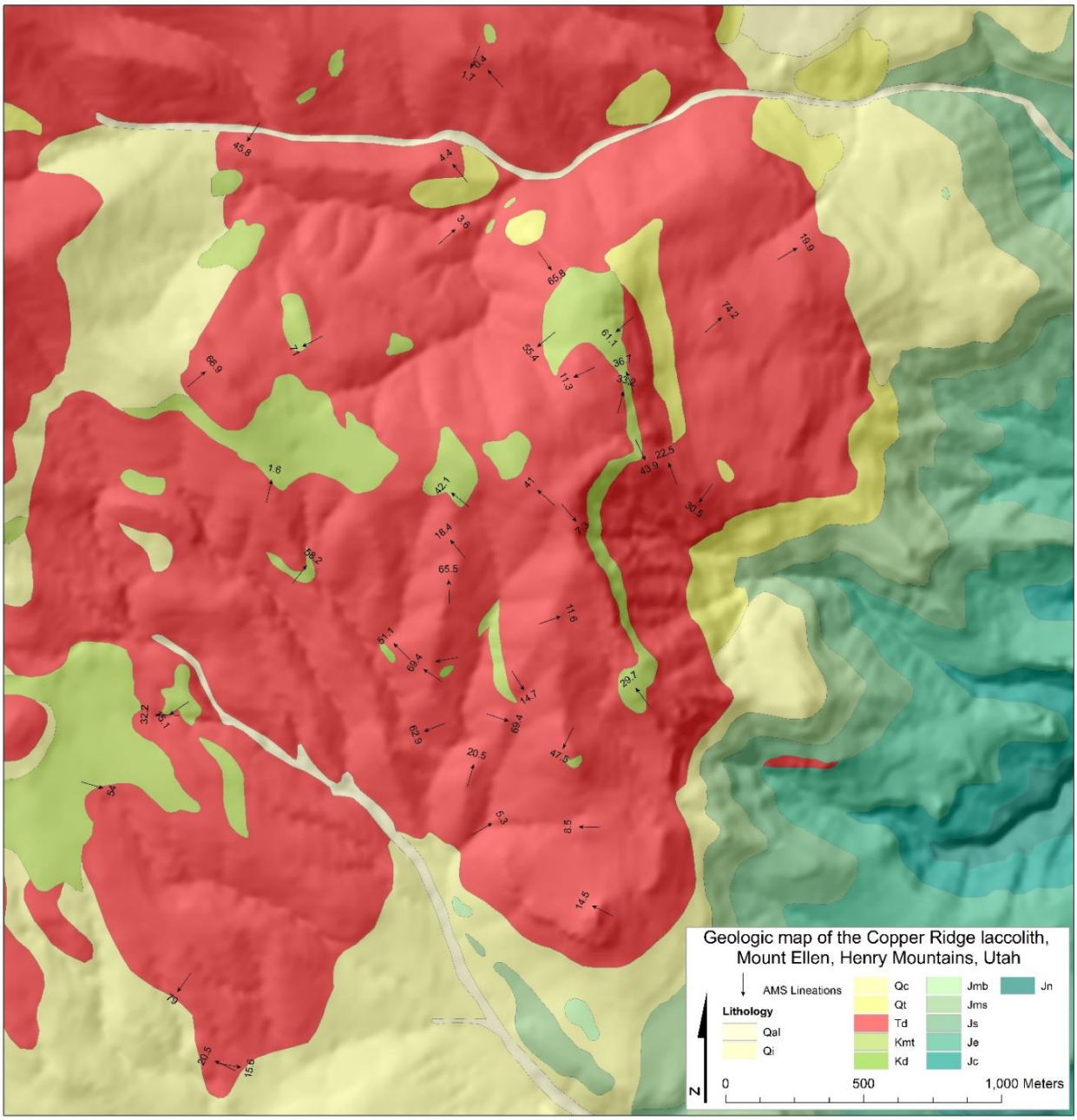

Figure 36. Geologic map of CRL with AMS lineations plotted.

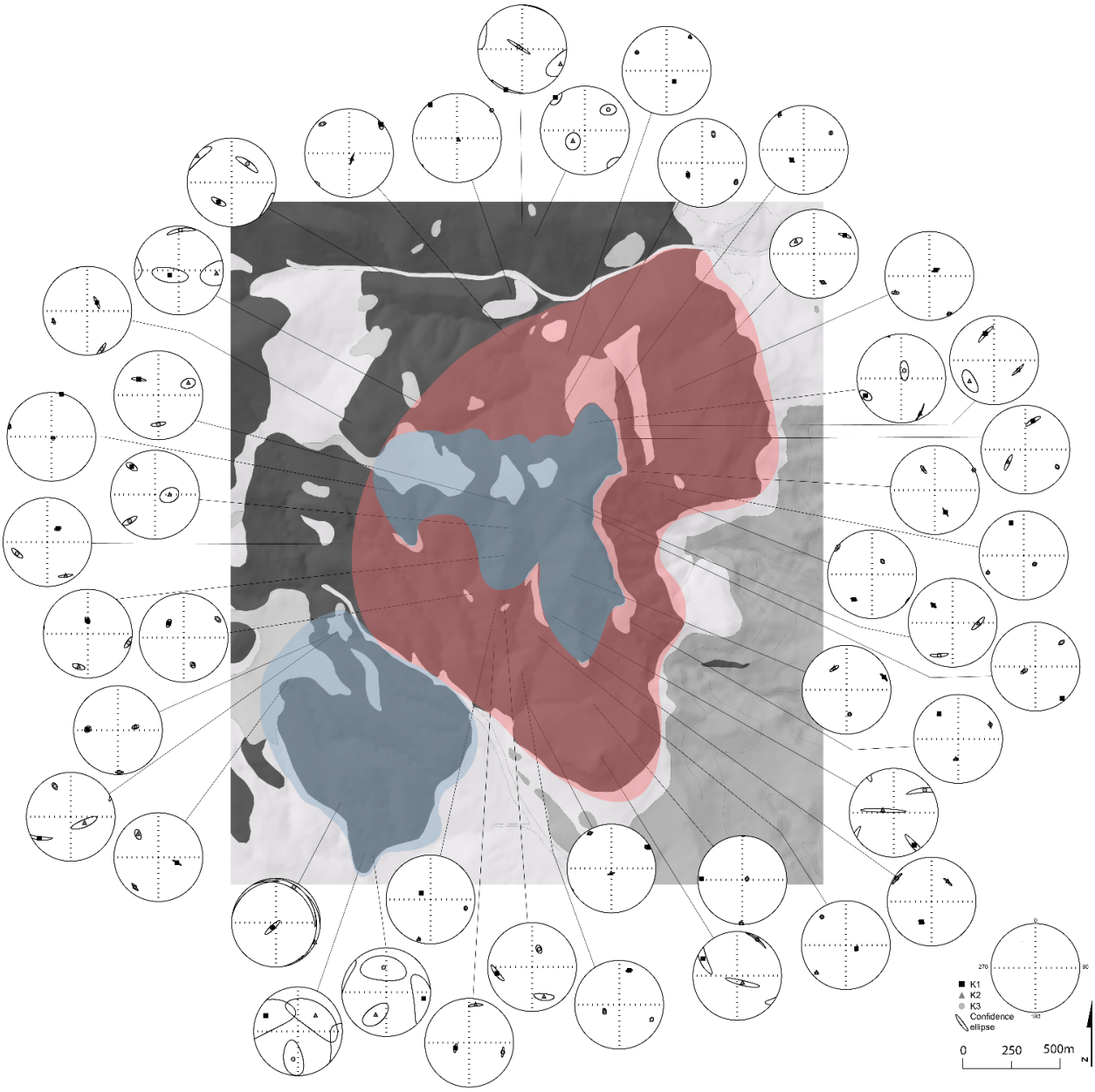

Figure 37. Grayscale geologic map of CRL with stereonets plotted for each sample site. Confidence ellipses are shown for each principal axis. The upper and lower sheets are outlined in blue and red, respectively. Stereonets that correspond to locations not within the red or blue areas are interpreted as being from intrusions separate from CRL.

AMS data from the upper sheet are plotted on equal area lower hemisphere stereographic projections (Figure 38A). The upper sheet K_1 orientations trend mostly from north-northeast to west-southwest and vary from shallowly plunging to steeply plunging (Figure 38B). K_3

orientations vary widely across all samples, with shallow and steep plunges trending in variable orientations. When samples are divided into the categories “not near contact” and “near contact” trends are observable. Samples are considered near the contact if they are no more than 10 m away from an observable contact. Upper sheet K_1 orientations near contacts are generally moderately to steeply plunging, and trend to the northwest (Figure 39A). K_1 orientations away from the contact are concentrated at shallow plunges, trending northwest and southeast (Figure 39B).

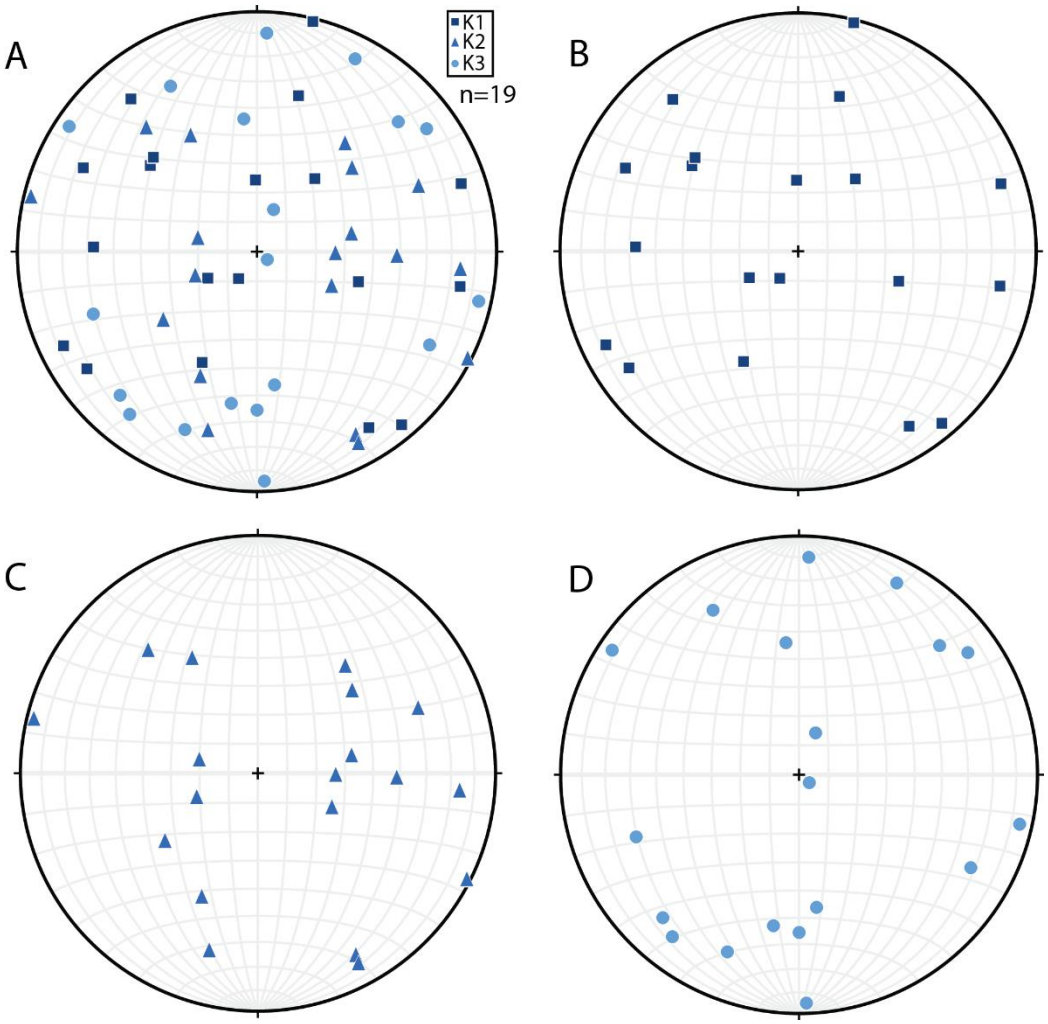

Figure 38. Equal area lower hemisphere stereographic projections for the upper sheet. Stereonets show: A: All upper sheet data; B: Upper sheet K_1 orientations; C: Upper sheet K_2 orientations; D: Upper sheet K_3 orientations.

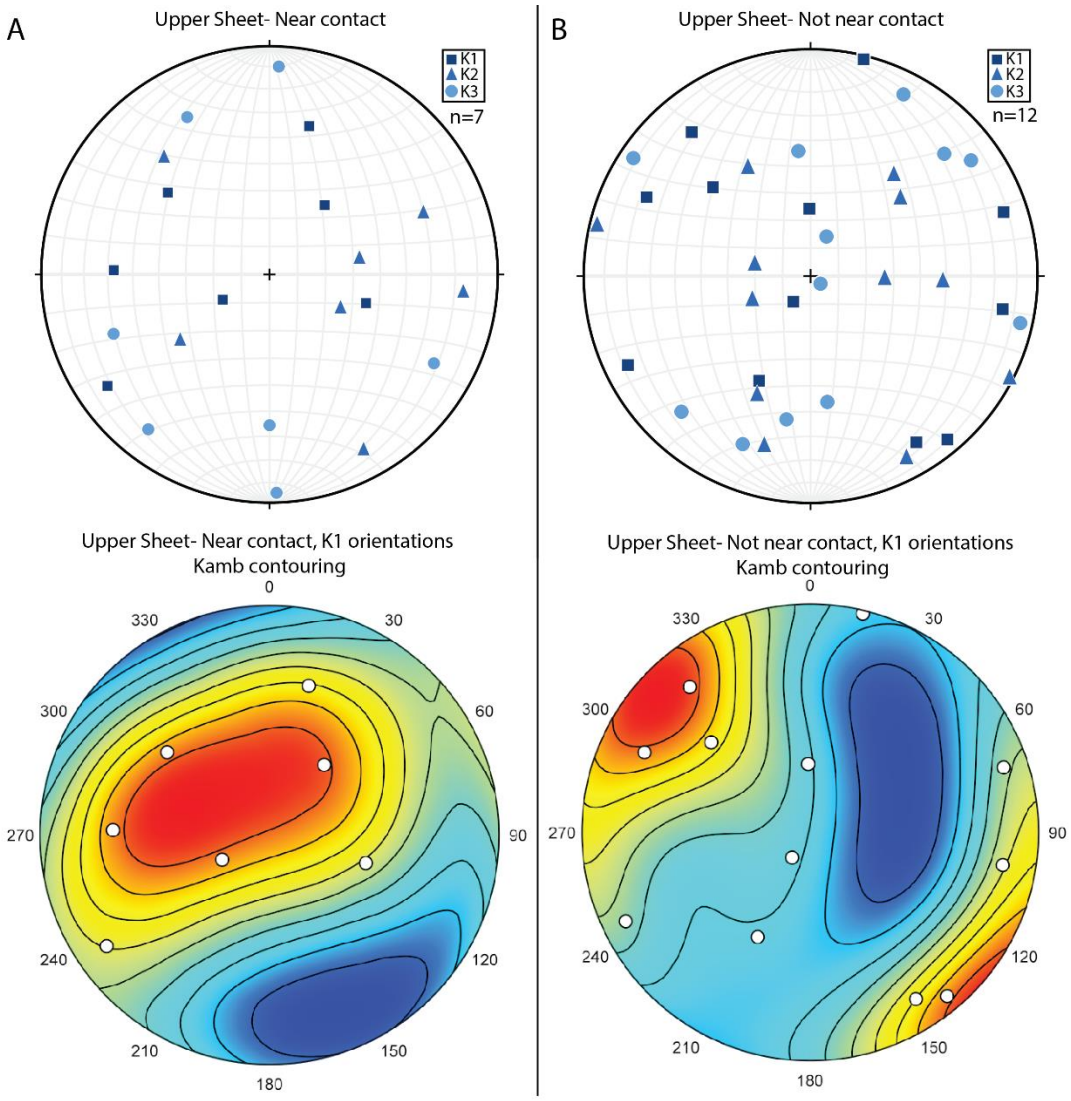

Figure 39. Equal area lower hemisphere stereographic projections for upper sheet samples, separated based on proximity to the margins of the intrusion. A: AMS orientations for upper sheet samples near contacts. K_1 orientations are shown with kamb contours. B: AMS orientations for upper sheet samples not near contacts. K_1 orientations are shown with kamb contours.

AMS data from the lower sheet are plotted on equal area lower hemisphere stereographic projections (Figure 40). The K_1 orientations for samples from the lower sheet cluster into shallowly to moderately plunging samples and steeply plunging samples (Figure 40B). The shallowly to moderately plunging samples trend in a swath from northeast to southwest. The steeply plunging K_1 orientations trend in various directions. K_3 orientations trend from northwest to southeast and have shallow and steep plunges (Figure 40D). Separating the lower sheet

samples into “near contact” and “not near contact” reveals trends in the data. Lower sheet samples near contacts have K_1 orientations that are moderately to steeply plunging and trend towards the southwest to northwest (Figure 41A). K_1 orientations for lower sheet samples not near contacts are concentrated along a main girdle, oriented from northeast to southwest (Figure 41B).

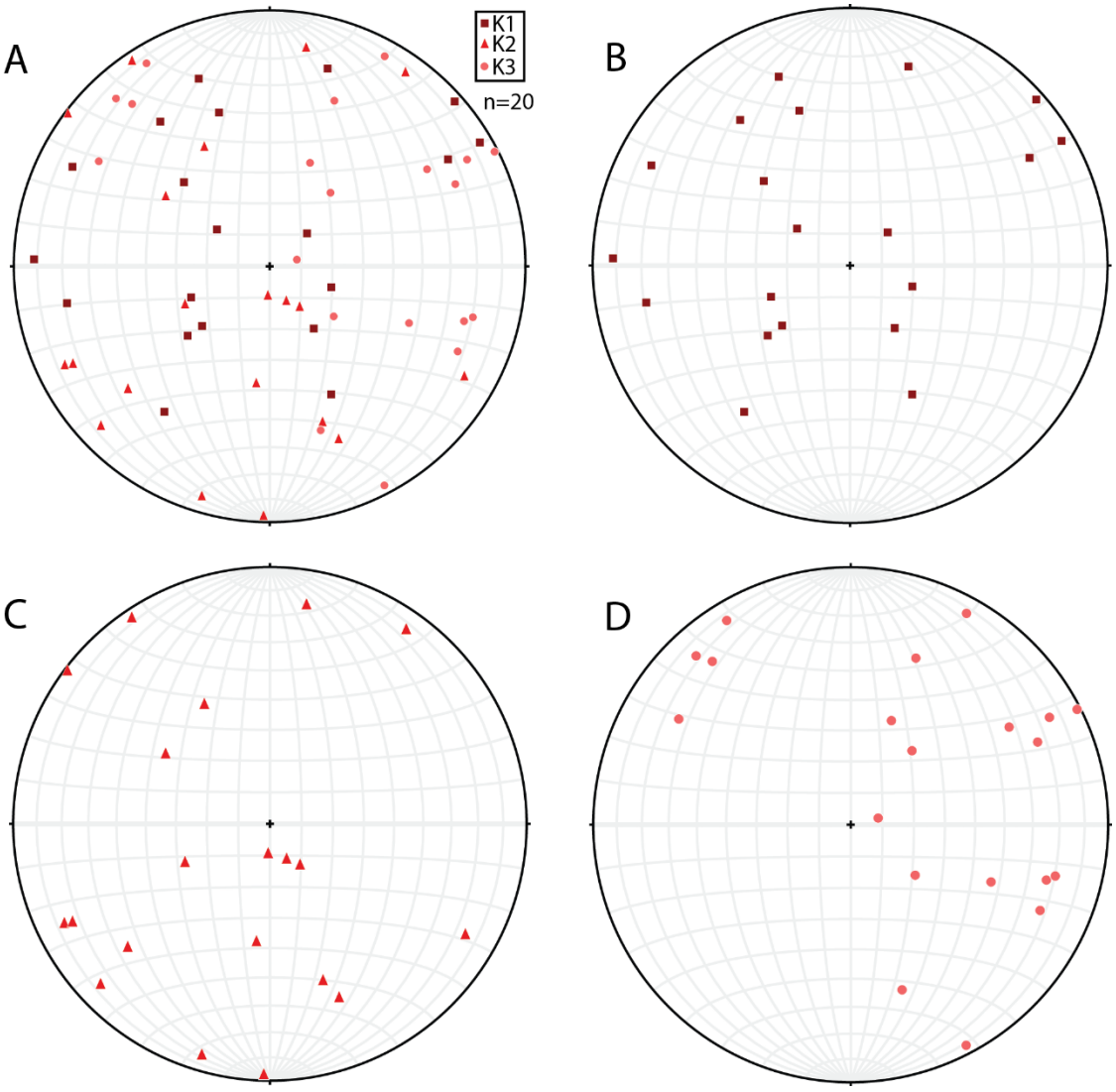

Figure 40. Equal area lower hemisphere stereographic projections for the lower sheet. Stereonets show: A: All lower sheet data; B: Lower sheet K_1 orientations; C: Lower sheet K_2 orientations; D: Lower sheet K_3 orientations.

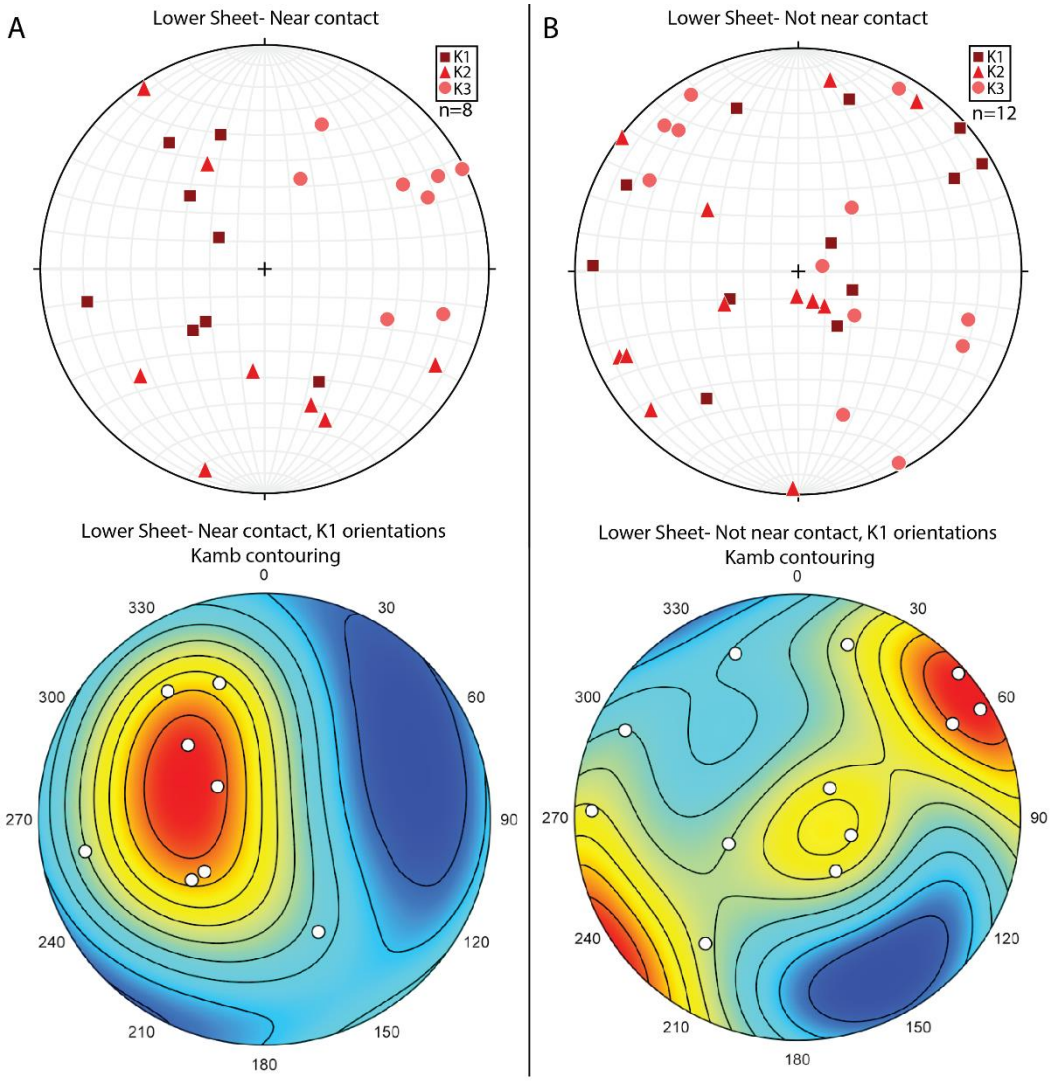

Figure 41. Equal area lower hemisphere stereographic projections for lower sheet samples, separated based on proximity to the margins of the intrusion. A: AMS orientations for lower sheet samples near contacts. K_1 orientations are shown with Kamb contours. B: AMS orientations for lower sheet samples not near contacts. K_1 orientations are shown with Kamb contours.

AMS scalar parameters are plotted in Figure 42. There are no apparent trends between the upper sheet, lower sheet, and adjacent intrusions for bulk susceptibility (K_m) values vs. other parameters. The upper sheet has a wider range of bulk susceptibilities, ranging from 2.72 $x10^{-4}$ SI to 7.53 x 10^{-2} SI, with an average of 1.98 x 10^{-2} SI and a standard deviation of 1.99 x 10^{-2} SI. Samples from the upper sheet have the highest susceptibilities. The lower sheet has a smaller

range of susceptibilities, ranging from 1.52 x 10^{-4} SI to 3.72 x 10^{-2} SI, with an average of 1.43 x 10^{-2} SI and a standard deviation of 9.91 x 10^{-3} SI.

Values for the ellipticity (*T*) for the upper sheet fall over a wide range, from -0.818 to 0.656, averaging at -0.061 with a standard deviation of 0.286. About half of the samples from the upper sheet fall in the oblate range (*T*= 0 to 1), and the other half in the prolate range (*T*= 0 to-1). Samples from the lower sheet have a smaller range in ellipticity, from -0.363 to 0.620, averaging 0.097 with a standard deviation of 0.326. Most of the samples from the lower sheet plot in the oblate range. No trend exists between *T* and K_m values (Figure 42A).

The degree of anisotropy (P_j) in the upper sheet ranges from 1.016 to 1.050, with an average of 1.023 and a standard deviation of 0.286. P_j values for the lower sheet range from 1.013 to 1.046, with an average of 1.031 and a standard deviation of 0.010. No apparent trends exist between P_j and the other parameters (Figure 42B, C).

The upper sheet, aside from one outlier, has a smaller range of lineation (*L*) values than the lower sheet. Upper sheet L values range from 1.003 to 1.041 with an average of 1.012 and a standard deviation of 0.003. Lower sheet L values range from 1.005 to 1.026, with an average of 1.014 and a standard deviation of 0.008. The upper sheet has a slightly larger range of foliation (*F*) values than the lower sheet (Figure 42D). Upper sheet F values range from 1.004 to 1.025, averaging at 1.011 with a standard deviation of 0.005. Lower sheet F values range from 1.007 to 1.025, averaging at 1.016 with a standard deviation of 0.006. The lower sheet *F* values follow a general trend, increasing with an increase in *L* values. The upper sheet data have no apparent trend.

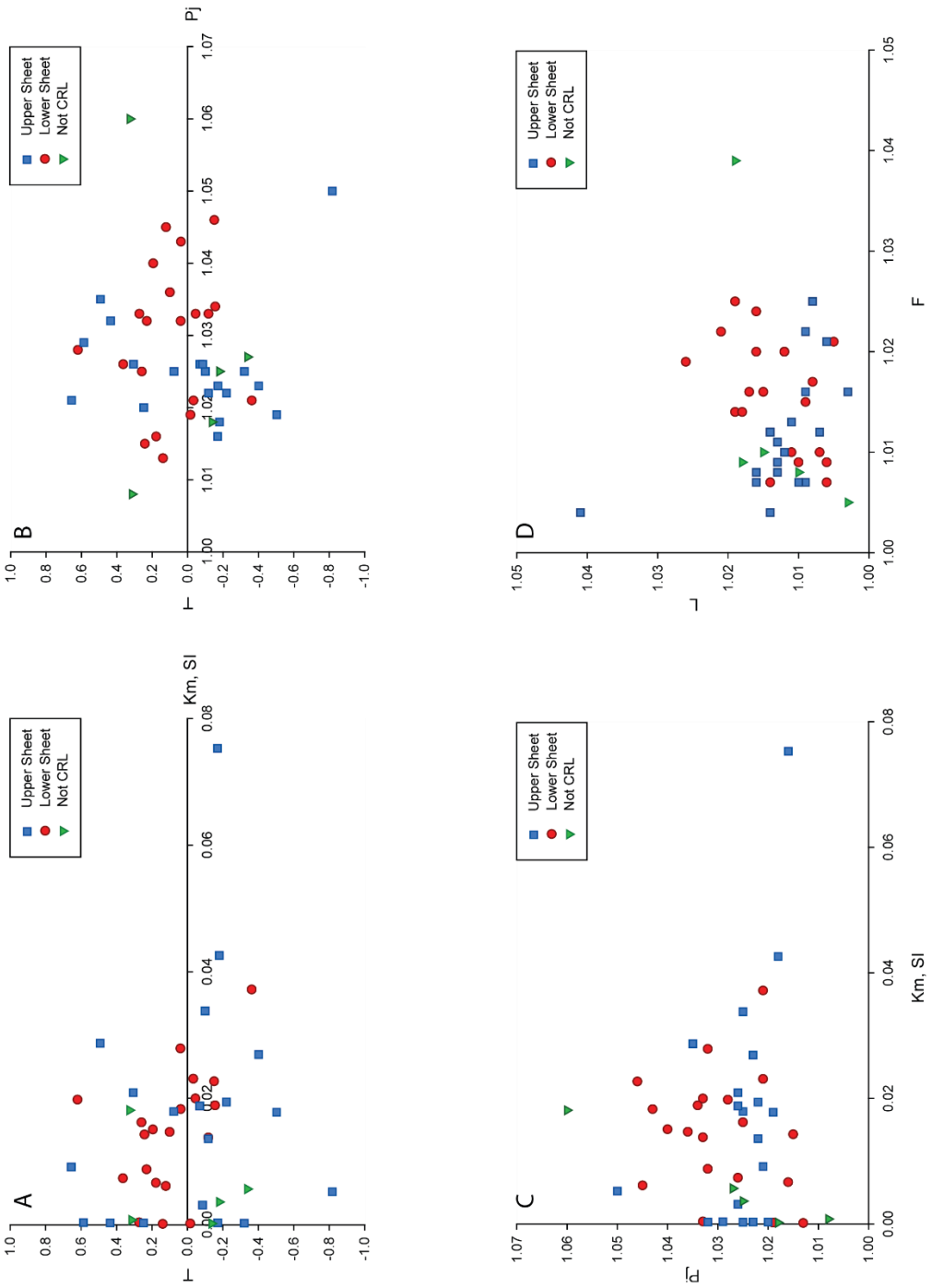

Figure 42. AMS scalar parameters plots for upper sheet, lower sheet, and adjacent intrusions. A: Ellipticity shape vs. bulk susceptibility. B: Ellipticity vs. degree of anisotropy. C: Degree of anisotropy vs. bulk susceptibility. D: Lineation vs. foliation.

X-Ray Diffraction

XRD performed on the three Tununk samples (Figure 43) revealed that the most prominent minerals are quartz, feldspar, and calcite. The samples were analyzed twice because the calcite peaks were extremely intense and obscured the smaller peaks of minor minerals. The

samples were treated with 10% acetic acid to get rid of the calcite, allowing the less intense peaks to be recognizable. On the first run, the data show that the upper sample contains quartz, calcite, and feldspar. The data suggest that the feldspars may be sodium or potassium feldspar. Data from the central sample shows that it contains quartz, calcite and sodium and potassium feldspar. The central sample data show strong peaks at 2θ= 7 and 14. Peaks at these locations are strong evidence for the presence of chlorite. The lower sample contains calcite, and sodium and potassium feldspar.

On the second run, the upper sample data show quartz, chlorite, and feldspar. There is strong evidence that it contains a potassium-rich feldspar. The middle sample data show quartz, chlorite, and feldspar. There is strong evidence that it contains potassium-rich feldspar as well as plagioclase feldspar. The lower sample data show chlorite and feldspar. There is strong evidence that the feldspar is plagioclase and orthoclase. Data also showed strong evidence that calcium-rich clinopyroxene is present in the lower sample.

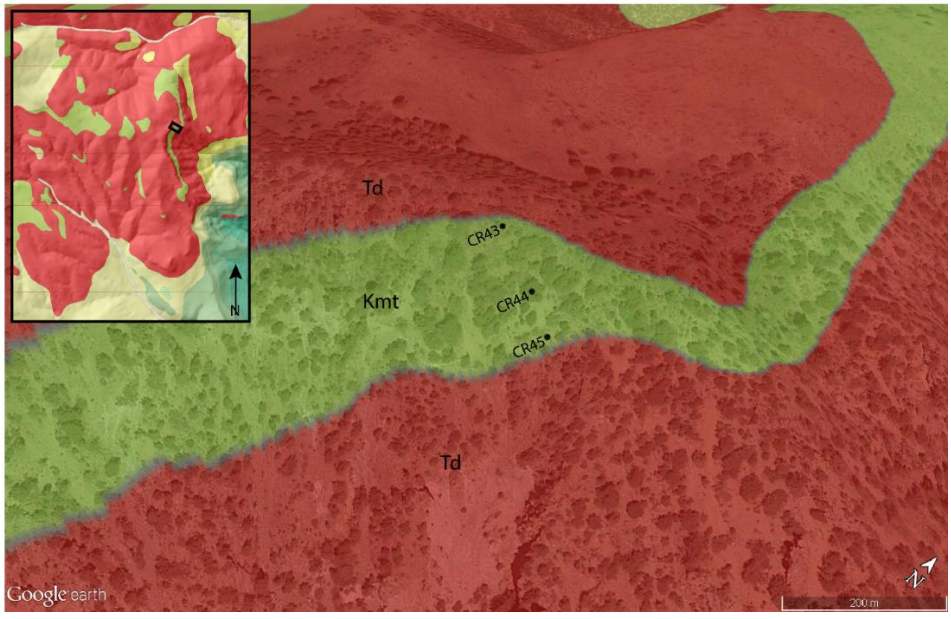

Figure 43. Map showing the location of the Tununk samples used for XRD analysis. Inset shows the location of the samples on CRL.

Discussion

Field Work

Physical characteristics of the igneous rocks observed in the field suggest that CRL formed through two separate pulses of magma, resulting in an upper and lower sheet. Field observations suggest that the nearly continuous, well-preserved Tununk layer within CRL separates the upper and lower sheets. The intrusion of the upper and lower sheets displaced the Tununk vertically, and the layer remained mostly intact, maintaining the original horizontal to subhorizontal bedding. The folding, calcite veins, and micro-faulting locally present in the Tununk indicate that the layer was deformed by the intrusions.

The upper sheet likely intruded into the central portion of the Tununk (originally ~134 m thick). Local preservation of cap rock on the main CRL ridge suggests there was a substantial thickness of Tununk above the upper sheet. The lower sheet likely intruded close to the contact between the Tununk and the underlying Dakota sandstone. The lower sheet would have had to intrude low enough for the thick portion of Tununk now between the sheets to be preserved. The lower contact between the Tununk and the lower sheet is locally preserved, and in many places there are lenses of Dakota within the lower sheet. Dakota was not observed in place in the field area, suggesting that it was locally disaggregated by the intrusion of the lower sheet.

Dakota inclusions found within the intrusion had highly variable bedding dips, and were definitely rotated and maybe displaced from their original locations. The lenses of Dakota are similar to intercalated sedimentary rocks in the Maiden Creek sill described by Horsman et al. (2005), and sedimentary rafts in a laccolith described by Schmiedel et al. (2014). Fault surfaces

observed in the Dakota lenses may be detachment surfaces where the lens detached from its original location, or perhaps a larger piece of Dakota split into smaller pieces through faulting.

Constraining the geometry of CRL and its component sheets required the classification of igneous rocks based on physical properties. The physical differences between the upper and lower sheet were consistent throughout most of the field area. However, the location of the igneous rocks found in the Garden Basin area raised questions as to whether or not they were part of CRL. These rocks are texturally similar to the upper sheet but are at the same elevation as the lower sheet, causing the upper sheet to appear segmented in map-view. Based on textural characteristics of the rocks, and a variety of other datasets, they are interpreted as being part of the upper sheet. The northern margin of CRL was remapped because the rocks from the ridge to the north of the main CRL ridge are texturally different from any observed in CRL. The ridge north of CRL is interpreted as being from a separate intrusion. To further support this, an area on the same ridge contains igneous rocks with large inclusions of several types of sedimentary rock. This zone may be an example of the complex process zone that forms at the tip of a propagating magma body. The orientation of the ridge and the location of the process zone suggest that the ridge to the north of CRL is a separate intrusion. These observations contradict the extent of CRL as mapped by Hunt et al. (1953) and support the new extent map (Figure 13). Hunt et al. (1953) originally suggested CRL had a length of 3 km and a width of 8 km. The new extent map suggests a length of 2 km and a width of 4 km.

Field observations and measurements were used to try to understand magma flow at the time of intrusion. Magma flow tends to align crystals in relation to flow directions, and the rapid cooling of the CRL igneous rocks in the shallow crust locked the aligned crystals in place. Crystal alignment is a useful indicator of magma flow directions, and variations in alignment can

result from different locations within the intrusion (Knight and Walker, 1988; Philpotts and Asher, 1994; Correa-Gomes et al., 2001). Magmatic fabric patterns measured in the field show a consistent orientation down the main ridge of CRL, with a fanning pattern toward the margins. This suggests that as the magma intruded it was fed toward the east-southeast through a main conduit. This conduit then fed more local magma flow radially towards the margins. The vergence of the detachment fold in the Tununk supports magma flow in those directions.

The overall geometry of both sheets in the intrusion suggests magma was fed laterally from the central portion of Mount Ellen to where CRL formed. The upper and lower sheets both fan out from the same general area, suggesting that the feeders for both sheets were located to the west-northwest, which agrees with field measurements. The magma was likely transported vertically from depth to the central portion of Mount Ellen, and horizontal feeder movement began when magma exploited the weaknesses in the Tununk, which is overlain by a sandstone. As described by Kavanagh et al. (2006) magma is likely to intrude into less competent layers when it reaches a boundary between an overlying competent layer and an underlying less competent layer.

Sedimentary strata in the vicinity of CRL are locally deflected upward from their consistent regional orientation, as shown in cross section (Figure 12). I interpret this to mean that a subsurface intrusion has locally lifted the sedimentary strata. In cross section A-A', I hypothesize that a buried intrusion, locally under CRL, is associated with the Ragged Mountain bysmalith to the south of CRL. The formation of the hypothesized intrusion likely postdates the formation of CRL, and the buried intrusion may have lifted the southern margin of the lower sheet. The extremely fractured area in the lower sheet (Figure 19) may be evidence for this post-

CRL emplacement deformation. The suggested intrusion in the D-D' cross section is likely independent of CRL, and during intrusion locally lifted the overlying sedimentary strata.

The observed reduction in phenocryst size and abundance near the contacts in the upper sheet is attributed to the Bagnold effect (Bagnold, 1954), which is described in igneous intrusions by Komar (1972 a, b). The velocity gradient in a magma near an intrusion margin creates a grain dispersive pressure. Close to the contacts, the velocity decreases and viscosity increases, and in order to maintain a constant grain dispersive pressure through the magma, crystals are preferentially moved to the center. The forces preferentially affect large crystals, resulting in a smaller mean crystal size towards the margins of the intrusion and a larger mean crystal size towards the center of the intrusion.

Crystal Size Distribution

The upper and lower sheets have distinct CSDs, indicating that they underwent different crystallization histories. Larger crystal sizes suggest a longer crystal growth period, relative to smaller crystal sizes. The upper sheet has larger plagioclase crystals than the lower sheet, suggesting that the upper sheet had a more extended period of crystal growth.

The upper sheet samples all have shallow and consistent slopes (Figure 28). Some of the samples have a segmented slope, with a consistent slope that shallows out significantly around the 8 mm crystal size extending to 13 mm. The consistent slope of the curve suggests steady-state cooling (Marsh, 1988). The shallowing of the slope at 8 mm suggests that the magma underwent textural coarsening at depth. Higgins (1998) suggests that at depth, plagioclase will begin to crystallize and at a certain depth and temperature nucleation stops and textural coarsening begins. During textural coarsening tiny crystals are reincorporated into the melt and

larger crystals continue to grow. As ascent continues, coarsening slows and stops, resulting in a CSD curve similar to those from the upper sheet.

The CSDs for lower sheet samples exhibit a relatively steep and consistent slope (Figure 29). With only minor changes in slope in some samples, the lower sheet likely went through a nearly steady state cooling cycle. If the magma was transported to the shallow crust after a shorter time at depth smaller crystals would result.

A consistent relationship exists between the nucleation density and the characteristic crystal length (Figure 30). Mock et al. (2003) had similar results, and suggested that higher nucleation densities lead to a large number of small crystals. The differences in nucleation density and characteristic crystal length between the upper and lower sheets of CRL suggest that the two sheets are from distinct pulses of magma. It is likely that the lower sheet ascended to the shallow crust after a shorter amount of time at depth than the upper sheet.

Geochemistry

The distinct clustering of geochemical data for the upper and lower sheets into two groups (Figure 31) suggests that the upper and lower sheets are from separate pulses of magma. Geochemistry results for CRL samples are broadly consistent with the findings of Nelson and Davidson (1993), who analyzed several samples from other intrusions on Mount Ellen. Trace element abundances from CRL samples are similar to other samples from Mount Ellen, with only minor variations in some elements. No samples from Nelson and Davidson (1993) were from CRL, so variations in the trace element abundances are to be expected. The broad similarities across the samples from Mount Ellen and CRL may suggest that the intrusions come from a common magma source.

Relative to the upper sheet, the lower sheet has higher silica and lower trace element concentrations. The REE plots for the upper and lower sheets show that the upper sheet is relatively higher in every REE (Figure 35). Nelson and Davidson (1993) attributed most of the differences in elemental abundance to fractional crystallization, which may be the cause of the differences between the two sheets. The magma that formed the lower sheet may have hosted more fractional crystallization than the magma that formed the upper sheet.

Nelson and Davidson (1993) also observed a lack of a Eu anomaly. The lack of a significant Eu anomaly may be the result of no addition or loss of plagioclase from the crystallizing magma body. The loss of plagioclase during crystallization processes leads to a negative Eu anomaly, and the addition of plagioclase to a melt leads to a positive Eu anomaly (Rollinson, 2013).

Anisotropy of Magnetic Susceptibility

AMS data can provide information about magma flow at the time of intrusion (Horsman et al., 2005; Morgan et al., 2008). Lineations towards the center of the upper sheet trend in approximately the same orientation down the main ridge of CRL, and are interpreted to mark the main flow channel of the magma. This orientation may indicate that magma flowed toward the east-southeast from a feeder in the west-northwest. A second trend in upper sheet lineations is a pattern fanning outward from the main flow channel. The fanning lineations suggest that the magma flowed from the center of the sheet outward to the margins. For the most part, these lineations are close to perpendicular with the margins of the intrusion. The perpendicular relationship may be consistent with magma flow paths that fanned outward towards the contacts during intrusion. Morgan et al. (2008) observed similar trends on Trachyte Mesa, and arrived at similar conclusions. The center of the lower sheet of CRL is not observable, but AMS data

collected from lower sheet samples reveal a fanning pattern similar to that in the upper sheet. I interpret this to mean that the feeder for the lower sheet was located in the same general area as the feeder for the upper sheet.

In both the upper and lower sheets, samples collected away from contacts yielded AMS lineations with variable trends, dominated by subhorizontal plunges. The subhorizontal plunges are likely the result of flattening that occurred while magma spread and the overburden was lifted (e.g. Horsman et al., 2005; Morgan et al., 2008). In both the upper and lower sheets, samples collected near contacts had lineations with moderate to steep plunges. This was likely caused by drag against the host rock rotating crystals.

In almost all instances, for both the upper and lower sheets, the degree of anisotropy (P_j) is highest near the margins. There is a semi-consistent trend with P_j values increasing from the center of the sheets outward, suggesting that fabric is better developed near the margins. Better-developed fabric near the margin of intrusions is likely the result of viscous drag against the host rock (Horsman et al., 2005).

X-Ray Diffraction

Overall, the three Tununk samples from between the upper and lower sheets have consistent mineralogy. The only difference is that the sample close to the lower sheet lacked quartz and contained some clinopyroxene. The rocks have not been metamorphosed to hornfels facies likely due to the rapid cooling of the intrusions. In shallow igneous intrusions, the temperature of the magma decreases rapidly. According to Kornprobst (2002), a shallow crustal intrusion can only metamorphose the host rock at low temperatures (≤400°C), even directly

adjacent to the contact. The short duration and low temperature of the heating is likely the reason that the Tununk was not metamorphosed to a hornfels.

Relative to other minerals, pyroxenes require higher temperatures to form in hornfels (Kornprobst, 2002), so the presence of clinopyroxene in the lower sample may indicate that the lower sheet heated the Tununk to a higher temperature than the upper sheet. The elemental differences coincide with physical differences in the Tununk samples. The lower portion Tununk appears to be more highly metamorphosed than the upper sheet, with a more mottled surface, and more fractures and veins of calcite. The lower sheet consists of a much larger volume of magma and may have heated the Tununk for longer than the upper sheet did, resulting in differences in metamorphism within the Tununk.

Construction History and Geometry of the Copper Ridge Laccolith

The data collected for this study are consistent with two distinct construction histories for CRL. The first is a model in which the upper sheet intruded prior to the lower sheet. The second is a model in which the lower sheet intruded prior to the upper sheet. Regardless of the timing, the proposed flow paths inside the sheets remain the same (Figure 44 and Figure 45). The flow path interpretations are modeled after the work of Morgan et al. (2008) on the Trachyte Mesa laccolith. Flow path interpretations are based on both AMS lineations and magmatic fabric field measurements; arrow width is proportional to the importance of the flow path. Data from the central portion of the lower sheet were sparse in the field, so interpretations in this area are hypothetical.

Also regardless of the timing, the final geometry of the intrusion is an asymmetric, fan shaped laccolith. The upper and lower sheets both originated from some feeder in the west-

northwest. Both sheets have relatively flat bottoms and domed tops, creating a planoconvex cross-sectional geometry. Portions of the upper sheet exist at similar elevations as the lower sheet.

Preferred Construction Model: Upper Sheet before the Lower Sheet

The preferred construction model is shown schematically in Figure 46. Magma likely ascended rapidly from depth in a vertical feeder to the central portion of Mount Ellen, where it exploited the weak bedding planes of the Tununk layer. Movement through a now horizontal feeder led magma to the area that would become CRL. The upper sheet formed when magma moved through a main flow channel and spread radially while lifting the overburden (Figure 44). Once the magma reached its lateral extent, vertical growth dominated. The upper sheet inflated and vertically displaced the overlying sedimentary strata.

The second pulse of magma likely originated from a similar mid-crustal storage area and ascended along the same general path. The magma forming the lower sheet spread through a main flow path and then fanned out radially (Figure 45). The lower sheet intruded off center under the upper sheet, with its southern extent ending just south of the center of the upper sheet, and its northern extent extending well past the northern margin of the upper sheet. As it spread, the magma lifted the strata and upper sheet to make space for itself, and much of the Dakota sandstone was disaggregated. Once the magma reached its final lateral extent, vertical growth dominated, displacing both the overlying Tununk and the upper sheet. The off center intrusion of the lower sheet caused the overburden to form a monocline. The upper sheet monocline resulted in a central limb separating a portion of the upper sheet resting on top of the lower sheet, and a portion of the upper sheet that has no lower sheet below it. As vertical growth progressed, fractures and faults likely formed in the central limb of the upper sheet monocline. The off center

intrusion of the lower sheet also led to variations in the thickness of the lower sheet. In the north, the lower sheet is thicker. This is likely the result of there being no upper sheet overlying the northern portion of the lower sheet.

After CRL was exposed at the surface of the earth, the faults and other fractures in the upper sheet likely facilitated higher weathering and erosion rates. As a result, the central limb zone was deeply eroded away, exposing the lower sheet and making the upper sheet appear segmented (Figure 13).

This growth model is preferred because under-accretion is commonly observed in intrusions formed through pulsed construction (Menand, 2011). Additionally, most of the upper sheet remains intact, except for the hinge region. The lower sheet intruding second and fracturing the hinge region would account for the hinge eroding away, while the rest of the upper sheet remained intact. In the alternative model, fracturing would not have been concentrated and the hinge region would likely be present in modern outcrops.

Alternative Construction Model: Lower Sheet before Upper Sheet

As an alternative model, the lower sheet may have intruded before the upper sheet. Magma would have originated and flowed in the same way as the preferred construction model (Figure 45). As the lower sheet magma spread to form CRL, it lifted the overburden and deformed the host rock, disaggregating much of the Dakota sandstone in the process.

In this model, the upper sheet intruded some time after the lower sheet. As the upper sheet intruded, magma spread both north and south. The northern margin is much more constrained than the southern margin. One possible reason for the asymmetry of the upper sheet is that there was some preexisting weakness in the Tununk toward the south, and the magma

exploited it, allowing the magma to spread farther to the south. The southern portion of the upper sheet may have flowed through the Tununk and cascaded down over the southern margin of the lower sheet (Figure 44).

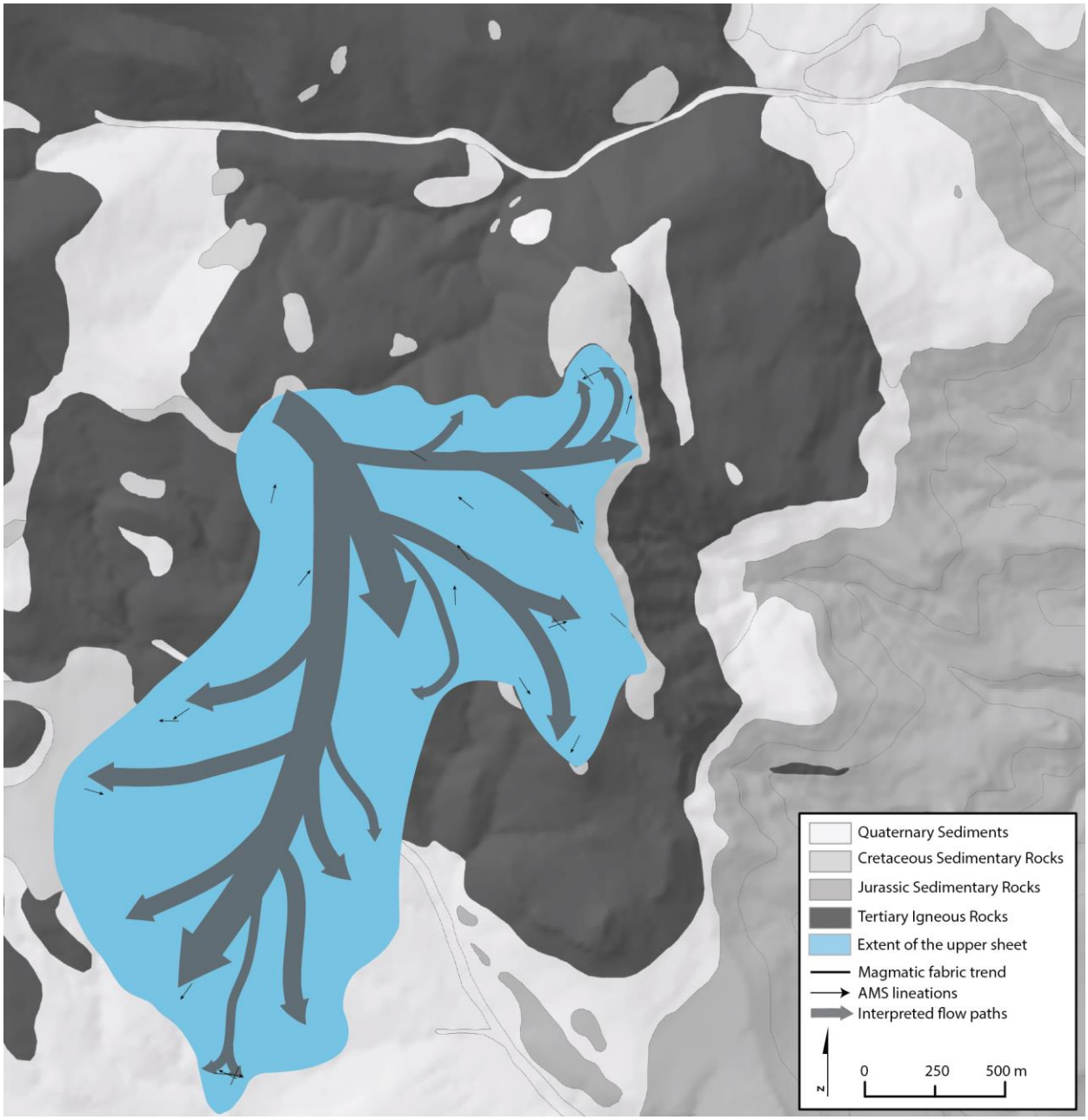

Figure 44. Interpreted flow paths during magma intrusion and formation of the upper sheet. Thin black lines with arrowheads indicate AMS lineations, and plain thin black lines indicate field fabric measurements.

Figure 45. Interpreted flow paths during magma intrusion and formation of the lower sheet. Thin black lines with arrowheads indicate AMS lineations, and plain thin black lines indicate field fabric measurements.

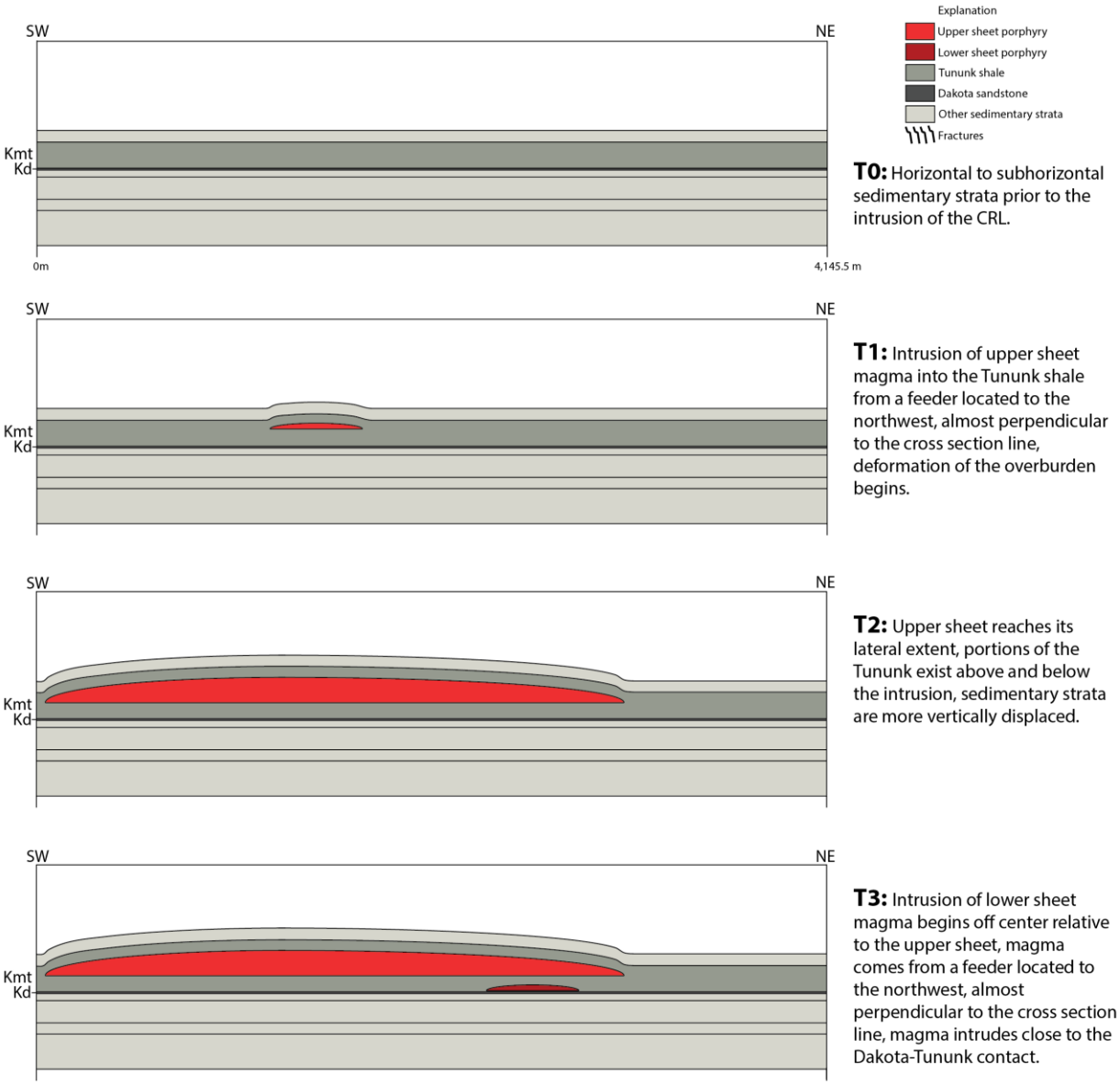

Figure 46. Cross sectional construction model for CRL with no vertical exaggeration.

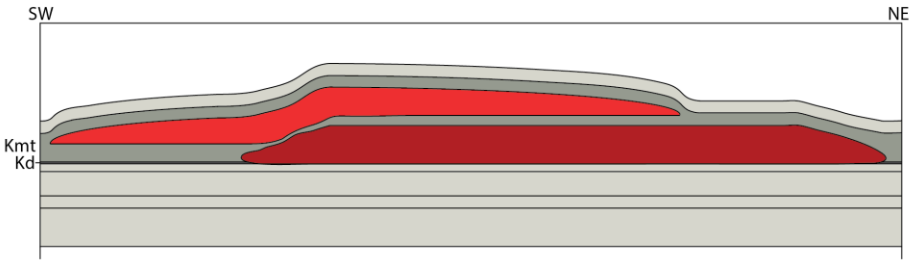

T4: Lower sheet spreads to lateral extent, simultaneously inflating and lifting the overburden, sedimentary strata offset increases and the upper sheet begins to bend, much of the Dakota is destroyed during the intrusion.

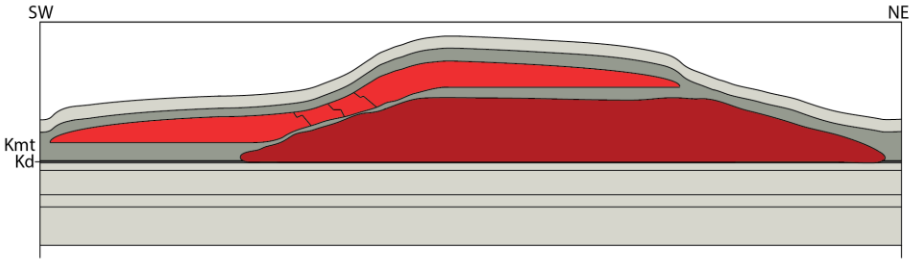

T5: Further inflation of the lower sheet causes more vertical displacement of the upper sheet and overlying sedimentary strata, fractures form in the hinge of the bent upper sheet.

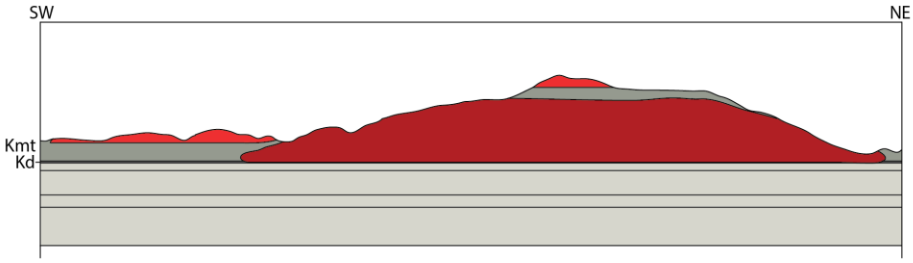

T6: Final intrusion geometry with modern topography, erosion of the upper sheet is facilitated by fracturing, causing the upper sheet to appear segmented in modern day outcrops, Tununk is preserved between the upper and lower sheet.

Conclusions

A wide variety of datasets suggest that CRL is composed of two different sheets. A well-preserved layer of Cretaceous Tununk separates the upper and lower sheets of the CRL in several locations. CSD data agree with two distinct pulses of magma forming CRL. The lower sheet has smaller plagioclase crystals than the upper sheet, suggesting the two had different crystallization histories at depth. The magma that formed the lower sheet likely spent less time at depth than the upper sheet. The upper and lower sheet are also chemically different. The lower sheet has higher SiO_2 concentrations relative to the upper sheet, and the upper sheet has higher concentrations of all of the rare earth elements, as well as several other trace elements. AMS data suggest magma for both sheets flowed outward from a feeder in the northwest. Magma likely flowed through a main channel and then spread radially in a fanning pattern. The spreading of magma in a fanlike pattern resulted in an asymmetric tongue-shaped laccolith.

It is likely that upper sheet magma intruded first, exploiting weaknesses in the Tununk and spreading radially out from a central flow channel. As magma spread, it made space for itself by lifting the overlying Tununk, which is locally preserved as cap rock on top of CRL. The magma that formed the lower sheet likely moved in a similar manner to the upper sheet, spreading through a main flow path and fanning out radially. The lower sheet is a much larger volume of magma so the vertical displacement of the overburden was much greater. As the lower sheet vertically displaced the upper sheet, fractures and faults formed in the central limb of the upper sheet monocline. Fractures facilitated weathering and erosion of the central limb in the upper sheet, causing the upper sheet to appear segmented in modern exposures.

References Cited

Bagnold, R.A., 1954, Experiments on a gravity-free dispersion of large solid spheres in a Newtonian fluid under shear: Proceedings of the Royal Society of London. Series A, Mathematical and Physical Sciences, v. 225, no. 1160, p. 49–63.

Beghoul, N., and Barazangi, M., 1989, Mapping high Pn velocity beneath the Colorado Plateau constrains uplift models: Journal of Geophysical Research: Solid Earth (1978–2012), v. 94, no. B6, p. 7083–7104.

Bouchez, J.L., 1997, Granite is never isotropic: an introduction to AMS studies of granitic rocks, *in* Bouchez, J.L., Hutton, D.H.W., and Stephens, W.E., eds., Granite: From Segregation of Melt to Emplacement Fabrics: Springer, Netherlands, p. 95-112.

Broda, R.J., 2014, Geometry and progressive development of a shallow crustal intrusive complex, Mount Hillers, Henry Mountains, Utah [Master's Thesis]: East Carolina University, 111 p.

Cashman, K.V., and Marsh, B.D., 1988, Crystal size distribution (CSD) in rocks and the kinetics and dynamics of crystallization II: Makaopuhi lava lake: Contributions to Mineralogy and Petrology, v. 99, no. 3, p. 292–305.

Clemens, J.D., and Mawer, C.K., 1992, Granitic magma transport by fracture propagation: Tectonophysics, v. 204, no. 3–4, p. 339–360.

Clemens, J.D., and Petford, N., 1999, Granitic melt viscosity and silicic magma dynamics in contrasting tectonic settings: Journal of the Geological Society, London, v. 156, p. 1057–1060.

Coleman, D.S., Gray, W., and Glazner, A.F., 2004, Rethinking the emplacement and evolution of zoned plutons: Geochronologic evidence for incremental assembly of the Tuolumne Intrusive Suite, California: Geology, v. 32, no. 5, p. 433-436.

Cook, J., Gordon, J.E., Evans, C.C., and Marsh, D.M., 1964, A mechanism for the control of crack propagation in all-brittle systems: Proceedings of the Royal Society of London. Series A, Mathematical and Physical Sciences, v. 282, no. 1391, p. 508–520.

Correa-Gomes, L.C., Souza Filho, C.R., Martins, C.J.F.N., and Oliveira, E.P., 2001, Development of symmetrical and asymmetrical fabrics in sheet-like igneous bodies: The role of magma flow and wall-rock displacements in theoretical and natural cases: Journal of Structural Geology, v. 23, no. 9, p. 1415-1428.

Corry, C.E., 1988, Laccoliths: Mechanics of Emplacement and Growth: Geological Society of America Special Paper 220, 127 p.

Gilbert, G.K., 1877, Report on the geology of the Henry Mountains: U.S. Geological Survey, 170 p.

Glazner, A.F., Bartley, J.M., Coleman, D.S., Gray, W., and Taylor, R.Z., 2004, Are plutons assembled over millions of years by amalgamation from small magma chambers?: GSA Today, v. 14, no. 4/5, p. 4-12.

Gwyn, N.Z., 2011, Emplacement and growth of large complex intrusions in the shallow crust, Henry Mountains, Utah [Master's Thesis]: East Carolina University, 89 p.

Higgins, M.D., 1996, Magma dynamics beneath Kameni Volcano, Thera, Greece, as revealed by crystal size and shape measurements: Journal of Volcanology and Geothermal Research, v. 70, no. 1–2, p. 37–48.

Higgins, M.D., 1998, Origin of anorthosite by textural coarsening: Quantitative measurements of a natural sequence of textural development: Journal of Petrology, v. 39, no. 7, p. 1307–1323.

Higgins, M.D., 2000, Measurement of crystal size distributions: American Mineralogist, v. 85, no. 8-9, p. 1105–1116.

Higgins, M.D., and Roberge, J., 2003, Crystal size distribution of plagioclase and amphibole from Soufrière Hills volcano, Montserrat: Evidence for dynamic crystallization-textural coarsening cycle: Journal of Petrology, v. 44, no. 8, p. 1401-1411.

Horsman, E., Morgan, S., de Saint-Blanquat, M., Habert, G., Nugent, A., Hunter, R.A., and Tikoff, B., 2010, Emplacement and assembly of shallow intrusions from multiple magma pulses, Henry Mountains, Utah: Earth and Environmental Science Transactions of the Royal Society of Edinburgh, v. 100, no. 1-2, p. 117–132.

Horsman, E., Tikoff, B., and Morgan, S., 2005, Emplacement-related fabric and multiple sheets in the Maiden Creek sill, Henry Mountains, Utah, USA: Journal of Structural Geology, v. 27, no. 8, p. 1426–1444.

Hunt, C.B., 1956, Cenozoic Geology of the Colorado Plateau: US Geological Survey Professional Paper 279, 99 p.

Hunt, C.B., Averitt, P., and Miller, R.L., 1953, Geology and Geography of the Henry Mountains Region, Utah: US Geological Survey Professional Paper 228, 234 p.

Jackson, M.D., and Pollard, D.D., 1988, The laccolith-stock controversy: New results from the southern Henry Mountains, Utah: Geological Society of America Bulletin, v. 100, no. 1, p. 117–139.

Johnson, A.M., and Pollard, D.D., 1973, Mechanics of growth of some laccolithic intrusions in the Henry Mountains, Utah, I: Field observations, Gilbert's model, physical properties and flow of the magma: Tectonophysics, v. 18, no. 3–4, p. 261–309.

Kavanagh, J.L., Menand, T., and Sparks, R.S.J., 2006, An experimental investigation of sill formation and propagation in layered elastic media: Earth and Planetary Science Letters, v. 245, no. 3–4, p. 799–813.

Knight, M.D., and Walker, G.P.L., 1988, Magma flow directions in dikes of the Koolau Complex, Oahu, determined from magnetic fabric studies: Journal of Geophysical Research: Solid Earth, v. 93, no. B5, p. 4301–4319.

Komar, P., 1972a, Flow differentiation in igneous dikes and sills: Profiles of velocity and phenocryst concentration: Geological Society of America Bulletin, v. 83, no. 11, p. 3443–3448.

Komar, P., 1972b, Mechanical interactions of phenocrysts and flow differentiation of igneous dikes and sills: Geological Society of America Bulletin, v. 83, no. 4, p. 973–988.

Kornprobst, J., 2002, Metamorphic Rocks and Their Geodynamic Significance: Dordrecht, Kluwer Academic Publishers, 206 p.

Le Bas, M.J., Lemaitre, R.W., Streckeisen, A., and Zanettin, B. (1986). A chemical classification of volcanic-rocks based on the total alkali silica diagram: Journal of Petrology, v. 27, no. 3, p. 745-750.

Marsh, B.D., 1988, Crystal size distribution (CSD) in rocks and the kinetics and dynamics of crystallization: Contributions to Mineralogy and Petrology, v. 99, no. 3, p. 277–291.

Marsh, B.D., 1998, On the interpretation of crystal size distributions in magmatic systems: Journal of Petrology, v. 39, no. 4, p. 553–599.

McDonough, W.F., and Sun, S.-s., 1995, The composition of the Earth: Chemical Geology, v. 120, no. 3–4, p. 223–253.

Menand, T., 2011, Physical controls and depth of emplacement of igneous bodies: A review: Tectonophysics, v. 500, no. 1-4, p. 11–19.

Michel, J., Baumgartner, L., Putlitz, B., Schaltegger, U., and Ovtcharova, M., 2008, Incremental growth of the Patagonian Torres del Paine laccolith over 90 ky: Geology, v. 36, no. 6, p. 459–462.

Mock, A., Jerram, D.A., and Breitkreuz, C., 2003, Using quantitative textural analysis to understand the emplacement of shallow-level rhyolitic laccoliths—A case study from the Halle Volcanic Complex, Germany: Journal of Petrology, v. 44, no. 5, p. 833–849.

Morgan, S., Stanik, A., Horsman, E., Tikoff, B., de Saint Blanquat, M., and Habert, G., 2008, Emplacement of multiple magma sheets and wall rock deformation: Trachyte Mesa intrusion, Henry Mountains, Utah: Journal of Structural Geology, v. 30, no. 4, p. 491–512.

Morton, L.B., 1984, Geology of the Mount Ellen Quadrangle, Henry Mountains, Garfield County, Utah [Master's Thesis]: Brigham Young University, 30 p.

Morton, L.B., 1986, Provisional geologic and coal resource map of the Mt. Ellen quadrangle, Garfield County, Utah [Master's Thesis]: Brigham Young University, scale: 1:24,000.

Nelson, S.T., and Davidson, J.P., 1993, Interactions between mantle-derived magmas and mafic crust, Henry Mountains, Utah: Journal of Geophysical Research: Solid Earth, v. 98, no. B2, p. 1837–1852.

Nelson, S.T., and Davidson, J.P., 1998, The petrogenesis of the Colorado Plateau laccoliths and their relationship to regional magmatism, in laccolithic complexes of southeastern Utah: Time of Emplacement and Tectonic Setting—Workshop Proceedings, p. 85–100.

Nelson, S.T., Davidson, J.P., and Sullivan, K.R., 1992, New age determinations of central Colorado Plateau laccoliths, Utah: Recognizing disturbed K-Ar systematics and re-evaluating tectonomagmatic relationships: Geological Society of America Bulletin, v. 104, no. 12, p. 1547–1560.

Petford, N., Cruden, A.R., McCaffrey, K.J.W., and Vigneresse, J.-L., 2000, Granite magma formation, transport and emplacement in the Earth's crust: Nature, v. 408, no. 6813, p. 669–673.

Petford, N., Kerr, R.C., and Lister, J.R., 1993, Dike transport of granitoid magmas: Geology, v. 21, no. 9, p. 845–848.

Philpotts, A.R., and Asher, P.M., 1994, Magmatic flow-direction indicators in a giant diabase feeder dike, Connecticut: Geology, v. 22, no. 4, p. 363-366.

Pitcher, W.S., 1979, The nature, ascent and emplacement of granitic magmas: Journal of the Geological Society, v. 136, no. 6, p. 627–662.

Pollard, D.D., and Johnson, A.M., 1973, Mechanics of growth of some laccolithic intrusions in the Henry Mountains, Utah, II: Bending and failure of overburden layers and sill formation: Tectonophysics, v. 18, no. 3–4, p. 311–354.

Pollard, D.D., Muller, O.H., and Dockstader, D.R., 1975, The form and growth of fingered sheet intrusions: Geological Society of America Bulletin, v. 86, no. 3, p. 351–363.

Pollard, D.D., 1973, Derivation and evaluation of a mechanical model for sheet intrusions: Tectonophysics, v. 19, no. 3, p. 233-269.

Rocchi, S., Westerman, D.S., Dini, A., and Farina, F., 2010, Intrusive sheets and sheeted intrusions at Elba Island, Italy: Geosphere, v. 6, no. 3, p. 225–236.

Rocchi, S., Westerman, D.S., Dini, A., Innocenti, F., and Tonarini, S., 2002, Two-stage growth of laccoliths at Elba Island, Italy: Geology, v. 30, no. 11, p. 983–986.

Rochette, P., Jackson, M., and Aubourg, C., 1992, Rock magnetism and the interpretation of anisotropy of magnetic susceptibility: Reviews of Geophysics, v. 30, no. 3, p. 209–226.

Rollinson, H.R., 2013, Using Geochemical Data: Evaluation, Presentation, Interpretation: New York, Routledge, 352 p.

de Saint-Blanquat, M., Habert, G., Horsman, E., Morgan, S.S., Tikoff, B., Launeau, P., and Gleizes, G., 2006, Mechanisms and duration of non-tectonically assisted magma

emplacement in the upper crust: The Black Mesa pluton, Henry Mountains, Utah: Tectonophysics, v. 428, no. 1-4, p. 1–31.

de Saint Blanquat, M., Horsman, E., Habert, G., Morgan, S., Vanderhaeghe, O., Law, R., and Tikoff, B., 2011, Multiscale magmatic cyclicity, duration of pluton construction, and the paradoxical relationship between tectonism and plutonism in continental arcs: Tectonophysics, v. 500, no. 1-4, p. 20–33.

Schmiedel, T., Breitkreuz, C., Görz, I., and Ehling, B.C., 2014, Geometry of laccolith margins: 2D and 3D models of the Late Paleozoic Halle Volcanic Complex (Germany): International Journal of Earth Sciences, v. 104, p. 323-333.

Stevenson, C.T., Owens, W.H., and Hutton, D.H., 2007, Flow lobes in granite: The determination of magma flow direction in the Trawenagh Bay Granite, northwestern Ireland, using anisotropy of magnetic susceptibility: Geological Society of America Bulletin, v. 119, no. 11-12, p. 1368–1386.

Tarling, D.H., and Hrouda, F., 1993, The Magnetic Anisotropy of Rocks: Chapman & Hall, London, 217 p.

Thompson, G.A., and Zoback, M.L., 1979, Regional geophysics of the Colorado Plateau: Tectonophysics, v. 61, no. 1–3, p. 149–181.

Thornton, E.D., 2015, Timing, internal flow characteristics, and emplacement mechanisms of the intrusive sheet network on the southern margin of Mount Hillers, Henry Mountains, southern Utah [Master's Thesis]: East Carolina University, 104 p.

Vigneresse, J.L., and Clemens, J.D., 2000, Granitic magma ascent and emplacement: Neither diapirism nor neutral buoyancy: Geological Society, London, Special Publications, v. 174, no. 1, p. 1–19.

Ward, M.T., 2014, Geometry and construction history of a complex intrusive center in the shallow crust, Mount Pennell, Henry Mountains, Utah [Master's Thesis]: East Carolina University, 114 p.

Appendix A: Annotated Maps of the Copper Ridge Laccolith

Maurer (2015)

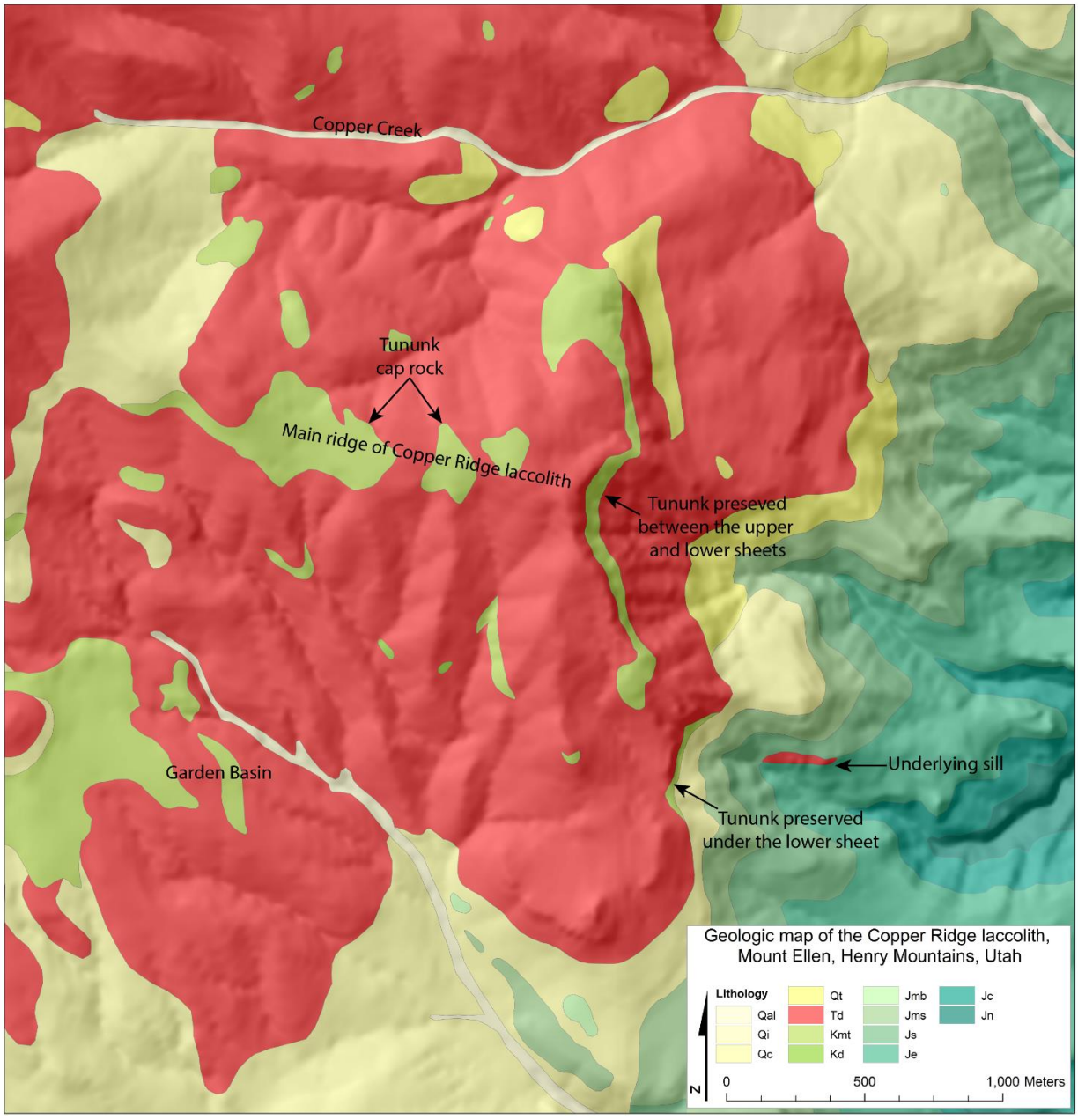

Figure 47. Geologic map of CRL made for this project. Geographic regions mentioned in the text are labeled, and Tununk preserved within the intrusion, as cap rock, and under the intrusion are labeled.

Hunt et al. (1953)

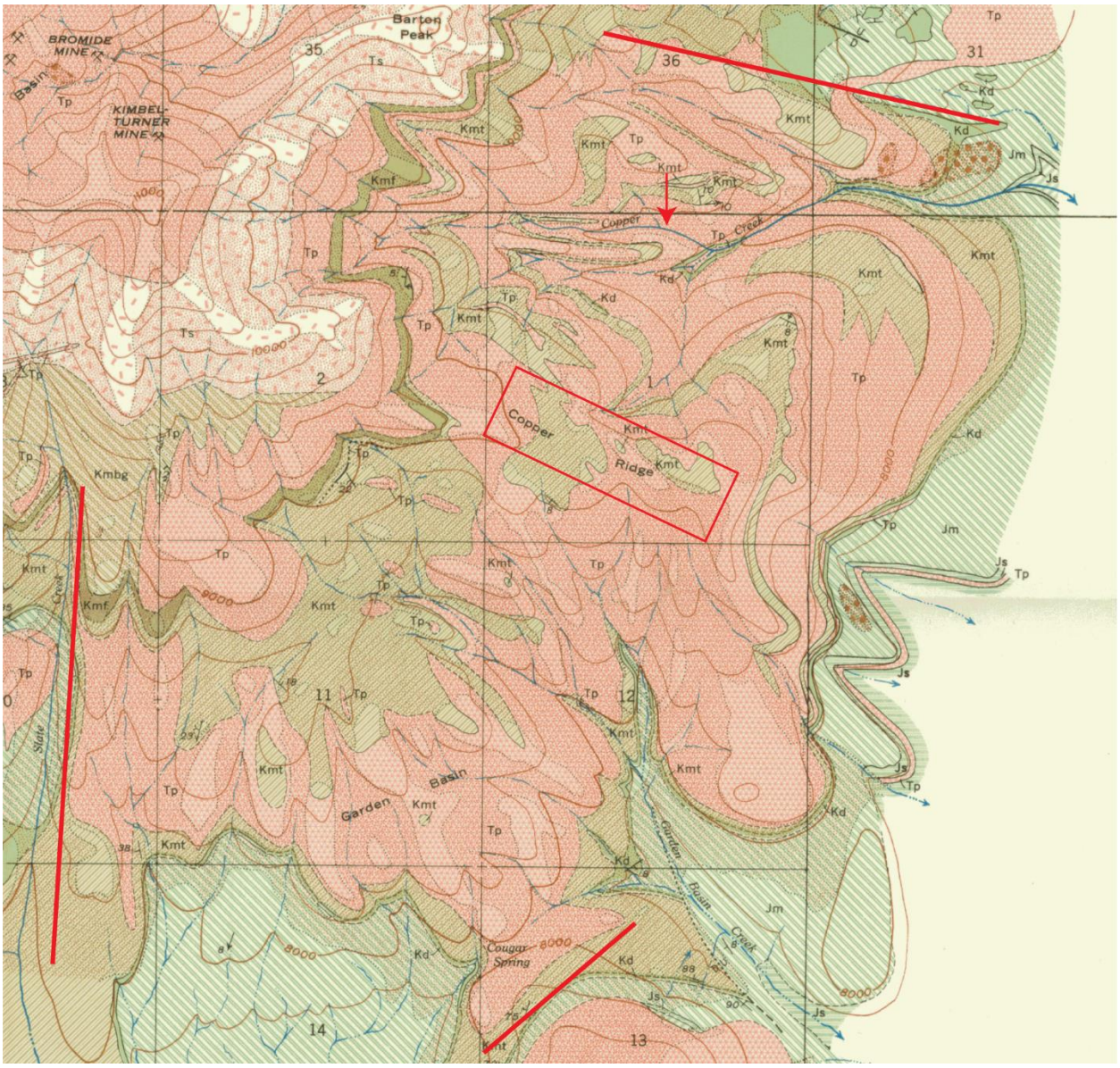

Figure 48. Map from Hunt et al. (1953) with the main CRL ridge outlined in a red box, Copper Creek is labeled by a red arrow, and the author's hypothesized extent of CRL labeled by red lines.

Morton (1986)

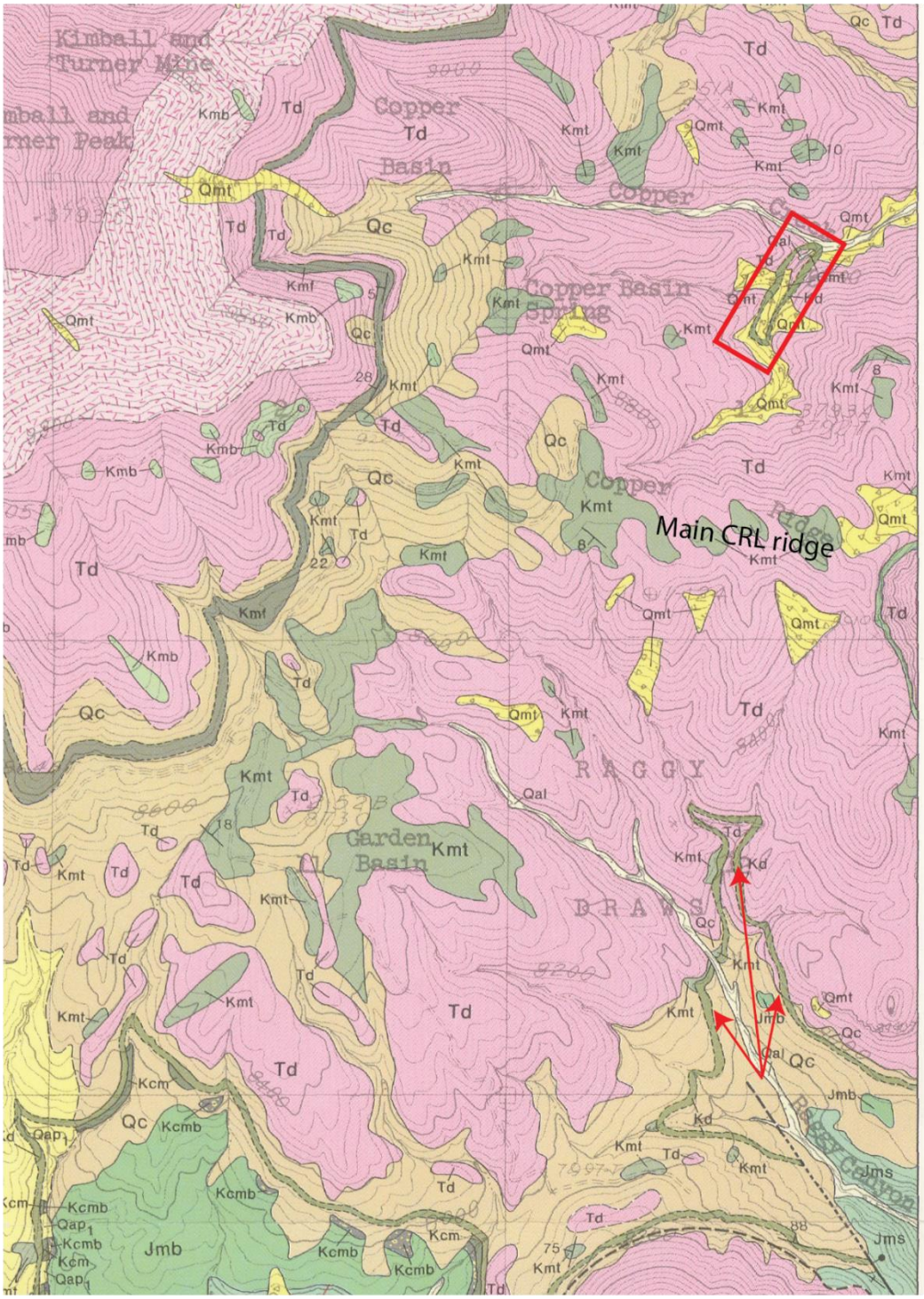

Figure 49. Map from Morton (1986) with the main CRL ridge labeled, the "ring of Dakota" outlined in a red box, and the continuous layer of Dakota labeled by red arrows.

Appendix B: Crystal Size Distribution Data

Table 2: CSD data for plagioclase phenocrysts

Upper Sheet CSD for Plagioclase Phenocrysts						
Sample #	CR19		CR48		CR59	
	Crystal Size (mm)	(ln) Pop. density	Crystal Size (mm)	(ln) Pop. density	Crystal Size (mm)	(ln) Pop. density
	12.7	-13.89	12.7	-15.28	5.06	-10.91
	8.01	-12.86	8.01	-13.74	3.19	-8.32
	5.06	-9.61	5.06	-10.32	2.01	-6.93
	3.19	-8.07	3.19	-7.88	1.27	-5.55
	2.01	-6.76	2.01	-6.44	0.801	-5.07
	1.27	-5.38	1.27	-5.08		
	0.801	-4.95	0.801	-4.74		
Sample #	CR84		CR95		ME9a	
	Crystal Size (mm)	(ln) Pop. density	Crystal Size (mm)	(ln) Pop. density	Crystal Size (mm)	(ln) Pop. density
	8.01	-13.76	8.01	-12.57	12.7	-15.24
	5.06	-10.92	5.06	-10.29	8.01	-13.7
	3.19	-8.47	3.19	-8.33	5.06	-9.79
	2.01	-7	2.01	-6.92	3.19	-7.64
	1.27	-5.63	1.27	-5.54	2.01	-5.95
	0.801	-5.11	0.801	-4.47	1.27	-4.77

Lower Sheet CSD for Plagioclase Phenocrysts						
Sample #	CR2		CR9a		CR14	
	Crystal Size (mm)	(ln) Pop. density	Crystal Size (mm)	(ln) Pop. density	Crystal Size (mm)	(ln) Pop. density
	8.01	-14.33	8.01	-14.33	3.19	-8.51
	5.06	-11.83	5.06	-10.94	2.01	-6.33
	3.19	-8.46	3.19	-8.49	1.27	-4.81
	2.01	-6.46	2.01	-6.45	0.801	-3.71
	1.27	-4.85	1.27	-4.98		
	0.801	-4.25	0.801	-4.65		
Sample #	CR62		CR88		ME7	
	Crystal Size (mm)	(ln) Pop. density	Crystal Size (mm)	(ln) Pop. density	Crystal Size (mm)	(ln) Pop. density
	5.06	-11.7	5.06	-10.83	5.06	-12.3
	3.19	-8.73	3.19	-8.71	3.19	-8.97
	2.01	-7.23	2.01	-7.22	2.01	-6.97
	1.27	-5.84	1.27	-5.88	1.27	-5.32
	0.801	-4.93	0.801	-5.03	0.801	-4.2
			0.506	-4.49		

CSD data for plagioclase phenocrysts, continued

Not CRL CSD for Plagioclase Phenocrysts		
Sample #	CR38	
	Crystal Size (mm)	(ln) Pop. density
	8.01	-13.24
	5.06	-10.66
	3.19	-7.99
	2.01	-6.39
	1.27	-4.98
	0.801	-4.24

Appendix C: Geochemistry Data

Table 3: Whole-rock major element geochemistry data for upper sheet samples

Upper Sheet Geochemistry Data- Major Elements									
	Sample #								
Major Element (wt. %)	CR19	CR66	CR71	CR82	CR95	CR114	ME8	ME9	Average
SiO_2	58.65	58.12	58.72	59.09	58.12	60.11	59.82	59.93	59.07
Al_2O_3	17.02	16.98	16.75	17.28	16.71	17.34	17.41	17.46	17.12
Fe_2O_3	6.90	6.67	7.14	7.27	6.88	6.59	6.86	6.90	6.90
MgO	1.97	1.66	1.79	2.02	1.60	1.95	1.94	1.86	1.85
CaO	6.19	6.62	6.32	5.26	6.41	5.44	4.52	5.43	5.77
Na_2O	4.25	4.31	4.13	5.05	4.19	4.30	4.59	4.19	4.38
K_2O	1.87	1.89	1.9	1.86	1.71	1.86	1.88	1.84	1.85
TiO_2	0.61	0.60	0.59	0.62	0.57	0.59	0.61	0.60	0.60
P_2O_5	0.21	0.22	0.21	0.23	0.22	0.21	0.24	0.22	0.22
MnO	0.13	0.11	0.14	0.15	0.12	0.13	0.12	0.13	0.13
Cr_2O_3	0.004	0.004	0.004	0.003	0.004	0.003	0.003	0.004	0.004
LOI	1.90	2.50	2.00	0.90	3.20	1.20	1.70	1.20	1.83
Total	99.70	99.68	99.69	99.73	99.73	99.72	99.69	99.76	99.72

Table 4: Whole-rock major element geochemistry data for lower sheet samples

Lower Sheet Geochemistry Data- Major Elements							
	Sample #						
Major Element (wt%)	CR8	CR63	CR76	CR88	CR81	CR104	Average
SiO_2	61.95	62.22	61.23	61.95	62.26	63.20	62.14
Al_2O_3	16.96	17.43	16.92	16.60	17.06	17.16	17.02
Fe_2O_3	5.07	5.95	5.47	5.95	5.85	5.28	5.60
MgO	1.21	1.49	1.32	1.40	1.29	1.26	1.33
CaO	5.30	5.06	5.09	5.00	4.34	5.09	4.98
Na_2O	4.53	4.57	4.82	4.57	5.17	4.41	4.68
K_2O	1.70	1.85	1.77	1.99	1.82	1.83	1.83
TiO_2	0.43	0.46	0.45	0.45	0.45	0.44	0.45
P_2O_5	0.20	0.21	0.20	0.21	0.21	0.19	0.20
MnO	0.10	0.18	0.12	0.13	0.14	0.10	0.13
Cr_2O_3	<0.002	<0.002	0.002	<0.002	<0.002	<0.002	-
LOI	2.30	0.30	2.30	1.50	1.10	0.80	1.38
Total	99.75	99.72	99.69	99.75	99.69	99.76	99.73

Table 5: Whole-rock major element geochemistry data for not-CRL samples

Not CRL Geochemistry Data- Major Elements					
	Sample #				
Major Element (wt. %)	CR37	CR100	CR82	CR95	Average
SiO_2	52.96	56.29	59.09	58.12	56.62
Al_2O_3	15.53	16.53	17.28	16.71	16.51
Fe_2O_3	8.33	7.30	7.27	6.88	7.45
MgO	3.26	2.67	2.02	1.60	2.39
CaO	7.41	6.63	5.26	6.41	6.43
Na_2O	3.55	4.05	5.05	4.19	4.21
K_2O	1.31	1.82	1.86	1.71	1.68
TiO_2	0.68	0.68	0.62	0.57	0.64
P_2O_5	0.25	0.24	0.23	0.22	0.24
MnO	0.15	0.13	0.15	0.12	0.14
Cr_2O_3	0.009	0.005	0.003	0.004	0.01
LOI	6.20	3.30	0.90	3.20	3.40
Total	99.64	99.65	99.73	99.73	99.69

Table 6: Whole-rock trace element geochemistry data for upper sheet samples

Upper Sheet Geochemistry Data- Trace Elements									
	Sample #								
Trace Element (ppm)	CR19	CR66	CR71	CR82	CR95	CR114	ME8	ME9	Average
Sc	10	10	9	10	9	10	10	10	10
Ba	718	699	680	625	701	657	737	741	695
Be	2	<1	<1	<1	<1	<1	<1	<1	-
Co	12.3	11.8	10.8	10.8	11.3	10.4	11.2	11.4	11.3
Cs	0.6	0.6	0.6	0.3	0.7	0.6	1.4	0.6	0.7
Ga	18.6	19	18.6	19.6	18.1	18.4	18	20.2	18.8
Hf	3.7	3.1	3.8	3.6	3.5	3.7	3.6	3.7	3.6
Nb	6.2	5.7	6.3	6.6	5.9	6.4	5.9	6.4	6.2
Rb	26.8	29.7	30.5	27.7	26.5	25.7	28.3	26.7	27.7
Sn	1	<1	1	<1	<1	<1	<1	<1	-
Sr	1020.7	918.1	991.2	893.9	993.8	1029	967.1	1019.6	979.2
Ta	0.3	0.3	0.3	0.3	0.3	0.3	0.3	0.4	0.3
Th	3.1	2.9	2.2	2.4	3.4	2.7	2.4	2.9	2.8
U	1.3	1	1.1	1.3	1.1	1.2	0.9	1	1.1
V	101	103	92	104	96	100	105	105	101
W	<0.5	<0.5	0.8	<0.5	<0.5	<0.5	<0.5	<0.5	-

Whole-rock trace element geochemistry data for upper sheet samples, continued

Upper Sheet Geochemistry Data- Trace Elements									
	Sample #								
Trace Element (ppm)	CR19	CR66	CR71	CR82	CR95	CR114	ME8	ME9	Average
Zr	136.2	128.7	155.9	141.6	131.4	130.1	135.9	138.2	137.3
Y	19.3	19.6	19.3	19.5	18.2	19.3	18.2	19.8	19.2
La	24.2	21.7	18.1	19.6	23.3	18.4	17.9	25.8	21.1
Ce	47.6	43.3	36.5	41.9	47.7	37.1	37.5	48.7	42.5
Pr	5.92	5.21	4.76	5.31	5.54	4.93	4.76	5.66	5.26
Nd	23.2	22.5	18.9	21.2	23.6	18.9	18.2	23	21.2
Sm	4.23	4.36	3.96	4.67	4.3	4.18	4.02	4.58	4.29
Eu	1.28	1.29	1.23	1.31	1.26	1.33	1.26	1.34	1.29
Gd	3.87	3.88	3.82	4.07	3.93	3.86	3.6	4.22	3.91
Tb	0.58	0.57	0.57	0.59	0.56	0.58	0.53	0.63	0.58
Dy	3.15	3.3	3.28	3.43	3.45	3.19	3.17	3.33	3.29
Ho	0.66	0.72	0.64	0.71	0.63	0.68	0.64	0.68	0.67
Er	2.02	2.01	2.18	2.05	1.95	1.85	1.83	1.94	1.98
Tm	0.3	0.3	0.32	0.33	0.28	0.3	0.29	0.3	0.30
Yb	2.04	2	1.98	1.86	1.8	1.97	2.02	1.99	1.96
Lu	0.31	0.31	0.31	0.3	0.31	0.3	0.32	0.32	0.31
Mo	0.4	0.3	0.3	0.3	0.5	0.2	0.3	0.1	0.3
Cu	19	21.2	19.1	17.6	18.8	20.2	25.5	20.6	20.25
Pb	4	4.1	4.9	32	3.7	2.9	3.4	2	7.1
Zn	47	31	58	173	57	39	43	37	61
Ni	8	6.7	5.2	5	7.9	5.3	7.9	5.9	6.5
As	1.1	0.9	1	0.7	0.6	<0.5	<0.5	<0.5	-
Cd	<0.1	<0.1	<0.1	0.3	<0.1	<0.1	<0.1	<0.1	-
Sb	<0.1	<0.1	<0.1	0.1	<0.1	<0.1	<0.1	<0.1	-
Bi	<0.1	<0.1	<0.1	<0.1	<0.1	<0.1	<0.1	<0.1	-
Ag	<0.1	<0.1	<0.1	0.1	<0.1	<0.1	<0.1	<0.1	-
Au (ppb)	<0.5	<0.5	<0.5	0.6	<0.5	<0.5	<0.5	<0.5	-
Hg	<0.01	<0.01	<0.01	<0.01	<0.01	<0.01	<0.01	<0.01	-
Tl	<0.1	<0.1	<0.1	<0.1	<0.1	<0.1	<0.1	<0.1	-
Se	<0.5	<0.5	<0.5	<0.5	<0.5	<0.5	<0.5	<0.5	-

Table 7: Whole-rock trace element geochemistry data for lower sheet samples

Lower Sheet Geochemistry Data- Trace Elements							
	Sample #						
Trace Element (ppm)	CR8	CR63	CR76	CR88	CR81	CR104	Average
Sc	6	7	6	6	6	7	6
Ba	889	850	994	934	970	812	908
Be	2	<1	<1	<1	2	<1	-
Co	6.5	7.6	7.8	7.4	7.5	6.8	7.3
Cs	1.1	1.1	0.7	0.8	1.6	0.8	1.0
Ga	17.8	19	18.5	18.6	18.7	17.6	18.4
Hf	3.1	3.2	2.9	2.8	3.1	3	3.0
Nb	5.5	5.3	5.8	5.3	5.6	4.7	5.4
Rb	26.8	32	29.4	35.2	29.4	29.1	30.3
Sn	<1	<1	<1	<1	<1	<1	-
Sr	1021.2	1020.8	1196.5	1042.5	1202.6	1037.9	1086.9
Ta	0.2	0.3	0.2	0.2	0.3	0.3	0.3
Th	2.7	2.7	2.7	2.5	2.4	2.3	2.6
U	0.9	1.1	0.9	0.9	0.9	1	1.0
V	60	65	62	67	63	62	63
W	0.6	<0.5	<0.5	<0.5	<0.5	<0.5	-
Zr	117.7	116.3	113.5	107.1	112.8	109.6	112.8
Y	14.6	15.4	14.8	14.6	14.5	14.5	14.7
La	15.4	19.6	17.5	16.9	16.3	16	17.0
Ce	32.1	36.7	34.9	31.5	33.5	31.4	33.4
Pr	3.98	4.85	4.64	4.13	4.3	4.09	4.33
Nd	16.9	20.8	19	18.5	18	18.1	18.6
Sm	3.72	3.51	4	3.76	3.84	3.51	3.72
Eu	1.04	1.19	1.16	1.17	1.21	0.99	1.13
Gd	3.06	3.6	3.44	3.34	3.23	3.06	3.29
Tb	0.43	0.46	0.48	0.48	0.46	0.43	0.46
Dy	2.52	2.58	2.49	2.67	2.64	2.61	2.59
Ho	0.48	0.5	0.51	0.49	0.49	0.52	0.50
Er	1.44	1.56	1.43	1.58	1.51	1.33	1.48
Tm	0.21	0.22	0.22	0.21	0.22	0.21	0.22
Yb	1.39	1.53	1.5	1.58	1.55	1.37	1.49
Lu	0.22	0.24	0.23	0.24	0.23	0.22	0.23
Mo	0.3	0.4	0.2	0.3	0.4	0.2	0.3
Cu	6.4	14.4	9.2	11.9	10.7	5.4	9.7
Pb	3.1	7.5	6.4	5	4.8	4.2	5.2
Zn	40	69	53	67	44	31	51

Whole-rock trace element geochemistry data for lower sheet samples, continued

Lower Sheet Geochemistry Data- Trace Elements							
	Sample #						
Trace Element (ppm)	CR8	CR63	CR76	CR88	CR81	CR104	Average
Ni	3.2	3	3	3.2	2.6	2.6	2.9
As	0.6	1	6.4	2.1	0.8	1.4	2.9
Cd	<0.1	<0.1	<0.1	0.1	0.4	<0.1	-
Sb	<0.1	0.1	0.2	<0.1	<0.1	0.1	-
Bi	<0.1	<0.1	<0.1	<0.1	<0.1	<0.1	-
Ag	<0.1	<0.1	<0.1	<0.1	<0.1	<0.1	-
Au (ppb)	<0.5	<0.5	<0.5	<0.5	<0.5	<0.5	-
Hg	<0.01	<0.01	<0.01	<0.01	0.01	<0.01	-
Tl	<0.1	<0.1	<0.1	<0.1	<0.1	<0.1	-
Se	<0.5	0.6	<0.5	<0.5	<0.5	<0.5	-

Table 8: Whole-rock trace element geochemistry data for not-CRL samples

Not CRL Geochemistry Data- Trace Elements					
	Sample #				
Trace Element (ppm)	CR37	CR100	CR82	CR95	Average
Sc	16	12	10	9	12
Ba	700	725	625	701	688
Be	<1	<1	<1	<1	-
Co	21.2	15.4	10.8	11.3	14.7
Cs	0.7	0.4	0.3	0.7	0.5
Ga	17.6	18.5	19.6	18.1	18.5
Hf	2.8	2.9	3.6	3.5	3.2
Nb	4.7	5	6.6	5.9	5.6
Rb	18.1	28.9	27.7	26.5	25.3
Sn	1	<1	<1	<1	-
Sr	1121.6	1102.1	893.9	993.8	1027.9
Ta	0.3	0.3	0.3	0.3	0.3
Th	5	4.2	2.4	3.4	3.8
U	1.5	1.5	1.3	1.1	1.4
V	170	141	104	96	128
W	<0.5	0.5	<0.5	<0.5	-
Zr	110.7	100.7	141.6	131.4	121.1
Y	19.5	15.9	19.5	18.2	18.3
La	30.6	26.9	19.6	23.3	25.1

Whole-rock trace element geochemistry data for not-CRL samples, continued

Not CRL Geochemistry Data- Trace Elements					
	Sample #				
Trace Element (ppm)	CR37	CR100	CR82	CR95	Average
Ce	55.9	49.7	41.9	47.7	48.8
Pr	6.58	6.01	5.31	5.54	5.86
Nd	27	23.7	21.2	23.6	23.9
Sm	4.88	4.48	4.67	4.3	4.58
Eu	1.42	1.38	1.31	1.26	1.34
Gd	4.47	3.98	4.07	3.93	4.11
Tb	0.61	0.53	0.59	0.56	0.57
Dy	3.17	3.09	3.43	3.45	3.29
Ho	0.73	0.57	0.71	0.63	0.66
Er	1.78	1.58	2.05	1.95	1.84
Tm	0.28	0.26	0.33	0.28	0.29
Yb	1.91	1.63	1.86	1.8	1.8
Lu	0.3	0.25	0.3	0.31	0.29
Mo	1.2	0.6	0.3	0.5	0.7
Cu	55.7	25.2	17.6	18.8	29.3
Pb	7.7	4.4	32	3.7	12.0
Zn	75	72	173	57	94
Ni	22.1	11.9	5	7.9	11.7
As	1.9	9.8	0.7	0.6	3.3
Cd	0.1	<0.1	0.3	<0.1	-
Sb	0.1	0.2	0.1	<0.1	-
Bi	<0.1	<0.1	<0.1	<0.1	-
Ag	<0.1	<0.1	0.1	<0.1	-
Au (ppb)	<0.5	<0.5	0.6	<0.5	-
Hg	<0.01	<0.01	<0.01	<0.01	-
Tl	<0.1	<0.1	<0.1	<0.1	-
Se	<0.5	<0.5	<0.5	<0.5	-

Appendix D: Anisotropy of Magnetic Susceptibility Data

Table 9: AMS data for upper sheet samples

Upper Sheet AMS data								
Name	**UTM E**	**UTM N**	**Num.**	**K_m (SI)**	**K_m 1 s (SI)***	**K1**	**K2**	**K3**
	Zone 12N (NAD83)							
ME8	521243	4210732	6	0.075300	0.001720	1.008	0.999	0.993
ME9	521274	4211060	6	0.042600	0.001380	1.009	0.999	0.992
CR3	521585	4211068	6	0.017800	0.000439	1.011	0.997	0.992
CR15	520710	4210792	6	0.000272	0.000016	1.014	0.997	0.989
CR18	520595	4211096	6	0.017900	0.000263	1.012	1.001	0.988
CR19	521687	4210995	5	0.019400	0.001730	1.012	0.998	0.990
CR48	521868	4211416	6	0.000367	0.000010	1.011	1.005	0.984
CR54	519964	4210017	6	0.000296	0.000015	1.009	1.002	0.989
CR59	521621	4210621	6	0.020900	0.000364	1.011	1.002	0.986
CR66	521670	4210179	6	0.033800	0.001940	1.013	0.999	0.988
CR71	521722	4211507	5	0.013600	0.000522	1.011	0.999	0.990
CR82	520421	4209011	6	0.009150	0.000766	1.008	1.004	0.988
CR83	520462	4209005	6	0.003140	0.000566	1.013	0.999	0.988
CR84	520277	4209295	5	0.005240	0.002700	1.028	0.988	0.984
CR86	520738	4211618	6	0.000335	0.000092	1.012	0.999	0.989
CR95	520210	4210273	6	0.028700	0.003290	1.014	1.005	0.981
CR96	520256	4210291	6	0.000312	0.000015	1.013	1.004	0.982
CR101	521500	4210388	6	0.018800	0.004380	1.013	0.999	0.988
CR114	521267	4210884	6	0.026900	0.001770	1.012	0.997	0.990

*One standard deviation

AMS data for upper sheet samples, continued

Upper Sheet AMS data												
Name	**K1**				**K2**				**K3**			
	decl.	**incl.**	**α_{95} max**	**α_{95} min**	**decl.**	**incl.**	**α_{95} max**	**α_{95} min**	**decl.**	**incl.**	**α_{95} max**	**α_{95} min**
ME8	358.3	65.5	6.6	4.0	195.3	23.6	10.0	5.6	102.5	6.4	10.3	4.3
ME9	308.9	42.1	14.4	2.1	68.2	28.4	15.7	7.6	180.2	34.7	12.4	3.7
CR3	312.3	41.0	7.4	1.8	92.2	41.3	16.2	3.7	202.3	21.4	15.5	3.2
CR15	37.9	58.2	6.3	2.6	151.8	14.1	11.4	2.5	249.4	27.8	12.2	4.3
CR18	13.5	1.6	3.4	1.3	283.4	3.7	3.4	2.3	127.0	85.9	2.6	1.1
CR19	140.1	7.3	3.1	2.5	248.0	67.4	7.5	2.9	47.2	21.3	7.5	2.5
CR48	14.7	33.2	16.3	3.3	233.6	49.9	16.1	3.2	118.3	19.8	5.5	2.2
CR54	106.3	54.0	9.7	1.2	318.0	31.7	10.7	4.7	218.3	15.2	7.1	2.0
CR59	71.4	11.6	8.4	1.7	330.0	44.0	8.7	2.8	172.7	43.7	3.7	1.8
CR66	206.7	47.5	5.0	2.2	39.4	41.8	9.3	1.7	303.7	6.4	10.1	2.3
CR71	244.3	11.3	12.5	7.2	152.2	10.4	19.5	0.9	20.6	74.6	18.2	7.7
CR82	295.8	20.5	54.9	27.1	49.0	46.5	55.6	25.4	189.9	36.4	36.7	16.1
CR83	99.6	15.6	40.9	20.0	204.3	42.2	30.0	13.9	354.1	43.6	40.1	24.5
CR84	215.8	79.0	18.7	3.7	117.1	1.7	68.0	4.7	26.8	10.9	68.2	4.8
CR86	242.5	71.0	33.9	13.5	95.2	16.1	33.9	17.5	2.4	9.7	21.5	4.0
CR95	271.8	32.2	6.9	4.6	79.8	57.2	6.9	3.2	178.3	5.4	5.5	2.4
CR96	235.7	15.1	25.2	2.7	115.3	61.9	25.5	6.7	332.3	23.1	8.3	3.2
CR101	147.6	14.7	29.6	4.0	282.1	69.5	43.3	3.2	53.9	14.0	37.3	3.7
CR114	320.4	18.4	13.9	4.3	91.9	63.3	18.5	12.7	223.9	18.6	18.0	3.8

AMS data for upper sheet samples, continued

Upper Sheet AMS data				
Name	**L**	**F**	**P_j**	**T**
ME8	1.009	1.007	1.016	-0.170
ME9	1.010	1.007	1.018	-0.180
CR3	1.014	1.004	1.019	-0.503
CR15	1.016	1.008	1.025	-0.321
CR18	1.011	1.013	1.025	0.078
CR19	1.013	1.008	1.022	-0.220
CR48	1.006	1.021	1.029	0.587
CR54	1.007	1.012	1.020	0.248
CR59	1.009	1.016	1.026	0.306
CR66	1.013	1.011	1.025	-0.099
CR71	1.012	1.010	1.022	-0.117
CR82	1.003	1.016	1.021	0.656
CR83	1.014	1.012	1.026	-0.085
CR84	1.041	1.004	1.050	-0.818
CR86	1.013	1.009	1.023	-0.171
CR95	1.008	1.025	1.035	0.493
CR96	1.009	1.022	1.032	0.436
CR101	1.014	1.012	1.026	-0.069
CR114	1.016	1.007	1.023	-0.402

Table 10: AMS data for lower sheet samples

Lower Sheet AMS data								
Name	**UTM E**	**UTM N**	**Num.**	**K_m (SI)**	**K_m 1 s (SI)***	**K1**	**K2**	**K3**
	Zone 12N (NAD83)							
ME6	521180	4210224	6	0.027900	0.000767	1.015	1.000	0.984
ME7	521224	4210472	6	0.014300	0.000580	1.007	1.001	0.992
CR2	521586	4211623	6	0.006150	0.000310	1.021	1.002	0.977
CR7	522167	4211066	6	0.022700	0.000625	1.023	0.998	0.979
CR8	522049	4211158	6	0.037200	0.000600	1.012	0.997	0.991
CR9a	521942	4211221	6	0.018900	0.000217	1.018	0.998	0.984
CR10	521064	4210512	6	0.000403	0.000040	1.014	1.003	0.983
CR24	521937	4210348	6	0.018300	0.000761	1.021	1.000	0.979
CR49	521895	4211488	5	0.000152	0.000012	1.006	1.001	0.993
CR62	521743	4209868	6	0.023100	0.000370	1.010	1.000	0.990
CR63	521788	4209571	6	0.019800	0.000650	1.010	1.005	0.984
CR73	521870	4211677	6	0.000222	0.000006	1.010	1.000	0.991
CR76	521598	4211906	6	0.013800	0.000154	1.017	0.999	0.985
CR81	521245	4212011	6	0.020000	0.000374	1.017	0.999	0.984
CR87	522210	4211692	6	0.016200	0.000479	1.011	1.002	0.987
CR88	522480	4211948	6	0.006670	0.000351	1.008	1.001	0.991
CR103	521432	4210261	6	0.014700	0.000880	1.017	1.001	0.982
CR104	521325	4210067	6	0.007370	0.000502	1.011	1.003	0.986
CR105	521375	4209868	6	0.015100	0.000371	1.018	1.002	0.979
CR113	521175	4210423	6	0.008780	0.000087	1.015	1.002	0.983

AMS data for lower sheet samples, continued

Lower Sheet AMS data												
Name	**K1**				**K2**				**K3**			
	decl.	**incl.**	**α_{95} max**	**α_{95} min**	**decl.**	**incl.**	**α_{95} max**	**α_{95} min**	**decl.**	**incl.**	**α_{95} max**	**α_{95} min**
ME6	248.8	62.9	8.2	2.5	9.5	14.7	11.0	2.8	105.7	22.3	7.9	2.4
ME7	259.8	20.5	17.4	3.9	158.3	27.9	17.6	6.5	21.1	54.2	7.7	4.9
CR2	230.0	55.4	6.5	2.5	119.6	13.5	4.6	3.8	21.2	31.1	6.6	2.9
CR7	216.1	30.5	5.6	1.1	307.0	1.4	5.5	3.6	39.3	59.4	4.6	2.3
CR8	339.2	22.5	2.8	0.9	244.1	12.0	4.4	2.0	128.0	64.2	4.2	1.7
CR9A	154.4	43.9	9.7	0.7	331.2	46.0	9.8	2.0	62.9	1.6	2.6	0.6
CR10	314.4	51.1	7.6	4.1	161.3	35.7	6.4	3.9	61.5	13.4	5.9	3.8
CR24	322.9	29.7	3.8	1.6	186.5	51.8	4.6	1.6	66.0	21.8	5.8	0.7
CR49	341.7	36.7	19.1	3.0	229.0	27.5	20.1	11.8	112.1	41.0	13.6	2.0
CR62	271.8	8.5	3.1	1.7	181.4	2.5	4.8	2.6	75.4	81.2	4.6	1.9
CR63	296.8	14.5	33.7	6.2	143.9	73.8	32.4	4.4	28.6	7.1	17.8	1.8
CR73	228.9	61.1	6.3	1.3	326.1	4.0	6.1	1.5	58.2	28.6	2.5	0.9
CR76	144.7	65.8	2.7	1.7	35.1	8.5	2.8	2.1	301.6	22.5	2.7	1.4
CR81	48.2	3.6	9.0	4.4	154.8	77.6	10.0	0.9	317.5	11.9	6.1	3.7
CR87	48.0	74.2	7.7	1.6	243.5	15.2	8.2	2.2	152.4	4.0	3.7	1.7
CR88	58.9	19.9	12.3	2.4	303.7	49.6	12.3	6.2	162.8	33.5	6.5	1.5
CR103	108.5	69.4	4.9	1.4	226.5	10.0	4.1	1.9	319.7	17.8	3.0	1.8
CR104	16.2	20.5	5.4	2.5	245.4	60.2	5.3	3.6	114.3	20.6	4.1	3.3
CR105	59.4	5.3	7.1	3.3	183.4	80.5	6.8	0.7	328.7	7.8	4.4	1.6
CR113	304.9	69.4	3.3	2.3	196.4	6.8	4.3	1.6	104.0	19.4	3.8	1.6

AMS data for lower sheet samples, continued

Lower Sheet AMS data				
Name	**L**	**F**	**P_j**	**T**
ME6	1.015	1.016	1.032	0.039
ME7	1.006	1.009	1.015	0.242
CR2	1.019	1.025	1.045	0.122
CR7	1.026	1.019	1.046	-0.151
CR8	1.014	1.007	1.021	-0.363
CR9A	1.019	1.014	1.034	-0.156
CR10	1.012	1.020	1.033	0.273
CR24	1.021	1.022	1.043	0.038
CR49	1.006	1.007	1.013	0.139
CR62	1.011	1.010	1.021	-0.033
CR63	1.005	1.021	1.028	0.620
CR73	1.010	1.009	1.019	-0.016
CR76	1.018	1.014	1.033	-0.118
CR81	1.017	1.016	1.033	-0.045
CR87	1.009	1.015	1.025	0.259
CR88	1.007	1.010	1.016	0.178
CR103	1.016	1.020	1.036	0.100
CR104	1.008	1.017	1.026	0.364
CR105	1.016	1.024	1.040	0.195
CR113	1.012	1.020	1.032	0.231

Table 11: AMS data for not-CRL samples

Lower Sheet AMS data								
Name	**UTM E**	**UTM N**	**Num.**	**K_m (SI)**	**K_m 1 s (SI)***	**K1**	**K2**	**K3**
	Zone 12N (NAD83)							
CR34	521275	4212243	5	0.018100	0.000315	1.025	1.006	0.969
CR37	521403	4212584	5	0.000771	0.000097	1.003	1.001	0.996
CR38	521334	4212640	6	0.003630	0.000632	1.013	0.998	0.988
CR85	520340	4211497	6	0.000196	0.000014	1.009	0.999	0.991
CR100	520528	4212371	6	0.005650	0.001250	1.015	0.997	0.988

Lower Sheet AMS data												
Name	**K1**				**K2**				**K3**			
	decl.	**incl.**	**α_{95} max**	**α_{95} min**	**decl.**	**incl.**	**α_{95} max**	**α_{95} min**	**decl.**	**incl.**	**α_{95} max**	**α_{95} min**
CR34	321.2	4.4	3.0	1.5	144.0	85.6	2.5	1.6	51.3	0.2	2.4	1.6
CR37	318.3	0.4	14.1	10.1	227.6	60.0	16.1	13.2	48.5	30.0	16.2	9.1
CR38	202.1	1.7	23.1	3.4	111.9	8.2	28.4	16.8	304.0	81.6	24.9	2.5
CR85	49.4	66.9	11.8	2.2	252.5	21.4	4.9	2.5	159.3	8.3	12.4	2.8
CR100	213.6	45.8	13.5	5.4	307.2	3.5	24.0	9.7	40.5	44.0	22.5	5.9

Lower Sheet AMS data				
Name	**L**	**F**	**P_j**	**T**
CR34	1.019	1.039	1.060	0.327
CR37	1.003	1.005	1.008	0.315
CR38	1.015	1.010	1.025	-0.179
CR85	1.010	1.008	1.018	-0.137
CR100	1.018	1.009	1.027	-0.338